THESIS FOR THE DEGREE OF DOCTOR OF PHILOSOPHY

Sintering of water-atomized iron and low-alloyed steel powder

Surface chemical and thermoanalytical studies of oxide reduction and sintering

JOHAN WENDEL

Department of Industrial and Materials Science

CHALMERS UNIVERSITY OF TECHNOLOGY

Gothenburg, Sweden 2020

Sintering of water-atomized iron and low-alloyed steel powder
Surface chemical and thermoanalytical studies of oxide reduction and sintering

Johan Wendel

ISBN 978-91-7905-364-2

Doktorsavhandlingar vid Chalmers tekniska högskola
Ny serie nr 4831
ISSN 0346-718X

Department of Industrial and Materials Science
Chalmers University of Technology
SE-412 96 Gothenburg
Sweden
Telephone + 46 (0)31-772 1000
URL: www.chalmers.se

Printed by Chalmers Digitaltryck
Gothenburg, Sweden 2020

Sintering of water-atomized iron and low-alloyed steel powder

Surface chemical and thermoanalytical studies of oxide reduction and sintering

Johan Wendel
Department of Industrial and Materials Science
Chalmers University of Technology

Abstract

Iron and steel powder grades are extensively used in the powder metallurgy (PM) industry for manufacturing of ferrous structural components, with a major customer in the automotive industry. The powder grades are predominantly manufactured by water-atomization, yielding powder particles with highly irregular morphology and good compressibility, making the powder ideal for the conventional press-and-sinter manufacturing route.

The particles of the as-received powder are covered by a surface oxide layer, about 5-7 nm thick, as a result of the exposure to air or oxygen-containing atmospheres. The oxide layer is readily removed at low temperatures in the range 250-500 °C using hydrogen as a reducing agent, but the reduction process is strongly affected by the initial state of the powder and the alloy composition, as well as several processing parameters such as prior compaction of the powder and the composition of the processing gas. Since it contains a large fraction of the total oxygen content in the powder, removal of the oxide layer is a crucial step in the processing of these powder grades. Further raising the temperature enables the progressive reduction of various oxides as reflected by their thermodynamic stability, with oxides containing Cr, Mn and Si requiring significantly higher reduction temperatures than iron-based oxides. The progress of oxide reduction was studied using thermogravimetric and kinetic analysis and complemented with surface analysis methods.

Parallel to the chemical processes, shrinkage occurs as the powder particles are sintered. This increases the density of compacted powder as particles are bonded to each other and porosity decreases. The dimensional changes during sintering, as observed by dilatometry, are shown to be a function of compaction pressure, the direction relative to the compaction direction as well as multiple processing parameters such as the processing atmosphere, heating rate and sintering temperature where a significant phase-dependence exists. A large fraction of the total sintering shrinkage is attained already at low temperatures in the ferrite phase of the iron-based matrix.

The interaction between the chemical and physical processes are shown to be important for sintering as oxide reduction and oxygen removal are strongly dependent on the initial density of the compacted powder. Overall, oxide reduction is seen as a major goal in modern PM steelmaking in order to facilitate the development of strong, defect-free sinter necks. At the same time, sintering shrinkage and anisotropy must be considered as well to ensure dimensional tolerances. These two phenomena occur simultaneously, with large magnitudes already at temperatures significantly lower than standard sintering temperatures, indicating that the heating stage of the sintering process requires careful control in order to successfully sinter water-atomized iron and steel powder grades.

Keywords: water-atomized iron powder, water-atomized steel powder, sintering, thermogravimetric analysis, surface chemistry, surface analysis, dilatometry, oxide reduction, reduction kinetics

Preface

This work was carried out at the Department of Industrial and Materials Science, Chalmers University of Technology, Gothenburg, Sweden under the supervision of Professor Lars Nyborg and Professor Eduard Hryha. This doctoral thesis covers the topic of ferrous powder metallurgy, with special emphasis on the oxide reduction, sintering shrinkage and surface chemical changes that occur during the sintering of water-atomized iron and steel powder grades.

List of appended papers

I. **Surface analysis of fine water-atomized iron powder and sintered material**
J. Wendel, R. Shvab, Y. Cao, E. Hryha, L. Nyborg
Surface and Interface Analysis, 2018

II. **Oxide reduction and oxygen removal in water-atomized iron powder: a kinetic study**
J. Wendel, S. K. Manchili, E. Hryha, L. Nyborg
Journal of Thermal Analysis and Calorimetry, 2020

III. **Sintering behaviour of compacted water-atomized iron powder – effect of initial green state and processing conditions**
J. Wendel, S. K. Manchili, E. Hryha, L. Nyborg
Submitted for publication

IV. **Evolution of surface chemistry during sintering of water-atomized iron and low-alloyed steel powder**
J. Wendel, S. K. Manchili, Y. Cao, E. Hryha, L. Nyborg
Surface and Interface Analysis, 2020

V. **Reduction of surface oxide layers on water-atomized iron and low-alloyed steel powder by hydrogen: effect of alloying elements and initial powder state**
J. Wendel, S. K. Manchili, E. Hryha, L. Nyborg
Thermochimica Acta, 2020

VI. **Sintering behaviour of water-atomized iron and low-alloyed steel powder: anisotropy in dimensional and chemical changes during sintering**
J. Wendel, S. K. Manchili, E. Hryha, L. Nyborg
Manuscript

VII. **Effect of heating rate and process atmosphere on the thermodynamics and kinetics of the sintering of pre-alloyed water-atomized powder metallurgy steels**
E. Hryha, J. Wendel
Journal of the American Ceramic Society, 2018

Contribution to the appended papers

I. The author planned and performed parts of the experimental work and most of the analysis of the results. The author wrote the paper in cooperation with the co-authors.

II. The author planned and performed the experimental work and analysed the results. The paper was written in collaboration with the co-authors.

III. The author planned and performed the majority of the experimental work and analysed the results. The paper was written in collaboration with the co-authors. EBSD measurements were performed by Dr. Alexander Leicht.

IV. The author planned and performed the experimental work and analysed the results. Dr. Eric Tam assisted in the vacuum annealing experiments. The paper was written in collaboration with the co-authors.

V. The author planned and performed the experimental work and analysed the results. The paper was written in collaboration with the co-authors.

VI. The author planned and performed most of the experimental work and analysed the results. The XRD measurements were performed by S. K. Manchili. The paper was written in collaboration with the co-authors.

VII. The author took part in the planning of the experimental work and analysed parts of the results. The paper was written in collaboration with the co-author.

Papers not appended in this thesis

a. **Sintering aspects of carbonyl iron powder used in metal injection moulding**
J. Wendel, R. Shvab, E. Hryha, L. Nyborg, D. Riabov, S. Berg
Proceedings of World PM 2016

b. **Oxide reduction and oxygen removal in water-atomized iron powder and compacts**
J. Wendel, S. K. Manchili, E. Hryha, L. Nyborg
Proceedings of World PM 2018
An extended version of this paper was published in Journal of Thermal Analysis and Calorimetry (see Paper II)

c. **Analysis of iron oxide reduction kinetics in the nanometric scale using hydrogen**
S. K. Manchili, J. Wendel, E. Hryha, L. Nyborg
Nanomaterials, 2020

d. **Effect of nanopower addition on the sintering of water-atomized iron powder**
S. K. Manchili, J. Wendel, A. Zehri, J. Liu, E. Hryha, L. Nyborg
Metallurgical and Materials Transactions A, 2020

Abbreviations, mathematical expressions and materials

AES	Auger electron spectroscopy
DIL	Dilatometry
DSC	Differential scanning calorimetry
DTG	Differential thermogravimetry
EBSD	Electron back-scatter diffraction
HAGB	High-angle grain boundaries
KAM	Kernel average misorientation
LAGB	Low-angle grain boundaries
MIM	Metal injection moulding
PM	Powder metallurgy
SEM	Scanning electron microscopy
TGA	Thermogravimetric analysis
XPS	X-ray photoelectron spectroscopy

α (BCC)	Ferrite – the low-temperature phase of iron
γ (FCC)	Austenite – the high-temperature (up to ~1395 °C) phase of iron
p_{O_2}	Partial pressure of oxygen
p_{H_2}	Partial pressure of hydrogen
p_{H_2O}	Partial pressure of water vapour
ΔG^0	Change in standard Gibbs free energy
R	Gas constant, 8.314 J/mol·K
T	Absolute temperature
α	Conversion
A	Pre-exponential factor
Φ	Heating rate
E_a	Activation energy
E_α	Conversion-dependent activation energy
m_i	Initial sample mass
$m(t)$	Instantaneous sample mass
m_f	Final sample mass

ASC100.29 – Water-atomized powder, produced by Höganäs AB
CrA – Fe-1.8Cr, Cr pre-alloyed water-atomized steel powder, Höganäs AB
CrM – Fe-3.0Cr-0.5Mo, Cr pre-alloyed water-atomized steel powder, Höganäs AB

TABLE OF CONTENTS

Chapter 1

INTRODUCTION

1.1 BACKGROUND

Powder metallurgy (PM) generally refers to the scientific and technological aspects of production and further processing of metal powder, as well as the various manufacturing routes that are subsequently used to produce components from that powder. Several methods can be classified as belonging to the PM family; press and sinter, powder forging (PF), metal injection moulding (MIM) etc. Amongst these methods, the conventional press and sinter process route accounts for the overwhelming majority of all manufactured components from iron-based powder [1], and is the process being studied in this thesis. The benefits of the press and sinter manufacturing route are that, compared to more traditional methods such as casting and machining, the energy consumption and material waste can typically be kept to relatively low levels [2–4]. The key lies in the sintering process where powder is brought to elevated temperatures, yet below the melting point, at which the powder particles start to bond to each other by diffusion mechanisms. This results in a densification of the material along with an increase of the mechanical properties. Figure 1.1 shows a comparison of the raw material yield and energy consumption between sintering and other manufacturing methods, highlighting the efficiency of sintering-based methods. Today, the PM industry is significant and growing, although it is still small in relation to traditional metal working and is likely to remain a highly specialized industry used only for dedicated applications. Figure 1.2 shows that the press and sinter route is typically limited to production of components of low to medium complexity and annual production quantities of 10^4 components or more. Another restriction of press and sinter PM is that the mechanical properties that can be attained are limited by the inherent porosity

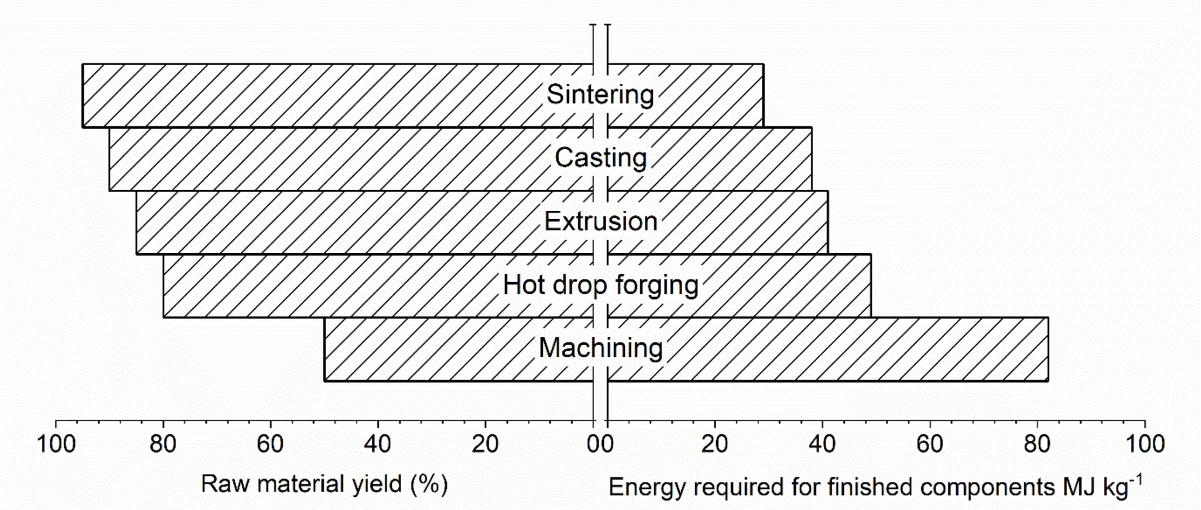

Figure 1.1: Raw material yield and energy consumption compared for some manufacturing methods. Adapted from: Schatt and Wieters (1997).

of the components, making them unfit for certain applications. However, several routes such as warm compaction, repressing, etc., can be utilized to approach the theoretical density [5].

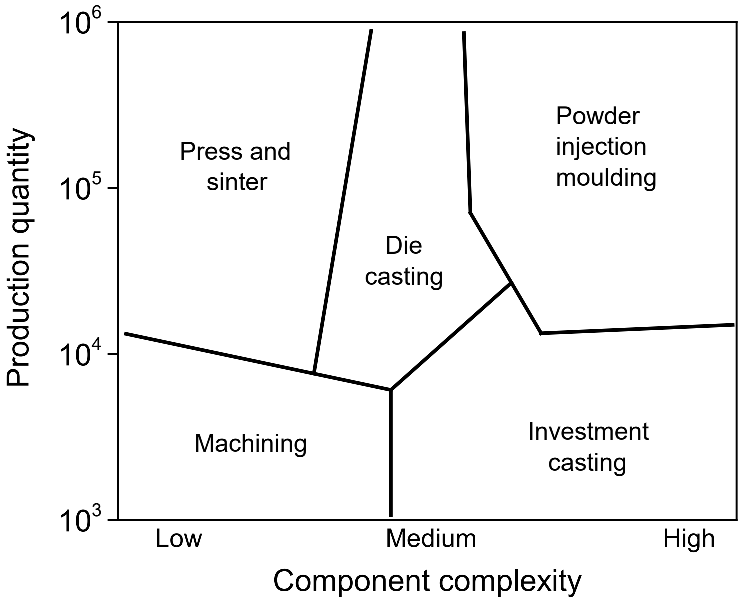

Figure 1.2: Schematic plot of the annual production quantity versus component complexity for some manufacturing methods. Adapted from: German (1996).

PM is today a well-established manufacturing route for ferrous components [2]. Still, various research efforts are ongoing, often focused on increasing the density of the components after sintering and thereby widen the range of possible applications of PM components. Notable examples are liquid phase sintering with master alloys [6,7], and utilization of hot isostatic pressing methods for reaching fully dense PM steels [8]. Other efforts aim to further improve the dimensional stability of sintered steels and strengthen its status as a method for precision manufacturing [9,10].

Other research areas are related to the development of advanced PM steels, with alloying elements that are relatively new in the PM industry such as Cr and Mn [11]. Because these elements are sensitive to oxygen, they typically require more careful control over the sintering conditions to not risk excessive oxidation which may deteriorate the mechanical properties [11,12]. Considerable research efforts have been put into studying these metal oxide systems that are important in PM. The vast majority of previous studies have been concerned with the stable oxide particulates that are randomly distributed on the surfaces of the powder particles. Some aspects that have been investigated are their formation and thermodynamic stability [12], their influence on mechanical properties [13], as well as their composition, size and distribution [14]. Less is known about the surface oxide layer, which covers the major fraction of the surface, and its possible implications on the sintering process. The reason for this is because the low-stability iron oxides are seen as non-critical, both in terms of the sintering of particles and the requirements on the sintering atmosphere [12,15–17].

1.2 AIMS AND SCOPE

While press and sinter PM can be thought of as a mature manufacturing technology in many respects, several questions and details remain to be investigated. The aim of this thesis is to further expand the understanding of some critical aspects involved in processing of water-atomized iron and steel powder used for press and sinter powder metallurgy. More specifically, the oxide reduction events and sintering shrinkage that occur during the heating stage of sintering have been investigated using a combination of surface- and thermoanalytical experimental methods.

Several materials were chosen for the investigation. Nominally pure water-atomized iron powder (ASC100.29, Höganäs AB) and sieved fractions were initially analysed as a model material system to provide the foundation of the study, along with Fe_2O_3 as an oxide reference. Two common water-atomized steel grades pre-alloyed with chromium (CrA and CrM, Höganäs AB) were then included to represent materials of greater industrial importance.

The research questions (**RQs)** can be related to a few areas of study, most conveniently separated as those concerned with oxide reduction and those related to the dimensional changes of sintering.

1.2.1 Oxide reduction and oxygen removal in water-atomized ferrous powder

All ferrous metal powder particles are covered by a thin surface oxide layer as a result of their exposure to air or oxygen-containing atmospheres. While the oxide is readily reduced at low temperatures in the presence of hydrogen, the reduction process is affected by several factors related to material characteristics and experimental parameters. At elevated temperatures, during the heating stage of sintering, progressive oxide reduction of internal and thermodynamically stable oxides is crucial to ensure that the oxygen levels are kept low in the component. In an industrially analogous setting using compacted powder, the oxide reduction and oxygen removal is significantly affected, since compaction restricts the pathways in and out of the powder compact. Research questions that are related to oxide reduction are:

- ***RQ 1:*** *What are the characteristics of the surface oxide layer, and how is it affected by powder alloy composition, initial state and compaction? [Papers I, II, IV, V]*

- ***RQ 2:*** *What are the origins of the different stages of mass loss in powder, and how are they affected by alloy composition and compaction? [Papers I, II, IV, V, VI, VII]*

1.2.2 Sintering behaviour of water-atomized ferrous powder

Whereas thermogravimetric analysis is ideal for studying oxide reduction processes, it cannot capture the sintering behaviour of powder in which mass transport mechanisms act to create sinter necks between particles. While many aspects of sintering are well understood, the interaction between sintering atmosphere and die-compacted powder calls for further investigation. In extension, the strong anisotropic character expected in sintered compacts derived from compaction raises further questions about the sintering of these materials. Research questions reflecting this part of the study are:

- ***RQ 3:*** *How do the initial states of the as-received and compacted powder influence sintering and shrinkage anisotropy, and what are the implications for densification? [Papers III, VI]*

It should be noted that both reduction of oxides and the mass transport mechanisms, responsible for development of sinter necks, are thermally stimulated processes, and thus occur simultaneously to some extent. This raises an additional question:

- ***RQ 4:*** *What are the mechanisms of interaction between oxide reduction, oxygen removal, and dimensional changes that occur during the heating stage of sintering of water-atomized iron and steel powder? [Papers II, V, VI, VII]*

Chapter 2

THE POWDER METALLURGY PROCESS

The aim of this chapter is to introduce the processing steps that make up the conventional press and sinter manufacturing route in ferrous PM. The processing steps can be summarized as; (i) powder production through atomization (ii) mixing with additives, (iii) shaping through compaction, (iv) delubrication, (v) sintering and (vi) post processing operations. Detailed schematics of the different processing steps can be found elsewhere, see e.g. [2].

2.1 POWDER PRODUCTION

The most common method to produce powder for ferrous PM is by atomization. In atomization, a stream of molten metal is disintegrated by high-pressure water or inert gas (water- or gas-atomization, respectively) which creates droplets of molten metal that rapidly solidify into particles. The atomization process parameters determine many properties of the powder, e.g. the mean size of the particles, the particle size distribution and the particle morphology. In addition, the chemical properties of the powder are affected as the atomization introduces oxygen into the material. The increased oxygen levels of water-atomized powder are commonly reduced by introducing an annealing step before the subsequent processing of the powder in the PM process. After atomization, the metal particles are sieved to create a well-defined powder grade with a nominal composition, morphology and particle size distribution according to standardized specifications.

It should be noted that the atomization and annealing steps are decisive in determining some of the key properties of the powder, but the details are typically proprietary information that cannot be disclosed. The powder grades analysed in this thesis are thus mostly in its "as-received", commercial condition.

Water-atomized iron powder is the workhorse of the conventional press and sinter route in the PM industry, mainly due to the low cost of the powder which allows for full utilization of the benefits of PM. The irregular particle morphology of the powder, caused by the balance between the spheroidization of the molten particles and the rapid cooling when using water as the atomization medium, typically gives high green strength, i.e. after shaping operations, which allows for easier handling. This is a consequence of the metal particles being mechanically interlocked with each other by protrusions.

2.1.1 Alloying

While plain water-atomized iron powder can be used in some applications, it is more common to alloy the material with elements that enable an increase of mechanical properties in the final component. This can be done in several ways; pre-alloying, diffusion-bonding, admixing etc. In this thesis, the focus will be on grades that are either plain water-atomized iron powder, or grades that are pre-alloyed with chromium. Pre-alloying introduces the alloying elements prior to atomization which means that they are in solid solution with the base metal. This limits the composition of the steels due to solid solution strengthening but has been shown to allow for successful incorporation of oxygen-sensitive alloying elements such as Cr and Mn [18].

2.2 POWDER MIXING

In the case of the conventional press and sinter route, the chosen powder is then mixed with a lubricant in order to facilitate the subsequent shaping operation. The lubricant, which is typically an organic compound, reduces the friction both between the powder and the die, and between the metal particles. This is important as it ensures a homogenous particle distribution and increases the level of powder packing. The amount of lubricant is typically in the range of 0.3-0.5 wt. %. Graphite is also commonly admixed as a source of carbon to increase the mechanical properties of the finished components. Since carbon has a large solid solution strengthening effect on iron, it must be admixed to the powder rather than alloyed prior to shaping.

2.3 COMPACTION

The shaping of metal powder involves a compaction step in which the powder is pressed into a die cavity of a desired shape. The compaction initially leads to rearrangement of powder particles with an increase in pressure causing deformation to initiate at interparticle contact points. Further raising the pressure increases the number and size of the contact points which eventually leads to a high-density configuration of the powder [19]. The effect is more pronounced for ductile materials such as iron. At high compaction pressures, there is a transition from particle rearrangement to particle deformation which then becomes the main source of density increase [19–21]. The deformation is partly elastic and partly plastic. Whereas the elastic deformation is relieved after the green compact is ejected from the die in a spring-back effect, the plastic deformation remains in the compacts [2]. Parallel to rearrangement and deformation of the metal particles, the number and size of pores is reduced which aids in the subsequent sintering process in which pores are eliminated to densify the material [19].

Uniaxial die compaction inherently results in density gradients in pressed compacts. The density gradients are most prevalent along the surface regions of the compacts in the pressing direction. For uniaxial pressing there is a high relative density around the middle region, while this becomes a region of low relative density for compaction in two directions [2]. The density gradients in green compacts are a major cause of sintering anisotropy which can cause severe limitations in keeping component tolerances [22,23]. Enclosed or fractured oxide layers at interparticle contact regions may also lead to oxygen trapping as the layers become enclosed within interparticle regions [24].

Alternative compaction methods such as cold isostatic pressing (CIP) can be used to circumvent the issue of density gradients by providing a homogeneous density distribution in the compacts, which leads to more isotropic sintering behaviour. Higher green densities can also be achieved, since no lubricants are used. However, CIP has other issues related to it like low geometrical flexibility and poor tolerances [2].

2.4 DELUBRICATION

The purpose of delubrication is the removal of lubricants used in the compaction process. The additives are typically based on organic compounds which are removed by thermal decomposition. Removal of lubricants can be a complex process, and failure is likely to be associated with problems that are often only revealed during the subsequent sintering, at which point there is low likelihood of addressing the issue. The decomposition process typically leads to formation of products such as hydrocarbons, CO, CO_2 and H_2O, which risk to deteriorate the processing atmosphere [25]. While delubrication is relatively easy on a lab-scale, knowledge of industrial scale delubrication processes is necessary to ensure robust production. On-line monitoring of delubrication has been promising [26], and further modification of the atmosphere to create a simulated dirty environment could be useful in predicting the delubrication and sintering behaviour [25].

2.5 SINTERING

The concept of sintering has been known to humanity for several thousands of years, with its application to metals dating back to 3000 BCE [27]. At the time, sintering was born out of necessity since casting temperatures were unattainable in many cases. When casting could eventually be achieved, sintering lost its importance and was largely unused. Starting from the 18th century, records exist of trial and error sintering for a range of materials, including porcelain, iron and platinum, with further introduction of refractory elements like tungsten for use in the early electronics industry of the 19th century. The 20th century brought development of models and theory, initiating the science of sintering [2,27]. Today, sintering is widely employed for metals when a specialized role can be filled, for example when the net-shaping capabilities of PM are beneficial, or a specialized microstructure is required [2].

Sintering is done at elevated temperatures, which for ferrous material is typically at 1120-1250 °C, and is usually the most energy intensive step of the PM process [3]. Apart from the sintering temperature and sintering time, the sintering atmosphere is another crucial parameter that needs to be considered. How the atmosphere interacts with the powder being sintered is determined by the thermodynamic stability of the elements and their compounds under a given set of conditions.

At elevated temperatures, diffusion mechanisms become more active, which allows for increased movement of atoms. The minimization of the total surface area of the compacts is a key driving force of sintering in which metal particles are bridged and bonded together with so called sinter necks [19]. This driving force, however, is large only for small micrometre-sized particles, e.g. powder used for MIM. For coarser powder grades, such as those used in the conventional press and sinter route, the driving force for minimization of surface area is less prominent and acts on a smaller, local level, which consequently leads to less sintering. Despite this, sintering can be enhanced by increasing the number of contact points between particles, and even further by increasing the size of those contacts by compaction. By ensuring a high initial green density in this way, sintering can be realized by means of diffusion to yield good interparticle bonding. Concomitantly, provided that the sintering activity is high enough, atoms will move to sustain neck growth and ultimately eliminate pores from the compact. The overall result is an increase in density and improved mechanical properties. Even so, improved properties will be gained even if densification is at a minimum, owing to surface diffusion effects that result in neck growth [28]. More specific details about sintering of water-atomized iron and steel powder grades can be found in Chapter 3.

2.6 POST-SINTERING PROCESSING

Post-sintering processing operations are often necessary to finish a component. This can be e.g. sizing and re-pressing of components to keep tolerances and increase density, machining to remove unwanted features or add threaded holes, or heat treatments to carburize or harden the component. Sinter-hardening, which combines sintering and a hardening operation into a single step, can also be used. Since the focus of this thesis has been on the properties of the as-received powder and how it behaves during compaction and the heating stages of sintering, no further details regarding these post processing operations are explained here.

Chapter 3

FERROUS POWDER METALLURGY

The aim of this chapter is to provide a description of ferrous metallurgy processing based on the literature review which served as the framework for the thesis as well as to provide further details regarding the research questions posed in Chapter 1.

3.1 BACKGROUND

Iron is arguably one of the most important engineering materials of the present day, particularly in combination with carbon as a basis for steel. The global annual demand for steel is enormous and increasing. The figure (as of 2009) sits at around 1.4 Gt per year, which is about 200 kg per person per year, but is projected to increase to up to 2.8 Gt by 2050 [29]. This situation is reflected in PM, where ferrous powder metallurgy, i.e. iron-based material systems such as pure iron and various steels comprise the major fraction of the world market of PM components, although at a much smaller scale of about 1 Mt per year [1]. Typical applications of PM steels are within the automotive industry, for engineering equipment, and more generally for the metal-processing industry [2,30]. The automotive industry is a key customer, with PM presenting a competitive alternative manufacturing method for several applications such as crank shafts, connecting rods, transmission gears etc. [1,2]. However, it should be noted that with the trend in increasing electrification, conventional PM likely needs to adapt in order to stay competitive for the automotive industry. This adaptation can probably to some extent be achieved by the inherent flexibility of PM with regards to the wide range of processes, materials, shapes and products [31].

3.1.1 Materials

Most ferrous components utilize powder produced via water- or gas-atomization, with water-atomized powder being much more common for iron and low-alloyed steels due to its relatively low production costs [1,3], and irregular particle morphology which aids in compressibility and handling during the subsequent processing [32,33]. The traditional alloying elements in ferrous press and sinter PM have been Ni, Cu and Mo. However, a combination of several factors such as an increase in price and price volatility as well as health concerns for the usage of Ni, and recyclability issues with Cu, gives an incentive towards the use of more sustainable elements. Instead, a new set of advanced PM steels was developed based on alloying elements that are standard in wrought steelmaking, such as Cr, Mn and Si [11,34]. The oxides of Ni, Cu and Mo are relatively unstable compared to the oxides of Fe, which in practise meant that oxide reduction and sintering of these components could be readily achieved by only considering the requirements for iron. However, the oxides of Cr, Mn and Si are much more thermodynamically stable than iron oxides, thus requiring significantly improved atmospheric conditions for successful oxide reduction, and in extension, sintering [34]. This is reflected in the alloying method where elements that form relatively unstable oxides can be added as elemental powder prior to compaction, whereas stable-oxide forming elements like chromium need to be protected from oxidation. This is commonly achieved by pre-alloying with Cr before atomization, thus incorporating it directly in the iron-matrix as a solid solution which lowers the activity of Cr and prevents it from excessive oxidation [18,35].

Höganäs AB, Sweden, introduced several chromium pre-alloyed grades in recent decades, for example Astaloy™ CrM (Fe-3.0Cr-0.5Mo) [18] and CrA (Fe-1.8Cr). These grades are commonly used in the press and sinter PM route, and show excellent compressibility despite the pre-alloying. The chromium also provides hardenability for useful mechanical properties. Over the years, significant research effort has been put into understanding the properties of these and related powder grades and how they change during the sintering process, see e.g. [17,34,36–39] regarding the chemical properties as a function of temperature and processing atmosphere, or [9,10,22,40] concerning the dimensional changes during sintering and how to control them.

3.2 OXIDES IN FERROUS POWDER METALLURGY

Water-atomization results in extensive oxidation of the powder due to the interaction between the water jets and the molten metal. The oxygen levels are therefore lowered in a subsequent annealing step prior to further processing. However, even after annealing, the powder in its 'as-received' state typically contains a minor amount of oxygen (~0.1-0.15 wt. %) because of its inherently large specific surface area which results in surface oxide formation during contact with air or oxygen-containing atmospheres.

To successfully sinter PM steels, some degree of atmosphere control is required, and the requirements are dictated by the alloying elements as indicated earlier. The sintering atmosphere typically has several purposes; to protect from oxidation and reduce residual oxides to improve metallic contacts, as well as to protect carbon-containing material from decarburization [32]. Several different classes of sintering atmospheres can be used depending on the needs [32], but the oxide reducing components are typically hydrogen, which facilitates reduction at low temperatures, and carbon, which participates in carbothermal reduction mechanisms at higher temperatures [12,32,41].

The oxides in PM steels come in two major classes; (i) the surface oxide layer which typically covers a large fraction (up to 95 % [12]) of the surface area of the powder particles, (ii) particulate oxides which can be classified into internal and discrete oxides randomly distributed on the surface of the metal particles where they are separated by the surface oxide layer. Because of the large surface-to-volume ratio of powder, and the low solubility of oxygen in ferrite and austenite [42], the surface oxide layer contains a large fraction of the total oxygen content in the powder (up to 30-50 % [12]), with the fraction increasing with decreasing particle size [43]. The remaining oxygen is present in internal oxides as well as the stable particulate oxides on the surface.

Common methods to observe and analyse these oxides are via thermoanalytical methods such as thermogravimetric analysis (TGA) from which the reduction of oxides can be inferred by the mass loss signal, see e.g. [6,17,41,44,45]. Surface analytical techniques such as X-ray photoelectron spectroscopy (XPS) and Auger electron spectroscopy (AES) are also commonly used, providing chemical information and some degree of spatial resolution along with depth-profiling capabilities, see e.g. [12,14,43,46].

3.2.1 Surface oxide layer

The surface oxide layers covering commercial water-atomized iron and steel powder grades are commonly reported to be based on predominantly Fe_2O_3, i.e. hematite, for nominally pure iron powder (ASC100.29) and chromium pre-alloyed grades (CrA and CrM) [12,14,43]. However, the oxide layer composition is believed to also reflect the alloy composition to some extent if the oxides are formed at low temperature where the atomic mobility is low [47]. Consequently, some differences are expected between the oxide layers formed on ASC100.29, CrA and CrM although the major constituent of the oxide layers will be iron oxide. The thickness of the surface oxide layer is commonly reported to be 5-8 nm for both water-atomized iron and chromium pre-alloyed steel grades [14,38,43,46].

Since the iron oxides, FeO, Fe_3O_4 and Fe_2O_3, are less stable than oxides based on Cr, Mn and Si, the presence of the surface oxide layer is typically not considered to be an issue during sintering as indicated previously. However, since the oxide layer contains a large fraction of the total oxygen in the powder, it can play an important role during sintering if not removed properly. This is the case for oxygen transfer effects that can occur if the microclimate that exists in the vicinity of the metal particle surfaces becomes simultaneously reducing and oxidizing to iron and stable-oxide forming elements, respectively, allowing the transfer of oxygen from one element to another without leaving the compact [6,45]. Elsewhere, not directly related to the PM industry, reduction of iron oxides has been extensively investigated due to its importance in iron- and steelmaking [48–50], although the studies are typically conducted on industrial-type ores or pellets. A range of materials of varying purity are studied, with the residues being known to influence the oxide reduction kinetics by way of catalysis, obstruction, or causing structural changes in the iron oxides that also affect the reducibility [50–55]. In terms of processing, studies have shown that mechanical deformation of hematite influences the structure and reactivity of the oxide [56,57]. While the results are not directly comparable to the present analyses where the iron oxide instead exists as a thin layer covering metal particles, the milling can possibly be viewed as a high-intensity analogy to the compaction step of the conventional press and sinter route.

In this thesis, the reduction of the surface oxide layer is expected to deviate slightly from reduction of a pure iron oxide due to the small concentrations of alloying or trace elements, the nanometer dimensions of the oxide layer, and compaction effects. Additional influences associated with the initial, as-received, state of the powder can also be observed as will be shown later. Overall, it can be said that a combination of several parameters such as oxide composition and structure, compaction and processing atmosphere influences the reduction of the surface oxide layer.

Effect on sintering

Regarding sintering, the significance of the oxide layer covering the powder particle surfaces is not unambiguously decided [15,58]. The role of the oxide layer is a function of its thermodynamic stability and ability to act as a diffusion barrier, and if the layer can be dissociated or reduced relatively easily, then there is no inhibition to diffusion and clean metal-metal contacts can be formed. Still, it has also been reported that the oxide layer on iron may not be detrimental at all so that sintering can proceed relatively unhindered, despite its presence. However, some of the investigations have been conducted mainly at high temperatures where diffusion rates are high [15,58]. Even if the oxide layer should not pose a large barrier to diffusion, other studies have indicated that clean metal-metal contacts can likely improve the sintering rates [16], thus indicating that at least partial removal of the oxide layer is beneficial for sinter neck development.

In the investigations conducted in this thesis, in line with the industrial standard, hydrogen is used as a reducing agent to enable low temperature surface oxide layer reduction. For many experiments, the sintering temperatures are also lower than the previously mentioned studies and industrial sintering cycles, which possibly influences the importance of the surface oxide layer in terms of sintering. Since the metal-metal contacts have been shown to influence the sintering rates [16], the kinetics of sintering as measured by dilatometry [59,60] are also likely affected to some extent. Regardless whether the oxide layer inhibits sintering or not, the available oxygen bound as oxides will remain in the material after sintering if they are not reduced. This situation is not desirable as the developing sinter necks will be weakened by the oxide defects which may in turn affect the mechanical properties after sintering. Distinctions must therefore be made between sintering conditions where the oxide layer is present and where it is removed at low temperatures in the presence of hydrogen, with the processing atmosphere becoming an important variable not only directly for oxide reduction but also for sintering shrinkage.

3.2.2 Particulate oxides

Since the introduction of chromium pre-alloyed grades, research efforts have been directed to understand these new alloying systems and related powder grades. Of special interest has been the presence and transformation of stable oxides during the sintering process, i.e. their distribution, growth and interference with sinter neck development. An extensive set of literature exists in this area; see e.g. [12–14,37,38,46,61,62].

Unlike the continuous iron-based surface oxide layer that encapsulates the powder particles, these stable oxides exist as discrete islands randomly distributed on the surface of the powder particles and originate from the powder atomization. Because of their stability, these oxides remain longer during the sintering process and may influence mechanical properties if e.g. oxide residues become trapped in developing sinter necks. Such situations can arise for example when using only low vacuum levels or solely inert or non-reacting atmospheres that cannot on their own reduce oxides. The effect manifests itself mostly as an effect on the impact strength and fatigue life of the sintered component [13]. In addition to particulate oxides located on the surfaces of the powder particles, internal oxides are also present to some extent [63,64]. The removal of these oxides is possible at relatively low temperatures in certain cases, and is expected to reflect the chemistry of the oxides [64].

Overall, oxide reduction is a major goal in modern PM steelmaking utilizing sensitive elements like Cr which require additional considerations regarding the processing atmosphere. Failure to address the issues may lead to interference with sintering which in extension deteriorates the mechanical properties of the components. It should also be noted that a complicating factor in oxide reduction is the influence of compaction, as a decrease in porosity limits the supply of processing gas to and from the inner parts of the compacts which thus impairs reduction [65].

3.3 SINTERING OF WATER-ATOMIZED IRON POWDER

Solid-state sintering is the main sintering method for water-atomized ferrous powder grades and is essentially the movement of atoms below the melting temperature of the material. To understand and predict the sintering behaviour has been a huge incentive for related industries, with both energy and material savings being important, as well as limiting the dimensional spread in sintered components [9,10].

As indicated earlier, sintering is based on the activation of several mass-transfer mechanisms with the minimization of surface energy being a key driving force [19]. The mechanisms by which sintering is possible are varied and act differently, but can be summarized as surface, grain boundary and volume diffusion, with additional material movement occurring to a lesser extent through plastic flow, evaporation/condensation as well as by pipe diffusion. A schematic overview of the actions of different sintering mechanisms can be seen in Figure 3.1, adapted from German (2014) [66].

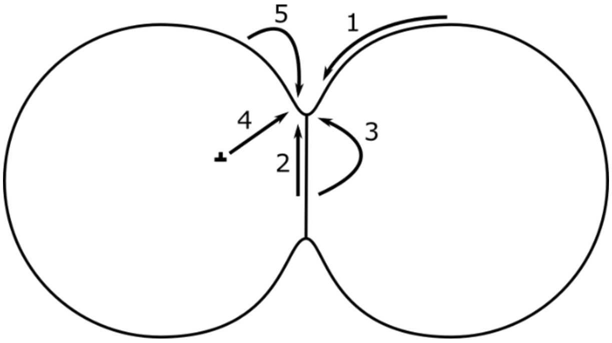

Figure 3.1: Schematic figure of different sintering mechanisms; 1) surface diffusion, 2) grain boundary diffusion, 3) volume diffusion, 4) plastic flow, 5) vapour transport. Adapted from: German (2014).

Surface diffusion moves atoms across surfaces and does not cause densification as the interparticle distance is not reduced [67], but can still aid in sinter neck formation and thereby increase the strength of compacts [28]. However, many mechanical and other properties rely to a large extent on density [2,5]. This requires densifying diffusion mechanisms where atoms are transferred from inside the powder to a developing sinter neck, with grain boundary and volume diffusion being the most important mechanisms. Diffusion coefficients typically follow the rule $D_S > D_{GB} > D_V$ for surface, grain boundary and volume diffusion, respectively. However, they typically have different activation energies and thus become most active at different temperatures [19,68]. The magnitude of sintering and the ratio of the contributions from different mechanisms can further change with powder size [67] as well as the crystal structure [28,69]. Additional problems with a generalized sintering theory is that even for simple model systems, the complexity increases rapidly in an applied industrial setting, with sintering influenced by a number of factors such as particle size distribution, morphology, added lubricants or additives, the subsequent compaction [19], as well as by any interaction with the sintering atmosphere.

3.3.1 Extent of sintering

On a macroscopic scale, the collective movement of atoms cause measurable dimensional changes that are commonly obtained by dilatometry, providing a continuous monitoring of the sintering progress during arbitrary temperature programs. This method is readily applied in PM steel research, see e.g. [22,40,44], and is the method that was opted for in this thesis.

Water-atomized grades are generally expected to have relatively poor sintering activity compared to e.g. the fine carbonyl iron powder used in metal injection moulding because of the much larger size of the particles [28]. However, in conventional ferrous PM, the main goal of sintering is not to acquire a large density increase but to improve mechanical properties and keep tolerances. High initial green densities through compaction is therefore often preferred [2]. The sintering behaviour of these powder grades has been investigated previously with a special reference to the sintering anisotropy responsible for density and property gradients [22,40,59,60,70]. Power-law sintering behaviours are sometimes used to describe the mass transport mechanisms involved in isothermal shrinkage, although studies also show that a modification of these models is typically required to account for the increase in structural defects that are common for die-compacted ferrous powder grades [59,60]. Compaction activates the material by the creation of a defective zone in which an increased density of dislocations and low-angle grain boundaries reflect the deformation state in the compact [60,70–73]. This activation of the material, in terms of an altered interparticle contact region, is believed to enhance diffusion [60,73,74], although it is unclear what role recovery and recrystallization play as dislocations will be annealed out at elevated temperatures.

As described earlier, the conventional PM manufacturing route for water-atomized iron and steel powder grades predominantly relies on solid-state sintering. However, other methods of sintering are possible but are only applied when there is strong economic incentive to do so. One example is liquid phase sintering where one component of the pressed compact is brought to above its melting temperature after which the liquid can infiltrate porosity and bind the phases together, see e.g. [6,7] regarding the use of master alloys in PM steels.

Chapter 4

THEORETICAL CONSIDERATIONS

This chapter aims to provide the foundation for the thermodynamic and kinetic analyses that is needed for the subsequent interpretation of the results. An overview of diffusion and sintering mechanisms relevant for the present material system is also given.

4.1 THERMODYNAMICS OF OXIDATION AND REDUCTION

The relation between temperature and oxygen partial pressure conditions that are required to uphold equilibrium between an oxide and its reactants can be written as

$$\mathrm{p}_{\mathrm{O}_2} = \exp\left(-\frac{\Delta \mathrm{G}^0}{\mathrm{RT}}\right) \qquad (4.1)$$

where p_{O_2} is the oxygen partial pressure, ΔG^0 is the change in standard Gibbs free energy, R is the universal gas constant and T is the absolute temperature. The corresponding plots are shown in Figure 4.1a for a variety of different oxides that are important in ferrous powder metallurgical systems with Cr as the principal alloying element and Mn and Si as common trace elements. The plots were calculated with the software HSC Chemistry 9.0. For conditions below each curve, dissociation of the oxide is favoured, and it will spontaneously break up into its reactants. A stable oxide can thus be dissociated by either raising the temperature and/or lowering the oxygen partial pressure. The positions of the curves in Figure 4.1a are related to the inherent thermodynamic properties of the elements and their oxides, resulting in greatly varying thermodynamic stabilities. The oxides of iron, FeO, Fe_3O_4 and Fe_2O_3, can be viewed as much less stable than the oxides of chromium, manganese and silicon. Spinel oxides of

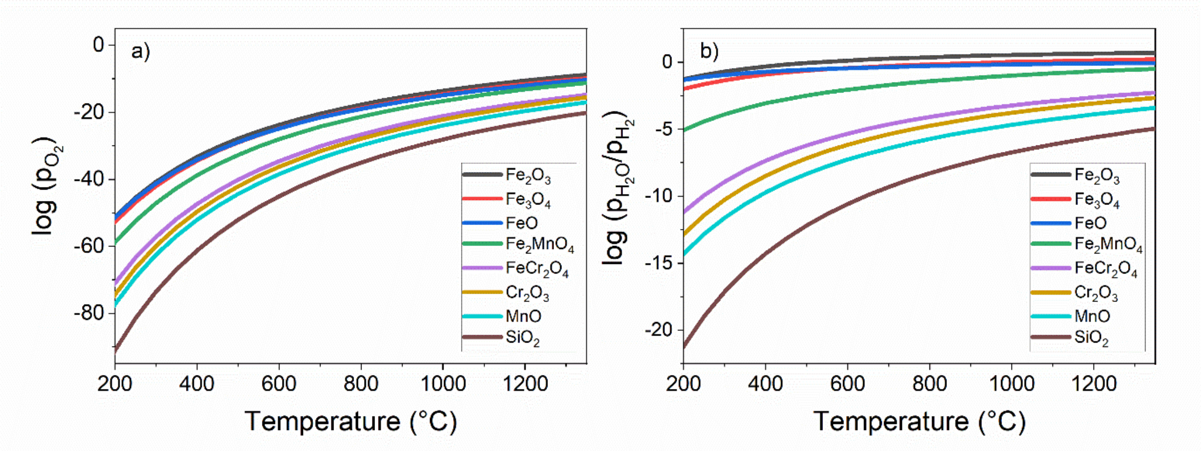

Figure 4.1: Oxide a) dissociation and b) reduction using hydrogen for some oxides commonly found in ferrous water-atomized powder grades used in PM. Calculated with HSC Chemistry 9.0.

mixed species, such as Fe_2MnO_4, $FeCr_2O4$, Cr_2MnO_4 and $MnSiO_3$ have intermediate stabilities [12,26], some of which are indicated in Figure 4.1.

The difficulties and costs associated with achieving the very high temperatures and/or very low oxygen partial pressures required for oxide dissociating makes it unfeasible for many industrial applications, although it has found use in e.g. the hard metal industry [75]. Instead, a reducing agent can be implemented which enables oxide reduction at considerably more favourable conditions. The most common reducing agents in powder metallurgical processing are hydrogen and carbon, with carbon being able to reduce oxides via both direct and indirect carbothermal reduction mechanisms.

Utilizing hydrogen for oxide reduction results in the following general expression

$$\frac{2}{y}M_xO_y + 2H_2 = \frac{2x}{y}M + 2H_2O \tag{4.2}$$

where M and O denote metal and oxygen, respectively and x and y balances the stoichiometry. The relationship between the partial pressures of the active gases then becomes

$$\frac{p_{H_2}}{p_{H_2O}} = \exp\left(\frac{\Delta G^0}{2RT}\right) \tag{4.3}$$

The thermodynamic stability is now presented as the ratio of partial pressures of water vapour and hydrogen gas at a given temperature. Figure 4.1b presents the corresponding plots for the relevant oxides. Reduction proceeds for conditions below each curve, meaning that a certain ratio of hydrogen to water vapour is required at a given temperature. Again, it is seen that the iron oxides more easily reduced than the corresponding oxides of chromium, manganese and silicon.

While hydrogen is commonly used as a low temperature reducing agent, high temperature reduction often relies on carbothermal reduction mechanisms wherein carbon and carbon monoxide act as the primary reducing agents [17,41]. However, the CO/CO_2 and H_2/H_2O ratios are always related for a given atmosphere via the water gas reaction ($CO + H_2O = CO_2 + H_2$) which means that they cannot be varied independently [26,37]. The thermodynamic stabilities of oxides are typically collected in a Richardson-Ellingham diagram, see e.g. [76], which provide an overview of the atmospheric conditions necessary to enable reduction of the oxide. It should be noted that thermodynamics alone does not explain when a specific oxide can be dissociated or reduced, only if it is possible from a thermodynamic perspective. The kinetics of a reaction, which explains at what rate it takes place, must also be considered to fully understand how oxidation, dissociation and reduction occurs. Of course, in real industrial sintering procedures, cost is also an issue with hydrogen being expensive and is further associated with handling risks. The common industrial processing gas for sintering of low-alloyed steels is therefore typically a mixture of N_2/H_2 in a 90/10 ratio, with carbon admixed to the powder both as an alloying element to reach required material properties and as aid in oxide reduction during sintering [13,32]. However, the dilution of hydrogen with nitrogen deteriorates the reducing capabilities of the processing atmosphere, thereby shifting oxide reduction to higher temperatures [26].

4.2 KINETICS OF OXIDE REDUCTION

While thermodynamics provide information about whether a reaction is possible or not at a given a set of conditions, kinetics tries to answer how fast that reaction proceeds. The time aspect is often of interest in industrial settings where it is important to be able to predict how long time a reaction takes, and what factors influence the reaction rate. Kinetic analyses are not traditionally associated with powder metallurgy but have been more common in other areas, such as initially dehydration of clays [77–79]. The analyses have since been adopted for studying for example pyrolysis and degradation of biomaterials and polymers [80–82], including thermal debinding processes of organic binder systems in MIM [83,84], and general PM [85]. In parallel, reduction of various metallic oxides such as nickel [86] and silver [87] oxide have been studied, along with several iron oxides; goethite, wüstite, magnetite and hematite [48,49,87,88] and milled iron ores [56,57] due to their importance in iron- and steelmaking. These studies collectively show the potential of the approach as adopted to areas related to powder metallurgy.

In this thesis, the kinetic analysis methodologies from these areas have been adopted for application to oxide reduction events that are important in powder metallurgical systems. This includes the reduction of the relatively low-stability iron-based surface oxide layer that covers all metal powder particles, removal of oxygen from internal oxides, and reduction of thermodynamically stable oxides that exist on the particle surfaces. The calculated activation energies provide information about how and at what rate the reactions proceed and can then be further utilized to make kinetic predictions of how the reactions proceed at extrapolated conditions. The analyses also indicate how the reactions are influenced by the presence of alloying and trace elements, the phase transformation of iron, and the restriction of mass loss that occur in powder compacts. At increasing temperature during a typical sintering cycle, multiple parallel reduction events also take place, thus further complicating the analyses. Nevertheless, an attempt is made to provide a generalized description of the mass loss behaviour of ferrous powder grades throughout the heating stage of a sintering cycle.

In practice, the kinetic analysis of a reaction involving mass loss can be analysed by performing a series of thermogravimetric experiments in which the heating rate is varied. The methodology for this analysis as applied to metal powder and pure iron oxides is detailed in the experimental methods section in Chapter 5. Several approaches for the analyses exist, where the Kissinger [77] and various isoconversional methods based on differential or integral thermoanalytical data are the most common [89]. The isoconversional methods assumes that the reaction rate is only a function of temperature [90], and that the reaction model is considered to be independent of temperature [91]. The following section includes a derivation of the equations that are used for the kinetic analysis and to calculate the apparent activation energies.

A solid state reaction can be described by the following equation [90]:

$$\frac{d\alpha}{dt} = k(T)f(\alpha) \tag{4.4}$$

where α is the extent of conversion of the reaction, *k(T)* is the temperature dependence and *f(α)* is the reaction model. The temperature dependent rate constant, *k(T)*, is taken as the Arrhenius equation

$$k(T) = A\exp\left(-\frac{E_a}{RT}\right) \tag{4.5}$$

where A is the pre-exponential factor, E_a is the activation energy and R is the gas constant. The kinetic parameters A and E_a are typically referred to as "effective" or "apparent" because of the difficulties in obtaining the true intrinsic parameters of a reaction. The non-specificity of thermal analysis measurements, process complexity and diffusion are key factors why this qualifier is advocated [90].

Non-isothermal temperature programs will be the focus of this study so that

$$\Phi = \mathrm{dT/dt} \tag{4.6}$$

where Φ is the heating rate assuming a constant value over the range of the temperature profile.

The reaction model $f(\alpha)$ in Equation 4.4 describes the conversion dependence of the process rate and can be expressed by several different models, the most common types being accelerating, decelerating, and sigmoidal. While kinetic analyses based on mathematical fitting of these models to experimental data is possible, the application can give rise to ambiguous results due to the failure to separate the conversion and temperature dependence of the reaction rate [90,92]. With Equation 4.4-4.6 combined, the expression for the rate of conversion becomes

$$\frac{\mathrm{d}\alpha}{\mathrm{dT}} = \frac{\mathrm{A}}{\Phi}\exp\left(-\frac{\mathrm{E_a}}{\mathrm{RT}}\right)\mathrm{f}(\alpha) \tag{4.7}$$

The Kissinger method [77] is derived from Equation 4.7, assuming a maximum rate of conversion where $d^2\alpha/dt^2=0$ [90], eventually leading to the expression

$$\ln\left(\frac{\Phi}{\mathrm{T_m^2}}\right) = \ln\left(-\frac{\mathrm{AR}}{\mathrm{E}}\mathrm{f}'(\alpha_\mathrm{m})\right) - \frac{\mathrm{E}}{\mathrm{RT_m}} \tag{4.8}$$

where T_m is the temperature at the maximum rate of conversion. While the use of the Kissinger method is straightforward, it is associated with some limitations such as requiring $f'(\alpha_m)$ to be independent of Φ. Strict independence is only accomplished for first order reactions, but can in practice be achieved with negligible variation for other reaction models. A visual inspection of the change in peak shape can be used to detect whether a significant variation exists [90]. Another limitation is that the Kissinger method only provides a single value of the activation energy, regardless of the kinetic complexity [90]. Consequently, it is possible that relatively unknown or less studied effects, such as the influence on mechanical compaction on the reduction of metal powder, can therefore be overlooked. In this study, the Kissinger method is used as a baseline providing a first quick look at the kinetics of the relevant processes. As a complement, an isoconversional method is used to reveal any further complexities of the reduction processes that may exist.

Integration of Equation 4.7 along with an approximation [93] of the temperature integral gives rise to the Kissinger-Akahira-Sunose (KAS) method [57,77,90,94] as

$$\ln\left(\frac{\Phi}{\mathrm{T_\alpha^2}}\right) = \mathrm{constant} - \frac{\mathrm{E_\alpha}}{\mathrm{RT}} \tag{4.9}$$

At a constant conversion α, the conversion-dependent activation energy E_α can then be estimated from the slope of a plot of $\ln(\Phi/T^2)$ vs. $1/T$. Further details about the methodology for the kinetic analyses can be found in Chapter 5.

Kinetic predictions

The calculated apparent activation energies can be used to compute predictions of the time required to reach a certain conversion or progress of the analysed reaction. Two equations derived from the Kissinger and isoconversional methods [90] are used to compute the predictions

$$t_0 = \frac{g(\alpha)}{A\exp\left(-\frac{E_\alpha}{RT}\right)} \tag{4.10}$$

and

$$t = \int_0^{T_\alpha} \frac{\exp\left(-\frac{E_\alpha}{RT_0}\right)}{\Phi\exp\left(-\frac{E_\alpha}{RT}\right)} dT \tag{4.11}$$

where t_0 and t denote the times required to reach full and partial conversion using the prediction methods, respectively. The term $g(\alpha)$ in Equation 5.2. is the integral form of the reaction model $f(\alpha)$ and can assume a variety of forms to represent the kinetics of the reaction, including for example the Avrami-Erofeev models, various types of diffusion models, etc., see for example [90] for a more complete list and closer description of the models. Results from the kinetic predictions can be found in Chapter 6.

4.3 DIFFUSION

Diffusion is of great importance in PM processes as it together with thermodynamics and kinetics governs how elements move across the material in search of equilibrium. As sintering is essentially just the movement of atoms, understanding diffusion is the key to understanding sintering.

Substitutional diffusion, specifically self-diffusion, is involved in the development of sinter necks while interstitial diffusion instead describes the movement of solute atoms that are much smaller than the host atoms and thus move faster. The diffusion processes are complicated by the fact that iron undergoes multiple transformations upon heating. For pure iron, a change from ferromagnetic to paramagnetic iron occurs at the Curie point of about 770 °C, followed by a change in crystal structure from BCC (ferrite, α) to FCC (austenite, γ) at about 910 °C. These changes influence the diffusion mechanisms, thus altering the rate at which atoms diffuse through the material. The change in self-diffusion in iron at the Curie point can be seen in Figure 4.2a, adapted from [95], highlighting the large increase in the diffusion coefficient. Conversely, the coefficients of grain boundary and dislocation pipe diffusion were noted to exhibit a significant decrease [96]. The diffusion coefficients also change at the α/γ transformation, with relatively small changes for grain boundary diffusion and a significant decrease in magnitude for volume diffusion in austenite [95,97]. An example can be seen in Figure 4.2b showing two plain iron samples sintered at 900 and 920 °C, respectively, and where the sintering rate as a function of crystal structure is clearly visible where the ferrite (BCC) allows for higher self-diffusion than austenite (FCC). Interstitial diffusion is also greatly affected by the crystal structure of the host lattice, with faster oxygen diffusion in BCC than in FCC as will be shown later.

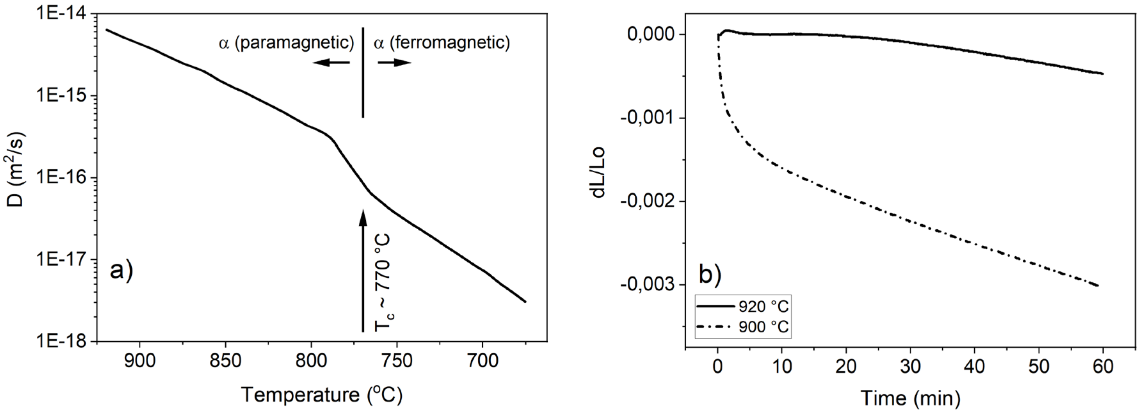

Figure 4.2: a) Volume self-diffusion in iron, highlighting the effect of the magnetic transformation on the diffusion behaviour. Adapted from: Buffington (1961), b) dilatometric curves of sintering of iron samples illustrating the effect of crystal structure on self-diffusion.

In addition to diffusion along surfaces, grain boundaries and through the crystal lattice, diffusion can also take place through dislocation pipes in the iron matrix [98]. While the contribution of pipe diffusion to the overall movement of atoms is generally expected to be low, it can have a significant effect at low temperatures and when the dislocation density in the material is high, such as after compaction of ferrous powder [60]. However, at elevated temperatures, recovery and recrystallization will render the effect from pipe diffusion negligible. Figure 4.3, redrawn from [99], summarizes the general trend regarding diffusion of various elements in iron; (i) interstitial diffusion coefficients are several orders of magnitude higher than the corresponding coefficients for substitutional diffusion, and (ii) diffusion generally shows a strong phase-dependence. However, diffusion of elements likely deviates from this simplification because of the presence of alloying and trace elements, and their respective effects on the host matrix and grain boundaries [96,97].

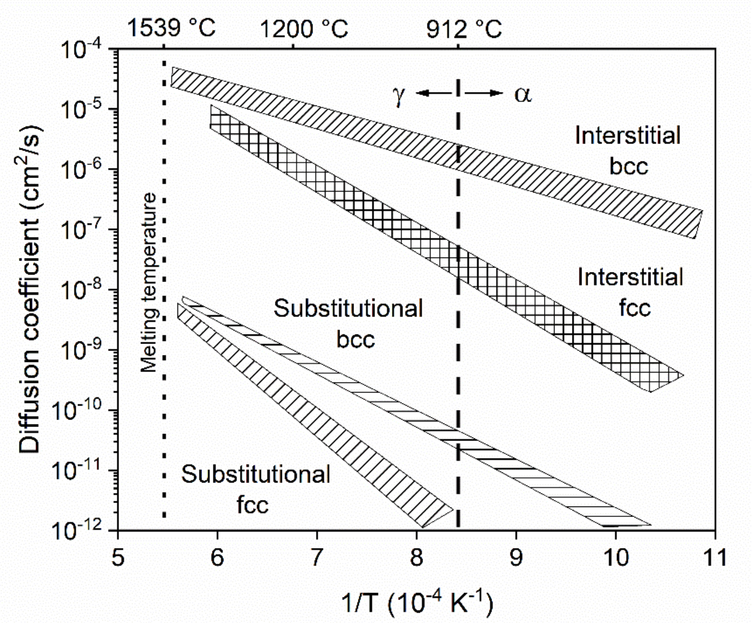

Figure 4.3: General overview of typical diffusion coefficients in iron. Adapted from: Föll (2018).

Chapter 5

MATERIALS AND EXPERIMENTAL METHODS

5.1 MATERIALS

The materials used for the experimental work in this thesis are water-atomized iron and steel powder grades produced and supplied by Höganäs AB, Sweden. For details about the production and properties of these powder grades, refer to Chapter 2 and 3, respectively.

The nominal chemical composition and oxygen content of the water-atomized powder grades can be seen in Table 5.1.

Table 5.1: Nominal chemical composition of the water-atomized powder grades

		Chemical composition (wt. %)					
Powder type	**Trade name**	**Fe**	**Cr**	**Mo**	**Ni**	**C**	**O (max)**
Pure iron	ASC100.29	Bal.	-	-	-	<0.01	0.11
Cr pre-alloyed	CrA	Bal.	1.8	-	-	<0.01	0.15
	CrM	Bal.	3.0	0.5	-	<0.01	0.15

An example overview SEM image of a typical water-atomized iron powder can be seen in Figure 5.1.

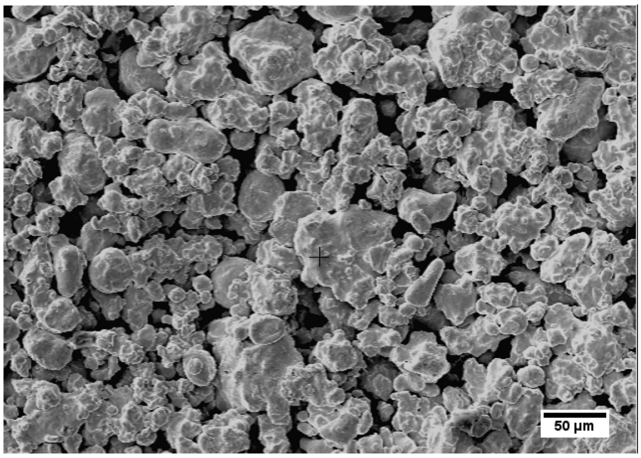

Figure 5.1: Overview of water-atomized iron powder ASC100.29. Note the particle size and irregular morphology.

The base raw material of the powder typically comes from metal scrap that is prepared for atomization. All impurities and trace elements cannot be removed prior to production and several elements outside the nominal specification exist in minor amounts. These elements are notably manganese, silicon and sulphur.

In Papers I-III, the standard fraction of ASC100.29 was sieved into three size fractions; <20, <45 and <75 µm to investigate the effects of particle size on reduction behaviour, surface chemical changes and sintering. These fractions are referred to as Fe20, Fe45 and Fe75 for the remainder of the thesis. A detailed chemical composition of the finer fractions, including the concentrations of impurity and trace elements, can be found in Paper I.

Reference powder oxides standards of iron and chromium were used for both oxide reduction and surface analysis. Details can be seen in Table 5.2.

Table 5.2: Reference oxide powder

Reference	**Supplier**	**Purity**	**Size**
Iron oxide	Sigma Aldrich	>99 % Fe_2O_3	< 5 µm
Chromium oxide	VWR Chemicals	98.9 % Cr_2O_3	-

5.1.1 Sample preparation

For several experiments in Chapter 6 and in the appended papers, the powder grades were simply used in their as-received conditions. While this provides a good overview of the chemical and physical processes that takes place while heating a powder, it does not reflect an industrial PM setting where the powder is in most cases compacted into useful shapes.

For Paper III, the water-atomized powder was first sieved to the appropriate size fractions, followed by mixing with 0.6 wt. % LubE for lubrication and 0.4 Wt. % graphite (Kropfmühl UF4) for some of the powder blends to provide a source of carbon. The mixes were then uniaxially compacted using three different compaction pressures. Cylindrical samples were produced, 11.3 mm in diameter and 13.5-14-7 mm in height, depending on the applied pressure. All operations were conducted at Höganäs AB. A tube furnace was subsequently used for the delubrication experiments. Green samples were loaded onto alumina crucibles and inserted into a quartz tube. The temperature was ramped to 450 °C with a heating rate of 10 °K/min. Argon (99.999 %) was flowing at 4 l/min to minimize oxidation. It should be noted that some oxygen pickup may occur but was deemed to have minor importance due to the subsequent sintering in hydrogen.

In Papers II and VI, powder was manually compacted using a small hydraulic press. Approximately 2 g of powder was put into a die cavity and compacted to densities in the range 6.6-7.4 g cm^{-3}, yielding discs about 10 mm in diameter and 3.5-4.0 mm in height, depending on the compaction pressure.

5.2 EXPERIMENTAL METHODS

Several different experimental methods were used in this thesis with special emphasis on thermoanalytical and surface analytical techniques and how they can be synergistically used together. Other techniques were used mainly to complement these analyses.

Thermoanalytical techniques

The thermoanalytical techniques were used to continuously monitor chemical (mass loss due to reduction of oxide) and physical (dimensional) changes in samples during sintering. In addition, the instruments were used as furnaces with well-controlled conditions in terms of temperature, heating rate and processing gas.

5.2.1 Thermogravimetric analysis

Thermogravimetric analysis (TGA) is a thermoanalytical measurement technique used to record the mass changes vs. temperature of a specimen to a very high degree of accuracy. Despite its relatively simple principles, TGA is a powerful method capable of giving information about oxidation, reduction, dehydration, pyrolysis, decarburization, etc., during arbitrary temperature programs which cannot otherwise be easily realized in an industrial setting. Another integral part of the function of the thermogravimetric equipment is its combination with atmosphere control (inert, vacuum, oxidizing, reducing etc.) that allows for a large variety of well-defined experimental setups.

The instrument used for all thermogravimetric work in this thesis was a simultaneous TGA/DTA/DSC thermal analyser STA 449 *F1* Jupiter from Netzsch (NETZSCH-Gerätebau GmbH, Selb, Germany) see Figure 5.2 for a schematic view. Experiments were done in a high temperature (up to 1550 °C) SiC tube furnace with a W-Re thermocouple for monitoring the temperature. Samples with masses of approximately 2000 mg were put in an Al_2O_3 crucible which was then loaded into the instrument. Reference samples of oxides of iron were also investigated, with masses of approximately 1000 mg due to lower density than the metal powder. The instrument was evacuated with a turbo pump to 10^{-4} mbar vacuum and flushed with high-purity argon (99.9999 %) up to three times before each measurement to minimize air residues. The analyses were done using the Netzsch Proteus software (v. 5.2).

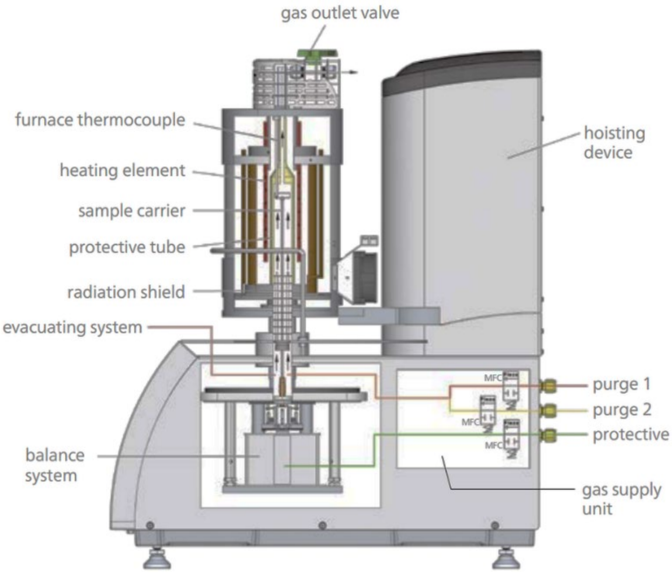

Figure 5.2: Schematic view of STA 449 F1 Jupiter from Netzsch. With permission.

The temperature programs used in this thesis lie in the temperature range 250-1350 °C. Low-temperature isothermal programs to study the surface oxide layer reduction were done at 250-350 °C with holding times of 0-180 min (Paper V). Dynamic heating programs to study oxide reduction and reduction kinetics at higher temperatures were done with heating rates of 10-50 K/min (Papers I, II, IV, V, VI, VII). The bulk of experiments were conducted in high-purity hydrogen (99.9999 %) to achieve ideal conditions for reducing atmospheres, but an industrial processing gas of N_2/H_2 (90/10 ratio) was also used (Chapter 6, Papers VI, VII). For the complete experimental details in each case, refer to the respective paper.

Effect of sample mass

The sample mass can itself influence the recorded mass vs. temperature signal for several reasons, including limitations in heat and mass transfer. The thermal inertia effect may lead to discrepancies in the recorded temperature and may further affect the calculations of the apparent activation energies since an increase in heating rate increases the temperature gradient between the thermocouple at the bottom of the crucible and the sample. This has been shown to be a common problem at least in the thermogravimetric and kinetic analyses of organic materials [80–82]. Restrictions in mass transport may also occur as the reducing hydrogen gas needs to be supplied to the powder bed of the crucible containing the powder. Conversely, water vapor needs to be effectively removed in the reverse direction. Consequently, the mass of the samples can have a significant impact on the thermogravimetric curves.

Ideally, the lowest sample mass possible will yield results closest to the intrinsic behaviour of the reaction, but in practice there will always be a compromise between accuracy and signal-to-noise ration. These concepts are illustrated in Figure 5.3a-d. In Figure 5.3a, thermogravimetric curves of samples with masses in the range 100-2000 mg. The smallest samples give rise to a large buoyancy effect along with significant noise, making the interpretation of the mass loss due to the initial surface oxide layer reduction step difficult. For sample masses of 2000 mg, the buoyancy effect was essentially mitigated. In Figure 5.3b, the differential TG (DTG) curves showing the mass loss rates are stack plotted which illustrates the shift in reduction peak position to higher temperatures with an increase in sample mass. The DTG curves are smoothened but despite that still show large levels of noise. Accordingly,

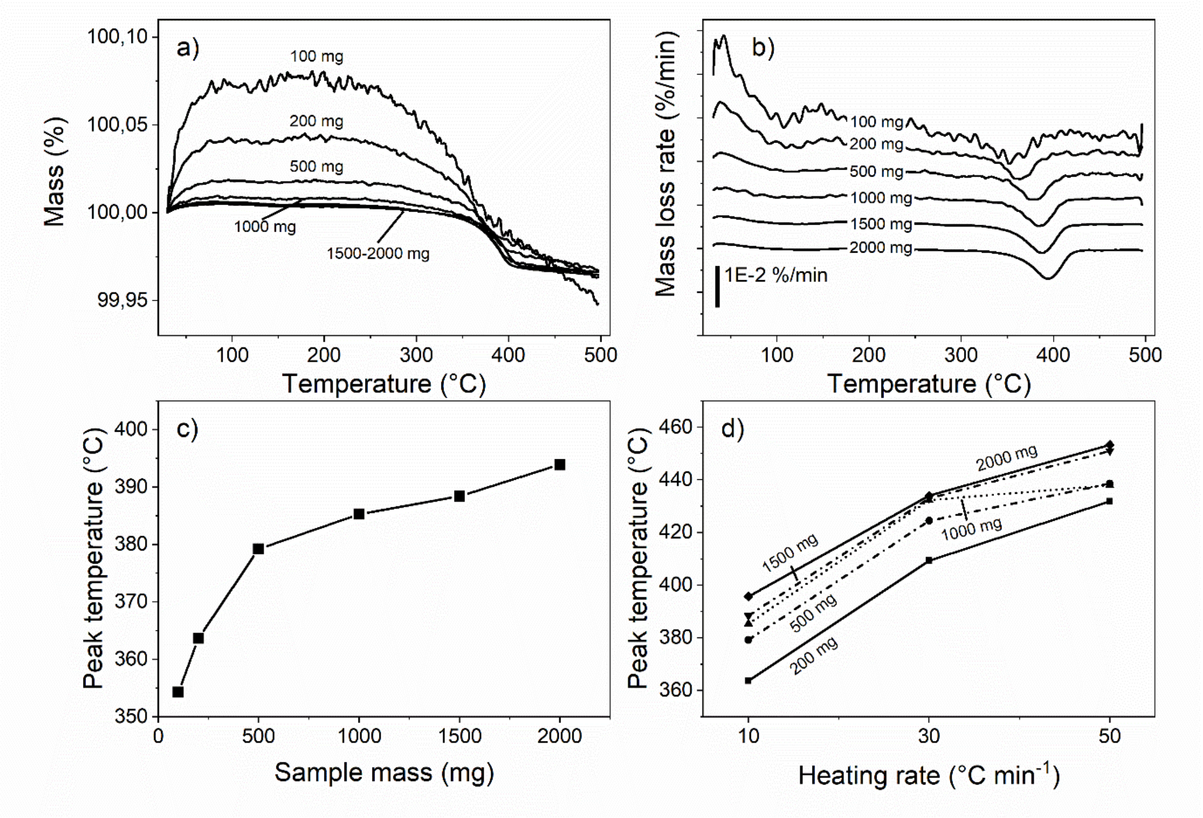

Figure 5.3: Low temperature region of typical TG curves. a) The strong buoyancy effect and b) significantly worsened signal-to-noise ratio can be seen for small samples. The large shift to higher reduction temperatures for large samples can be seen in c), along with the absence of an apparent heating rate dependence in d).

the resolution of small features is significantly improved with an increase in mass due to the improved signal-to-noise ratio. This is essential since the typical mass losses associated with the reduction of the surface oxide layer is on the scale of 0.01-0.03 % of the sample mass. The change in peak temperature position as a function of sample mass is illustrated in Figure 5.3c, indicating that the difference in reduction temperature may be up to 40 °C between samples with masses of 200 and 2000 mg. The extent of thermal inertia is explored in Figure 5.3d where the peak temperature as a function of heating rate is shown. As an increase in heating rate in the range 10-50 °C/min does not lead to large differences between samples of different mass, only a negligible amount of thermal inertia is present using this experimental setup. The reason for this is likely due to a combination of the heat transfer capabilities of hydrogen, the heat capacity of the metal powder and the overall efficient heating of samples in this instrument. The discrepancy in reduction temperatures between samples of 200 and 2000 mg is therefore attributed to limitations in mass transfer, i.e. access of hydrogen to the sample, penetration of the hydrogen into the powder bed, and the subsequent removal of the water vapor reaction product. Nevertheless, as neither heat nor mass transfer limitations cause a significant shift in reduction temperature with heating rate, as seen in Figure 5.3d, the anticipated underestimation in activation energy calculations [80] is expected to be mitigated to the extent possible.

While the difference between the peak temperatures of samples with varying masses may be up to 40 °C, the improved signal-to-noise ratio for larger samples was deemed to be more valuable for the analyses conducted in this thesis. For this reason, the standard sample mass for measurements is chosen to be 2000 mg. Another reason for using as large samples as possible with the current thermogravimetric setup is that the sintering conditions more closely resemble industrial practise, with reduction temperatures and calculated apparent activation energies approaching values that could be expected in real settings [82].

TGA-based kinetic analyses

The framework for the kinetic analyses outlined in Chapter 4 provides the basis for the details of the measurements and analyses described here, following recommendations of the International Confederation for Thermal Analysis and Calorimetry (ICTAC) [90,100]. As indicated previously, the kinetic analyses were done to describe the temperature influences and sensitivities of the relevant reactions in order to better understand the processes that take place during sintering of metal powder. Specifically, the progression of oxide reduction and oxygen removal and how reduction is affected by material and processing parameters were of interest.

The analyses were based on thermogravimetric measurements conducted on the Netzsch STA 449 *F1* Jupiter. The data points from the measurements are recorded with a relative mass and temperature throughout the heating stage of the sintering program. Whereas the Kissinger method from Equation 4.8 is relatively easy to apply, the isoconversional method of Equation 4.9 requires the selection of a conversion interval covering the reaction of interest. Each data point is then converted into a degree of conversion, α, based on the following equation

$$\alpha = \frac{\mathrm{m_i} - \mathrm{m(t)}}{\mathrm{m_i} - \mathrm{m_f}} \tag{5.1}$$

where m_i, $m(t)$ and m_f are the initial, instantaneous and final masses of the sample, respectively. The resulting curve of α vs. T_α then describes how the extent of the reaction proceeds from start to finish. By conducting multiple measurements at different heating rates, the shifted conversion curves vs. temperature can be plotted to show how the reaction responds to an

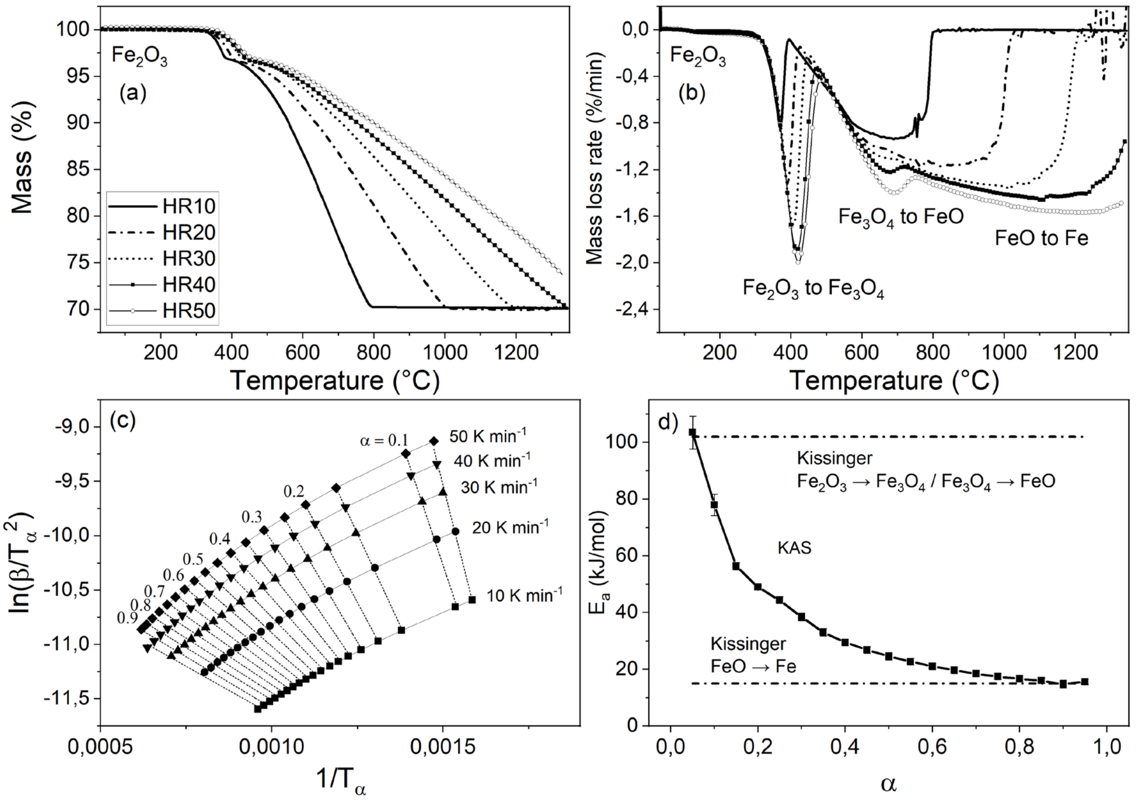

Figure 5.4: Example of reduction of Fe_2O_3 and a comparison of the KAS and Kissinger methods. a) Reduction curves of Fe_2O_3 at different heating rates, b) first derivative curves showing the rate of reduction, c) linear fitting of conversion steps at different heating rates, d) comparison of Kissinger method applied stepwise on the reduction and the KAS method applied over the entire reduction.

increase in heating rate according to Equation 4.9. At a constant conversion α, the activation energy E_α can then be estimated from the slope of a plot of $\ln(\Phi/T^2)$ vs. $1/T$. An example of such a plot along with a comparison with the Kissinger method can be seen in Figure 5.4a-d for the reduction of Fe_2O_3 in steps of $\alpha = 0.05$. Note that the selection of a conversion interval will determine how these plots represent the reaction and there is thus an improvement in resolution when treating the complete reaction as a stepwise reduction series rather than a single reduction step.

It should be noted that several limitations may be present in the kinetic analyses. While the thermal lag is shown to be relatively insignificant, cf. Figure 5.3, the selection of a conversion interval may be difficult if overlapping effects from other reactions or the α/γ transformation influence the reaction that is studied. Further details can be seen in paper II. Another drawback with the analyses is that the calculated apparent activation energies depend on the purity of the input materials and several processing parameters such as the processing gas and type of instrument [48–50]. However, since the experimental setup is kept constant, any inherent differences between the materials can be analysed.

5.2.2 Differential scanning calorimetry

Differential scanning calorimetry (DSC) is thermoanalytical technique employed to record the heat flow difference between the sample investigated and a reference. Because of this, the requirement is that the analysed event is either endothermic or exothermic, i.e. heat is either taken up or released by the sample. Processes that can be recorded in this way include phase transformations, chemical reactions, decompositions, magnetic transitions etc.

The instrument used for the DSC measurements is the same STA 449 *F1* Jupiter instrument that was used for the TGA, with the only difference being an S-type thermocouple and a DSC sensor installed for the measurements, cf. Figure 5.2. The sample masses are significantly smaller, in the range 100-250 mg, which are loaded into small Al_2O_3 crucibles. The experiments were run in high-purity argon (99.9999 %) up to 1350 °C with a holding time of 30 minutes and using a heating and cooling rate of 10 K/min.

An attempt to use DSC to monitor the heat released from compacted powder samples was done in order to characterize the extent of particle deformation and how the relaxation and recrystallization evolve with temperature, but nothing conclusive came out from these measurements using the current setup. Literature suggests that while DSC can be used to study deformation effects, the strain levels need to be significantly higher than what could be achieved by simple pressing of powder in the current case [101,102].

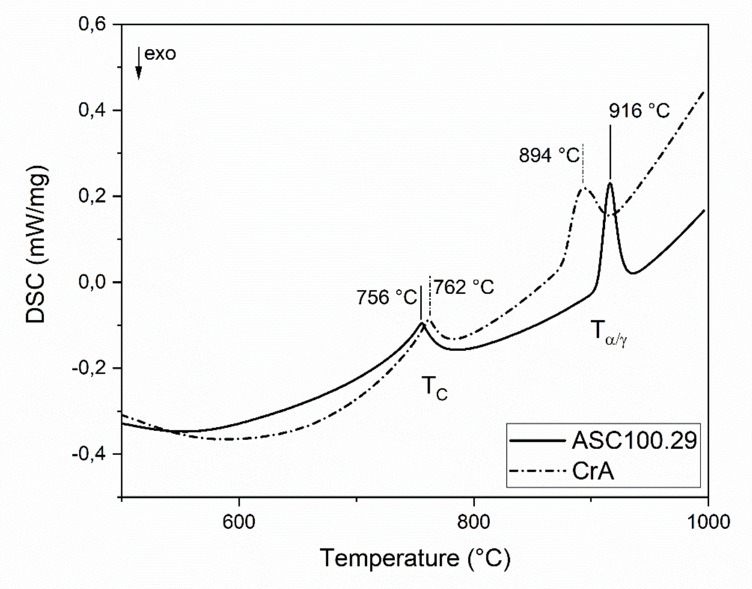

Figure 5.5: DSC of iron (ASC100.29) and steel (CrA) powder showing the temperatures of the Curie point (T_C) and phase transformation ($T_{\alpha/\gamma}$).

DSC was also used to provide information about the Curie points and phase transformation of the materials, see Figure 5.5, as both of these events influence the self-diffusion properties as indicated previously [95–97], thereby providing the temperature window where diffusion and sintering rates are potentially very high. Both the magnetic and phase transformations are in turn affected by the alloying composition, meaning that iron and steel powder do not show the same sintering behaviour in the late ferrite region, with potential implications for the sintering rates as well as the progress of oxide reduction from internal oxides.

5.2.3 Dilatometry

The dimensional changes of a specimen subjected to an arbitrary temperature program can be accurately measured by dilatometry. The instrument for the dilatometer experiments was a DIL 402 C from Netzsch (NETZSCH-Gerätebau GmbH, Selb, Germany). Similar to the TGA setup described previously, a W-Re thermocouple and a SiC furnace was used to allow experiments using reducing atmospheres at high temperatures, allowing for well-controlled sintering conditions. The sample is placed horizontally in the furnace tube after which the pushrod is positioned against the sample with a small force. The linear displacement of the pushrod is then converted into the measurement signal with high resolution. Like with TGA, the dilatometer is evacuated and flushed with high purity Ar gas prior to each measurement. For Figure 4.2b only, an induction-heated quench dilatometer was used to achieve a heating rate of 5 °C/s and a cooling rate of ~30 °C/s, thus allowing the samples to be brought to high temperatures rapidly in order to minimize sintering during heating.

Overall, the thermoanalytical techniques offer good flexibility and provide a convenient overview of the chemical and physical changes that occur during sintering of metal powder. The capabilities of the techniques are summarized in Table 5.3.

Table 5.3: Measurement capabilities of the thermoanalytical techniques

Technique	Mass	Phase transformations	Chemical reactions	Atmosphere control	Dimensional changes
TGA	X	-	Yes*	X	-
TG-DSC	X	X	X	X**	-
Dilatometry	-	Yes***	-	X	X

* Yes, if the chemical reaction gives rise to a change in mass

** DSC is run in inert atmosphere

*** Yes, if the phase transformation results in dimensional change

Surface analytical techniques

Surface analytical techniques were used to monitor and analyse changes in the surface chemistry of powder as a result of an increase in temperature or interaction with processing atmosphere. As indicated previously, a natural synergy exists between being able to record mass and dimensional changes in a well-controlled furnace, while subsequently being able to monitor any surface chemical changes that occurred during sintering.

5.2.4 X-ray photoelectron spectroscopy

X-ray photoelectron spectroscopy (XPS) is a surface sensitive technique that records the characteristic photoelectrons generated by X-rays directed onto the sample. Since the emitted photoelectrons will have slightly different binding energies depending on their chemical state, the XPS analyses can provide detailed information about the surface chemistry of the material. Tbe typical analysis depths are approximately 3-10 nm.

In this study, the surface chemical state of water-atomized ferrous powder was analysed using a PHI 5500 instrument (Paper I) and a PHI VersaProbe III instrument (Papers IV-VI), both equipped with a monochromatic Al Kα (1486.6 eV) X-ray source for the photoelectron generation. Powder samples, i.e. all samples that were neither compacted nor sintered, were either mounted on a carbon tape or lightly pressed onto Al-plates for the analysis.

Analyses and curve fitting were done using the software PHI MultiPak (v. 9.7.0.1) using asymmetric peak shapes and a Shirley background. Depth profiling was performed by successive analyses and ion etchings. The ion etching was done with an Ar^+ ion beam rastered over the analysis area yielding an etch rate of approximately 3 nm per minute. The etch rate was calibrated on a flat tantalum foil with 100 nm Ta_2O_5 oxide thickness. The etch depths thus refers to units of ion etching of Ta_2O_5. Nonetheless, the etch rates are assumed to be in reasonable agreement with etching of iron oxide [14]. It should be noted that while XPS depth-profiling using Ar^+ ions is routinely used for determining oxide layer thicknesses [14,38,43] on powder, issues may also arise due to inadvertently reducing iron oxides [103,104], thereby giving rise to incorrect ionic ratios in the profile. However, if just the ionic state changes without complete reduction to metal, the profiling results will likely only be slightly flawed. When performing XPS depth profiling on powder, it is also necessary to consider the powder shape which would otherwise influence the analysis. Models have therefore been developed in order to account for the spherical shape of powder [105] that allow e.g. positioning of the oxide/metal interface from the evolution of the bulk metal intensity as function of the nominal etch depth, thus allowing for an estimation of the thickness of oxide layer covering metal powder.

5.2.5 Auger electron spectroscopy

Auger electron spectroscopy (AES) is a surface analytical technique that detects Auger electrons emitted from the material. The interaction volume in this technique is relatively small; the use of a focused electron beam together with the surface sensitivity means that the Auger signal can be recorded for a small area around 10 nm and typically originates from 1-10 nm below the surface. Consequently, accurate measurements of surface chemical composition of small features can be performed. The sensitivity and analytical spatial resolution are also combined with secondary electron imaging, allowing for both imaging and analysis of small surface features. For the measurements performed here, a scanning PHI 700 instrument was used, with an accelerating voltage of 10 kV and a beam current of 10 nA.

A number of previous studies have utilized AES for depth profiling and surface analysis in various metal powder systems [14,37,39,106]. However, acquiring quantitative AES data from films of iron oxide, chromium oxide, or the solid solution of the two oxides can be difficult for several reasons such as the changing chemical environment for solid solutions of oxides that may cause a deviation from pure oxides [107]. Low kinetic energy peaks could be used to identify small differences in the composition of thin layers since the electrons typically originate from much smaller depths [108,109], but could not provide conclusive evidence in the present case.

Miscellaneous techniques

5.2.6 Scanning electron microscopy

Scanning electron microscopy (SEM) offers excellent information about the morphological and microstructural features of a material. Very high magnifications and spatial resolutions can be realized, providing surface topographical details by means of the secondary electron detector or elemental information (Z-contrast) using the back-scatter electron detector. One of the main strengths of the technique is its versatility and synergistic effects with e.g. energy dispersive X-ray analysis (EDX) and electron back-scatter diffraction (EBSD). However, microstructural investigations of highly ductile materials, such as plain iron powder, can be difficult as smearing of the material during sample preparation can cause superficial pores to close, giving inaccurate information when the density is cross-referenced with water-displacement methods [110]. The instrument used was a LEO Gemini 1500 FEG-SEM. Acceleration voltages of 15 kV were used with an In-lens detector, with a working distance of around 8.5 mm.

Energy dispersive X-ray analysis
The EDX can give qualitative chemical information about the surface and any features on it. The limitations are imposed by the large interaction volume of the electron beam with the sample. Thus, it is not an ideal technique when analysing the chemical nature of very small particulate features on powder surfaces. Nevertheless, its accessibility can provide a good overview.

Electron back-scatter diffraction
Electron back-scatter diffraction (EBSD) allows for collection of crystallographic information, including e.g. the crystal structure of a grain and its orientation and texture. In this study, EBSD was used for determining misorientation recorded from adjacent pixels to create a map of the misorientations across the analysed sample surface. The maps, which can span across particle cross sections can then be used to determine the prevalence of grain boundaries with a defined angle. By setting the map angle threshold to values commonly used to define low- and high angle grain boundaries, the location and density of such boundaries can be identified [72]. Low angle grain boundaries were here defined by a misorientation angle between 2 and 10°, whereas high angle grain boundaries were set to be at a misorientation angle > 10°. The EBSD maps used were acquired with a Nordlys II detector (Oxford Instruments). The acceleration voltage was 20 kV with a working distance of 15-20 mm. The step size was varied between 0.1 and 2 μm depending on the features to be analysed. All generated maps were processed using the Channel 5 software. The Kernel Average Misorientation (KAM) maps were constructed using a 3x3 grid with the centre pixel as reference. The KAM and GB maps depend on several things; step size, instrument settings, exclusion angles and smearing effects in the definition of the KAM maps. It should be noted that black areas can refer to unindexed areas which can originate from either pores or analysis errors. A comparison with the corresponding SEM image is therefore done to confirm that the unindexed areas are mostly pores.

5.2.7 Ball milling

A ball mill was used to induce structural defects into as-received powder grades. As has discussed previously, this has been shown to both alter the reactivity of iron oxide [56,57], and affect the sintering behaviour of compacted iron powder [40]. Ball milling was done using a Fritsch Pulverisette operated at 200 rpm with ceramic balls of 3.4 g and approximately 2.5 g of powder per run.

Chapter 6

SUMMARY OF RESULTS AND DISCUSSION

This chapter is a compilation of the studies done within the framework of the thesis and for the appended papers. The section is divided into two main parts; the first part covers the thermogravimetric and kinetic analyses while the second part deals with the sintering studies based on dilatometry. The surface analyses by XPS and AES are used to describe the chemical changes that occur during sintering and to complement the thermal analysis data. It should, however, be emphasized that the chemical and physical changes described in each section occur simultaneously during the heating stage of sintering and interact with each other. Consequently, it is difficult to completely decouple for example mass losses with sintering shrinkage.

6.1 INITIAL STATE OF THE AS-RECEIVED POWDER

While water-atomized iron and steel powder grades have nominal specifications, low levels of impurities and trace elements are inevitably present in the powder which is reflected in the surface chemical composition of the powder grades in their as-received conditions. As indicated earlier, the typical water-atomized particles have a highly irregular morphology and are predominantly covered by an oxide layer around 5-7 nm thin separating a minor amount of small particulate oxides enriched in Cr, Mn and Si, see e.g. [12,14] and Papers I and II [43,64].

An overview of a particle surface of as-received iron powder can be seen in Figure 6.1. AES was used to provide nanometer lateral resolution to the analyses in order to distinguish between the powder surface covered by the oxide layer and the oxide particulates dispersed on the

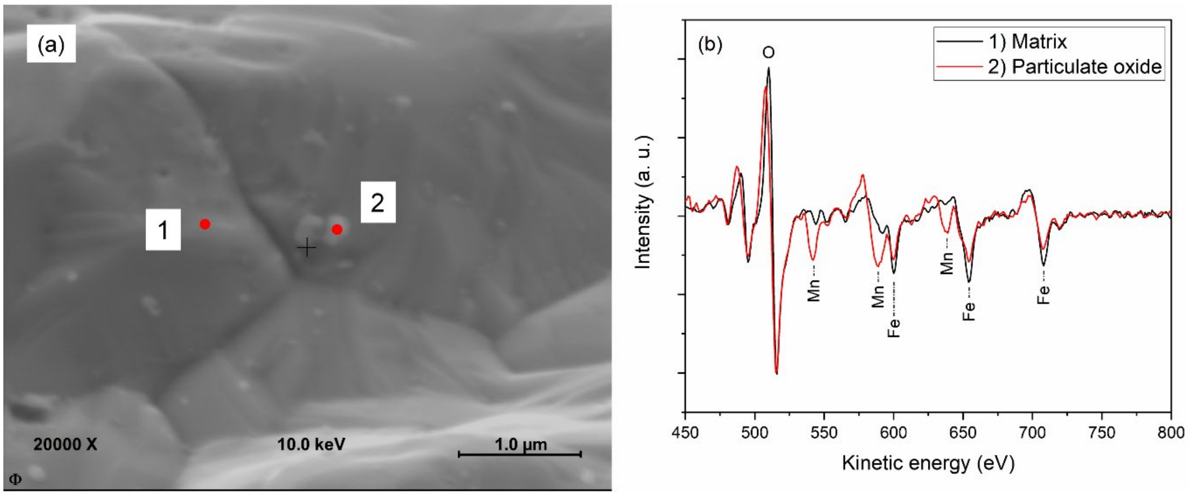

Figure 6.1: AES analysis of a water-atomized iron powder surface. a) overview image with two analysis points of the powder matrix and a particulate oxide, b) AES spectra of the two points. From Paper II.

surface. Whereas the oxide layer present on the surface is found to be mainly consist of iron oxide, particulate oxides can have significant content of other elements, like manganese. These results illustrate the generic picture of the as-received powder, but depending on powder characteristics and alloy composition, the exact nature of the particulate oxides can vary.

The as-received state of the powder changes during the heating stage of the sintering cycle as the surface oxide layer and oxide particulates are sequentially reduced due to the altered thermodynamic and kinetic conditions that arise during sintering. These situations are readily achieved in the thermogravimetric and dilatometry setups detailed in Chapter 5 and form the basis of the oxide reduction and sintering studies conducted in this thesis.

6.2 THERMOGRAVIMETRIC ANALYSIS

An example of a thermogravimetric curve for heating of water-atomized iron powder (ASC100.29) in pure hydrogen can be seen in Figure 6.2. Three principal temperature regions, can be identified; (i) the first region related to the reduction of the surface oxide layer (in the range 300-500 °C), (ii) a region of mass loss due to reduction of less stable internal and particulate oxides where the metal powder particles exhibit the ferrite form of iron with a BCC crystal structure (between 500 °C and the α/γ transformation), and (iii) a high temperature region with extensive mass loss mainly due to reduction of the more stable oxides (from the α/γ transformation and upwards).

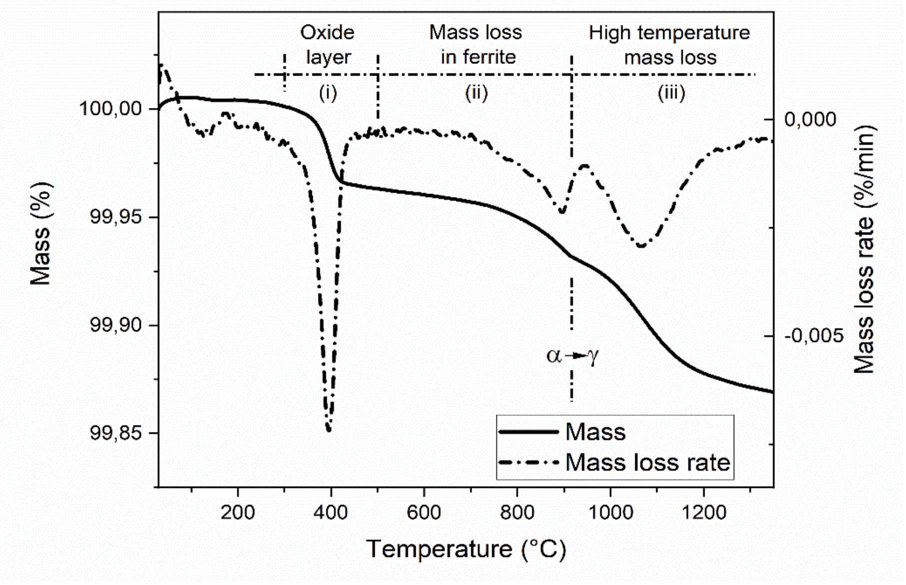

Figure 6.2: Thermogravimetric curve of ASC100.29 heated at 10 K/min in pure H_2.

Several factors influence the mass losses recorded by thermogravimetry, including material characteristics like initial condition, chemical composition and particle size as well as experimental parameters such as the processing gas and particle deformation encountered for example in powder compaction. The influences are detailed in the respective sections below.

6.3 THE SURFACE OXIDE LAYER

As introduced previously, iron and low-alloyed steel powder particles are largely covered by a thin surface oxide layer that contains a significant fraction of the total oxygen in the powder. The characteristics of this layer, in terms of its thickness, composition and how it responds to changes in temperature and atmosphere composition, and its role in sintering, has been a part of the studies in all appended Papers I-VII. The reduction of the surface oxide layer is easily distinguished in the typical thermogravimetric curve of water-atomized iron powder in Figure 6.2, with a distinctive mass loss at around 400 °C for iron powder. However, the temperature and magnitude of the reduction event is influenced by material and experimental parameters as indicated previously. How these factors influence the surface oxide layer reduction is discussed in the following subsections.

6.3.1 Oxide layer thickness

The oxide layer thickness of as-received water-atomized iron powder was found to be 6-7 nm in Paper I for powder sieved to <20, <45 and <75 μm. This value, estimated based on XPS depth profiling, was in line with previously derived thicknesses of surface oxide layers on chromium pre-alloyed steel powder grades, see e.g. [14,46]. It should be mentioned that the analyses are complicated by sputtering effects in which Ar^+ ions will inadvertently reduce oxides by preferential etching of oxygen, thus there is a risk of overestimating the presence of metallic iron as a result of the ion etching [103]. In Paper I it was also shown that the mass loss of the initial reduction step as recorded by thermogravimetry at around 400 °C in H_2 at a heating rate of 10 K/min could be coupled directly to the measured specific surface area, iron oxide density and oxygen content, to yield an oxide layer thickness estimation that showed a relatively good correlation with the values derived from XPS depth profiling. The estimate was done using the following expression:

$$m_{TG} = t_{oxide} \cdot \mathrm{BET} \cdot \rho_{oxide} \cdot 0.3 \tag{6.1}$$

where *m* is the mass loss recorded by thermogravimetry, *t* is the oxide thickness, *BET* (Brunauer-Emmet-Teller) is the measured surface area per unit of mass, ρ is the oxide density and 0.3 is the mass fraction of oxygen in Fe_2O_3. This value will vary depending on the chemical composition of the oxide, with the oxidation state determined by XPS. One limitation arises if the surface area cannot be assumed to be approximately constant over the course of reduction such as if the oxide layer thickness is comparable to the radii of the powder particles or there is extensive surface diffusion. However, in the present case, the oxide thickness is much smaller than the average particle radius and thus no such effect is encountered.

Although the oxide layers on as-received iron and steel powder grades are similar in thickness, they are considerably thicker than what is expected from a native oxide forming on a freshly exposed metal surface which is about 3 nm on high purity iron [111]. Consequently, commercial powder grades, after powder production, annealing and handling, have an oxide layer that does not directly correspond to a native oxide layer. The implications of these differences are detailed in later sections.

6.3.2 Effect of particle size

Smaller particles have a larger specific surface area than coarse particles. Consequently, more oxygen is bound to the surface and is available for removal by hydrogen during the reduction process. This leads to the difference in magnitude of the initial mass loss seen in Figure 6.3a-b for fine and standard fraction powder. A particle size dependence where the oxide layers on finer particles are reduced at lower temperatures is indicated in the inset in Figure 6.3b and may be connected to the increased surface area and surface energy. However, no significant effect of the differences in particle sizes can be seen on the thermogravimetric curves at

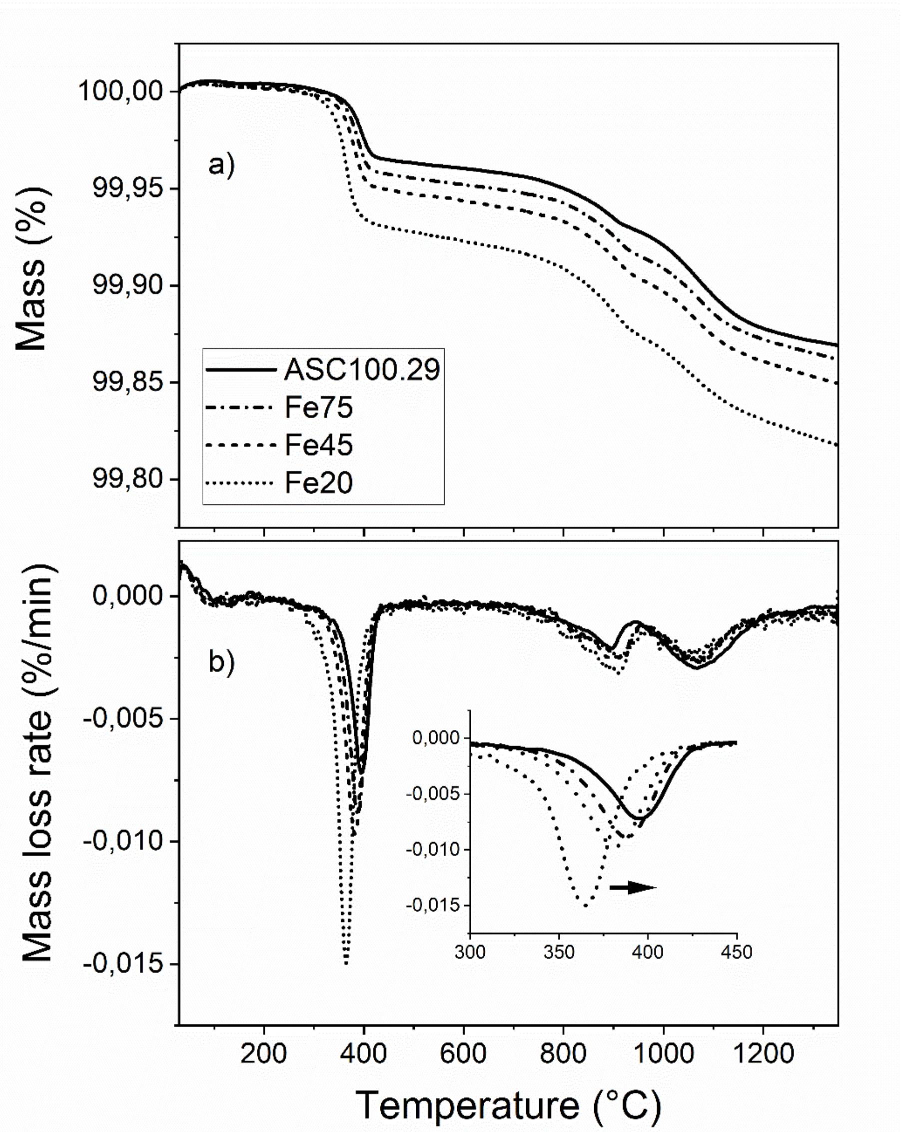

Figure 6.3: a) TG and b) DTG of powder run in pure hydrogen at 10 K/min. The curves show the effect of particle size on reduction of water-atomized iron powder. The inset shows the lowered peak temperature of reduction for finer powder fractions.

intermediate and high temperatures, although smaller particles were shown to have slightly higher content of Mn and Si oxides on their surfaces (Paper I). Some further details can be found in Papers I and II.

6.3.3 Surface oxide layer composition

The oxide layer has generally been considered to be a homogeneous oxide of predominantly Fe_2O_3 covering the surface of the powder particles, both for iron powder and chromium pre-alloyed grades [12,14,43]. However, it is likely that the composition reflects the alloy composition, especially if the oxide is formed at low temperatures where atomic mobilities are limited [47]. Consequently, an oxide forming on a nominally pure iron powder can be expected to be slightly different compared to an oxide forming on a pre-alloyed powder grade. The implications of the differences in composition between the powder grades can be seen in Figure 6.4a-b showing the reduction curves of ASC100.29, CrA and CrM heated at 10 K/min in pure hydrogen. The results indicate a significant lowering of the reduction temperature for the pre-alloyed grades. This change is believed to originate from a combination of a small alteration in

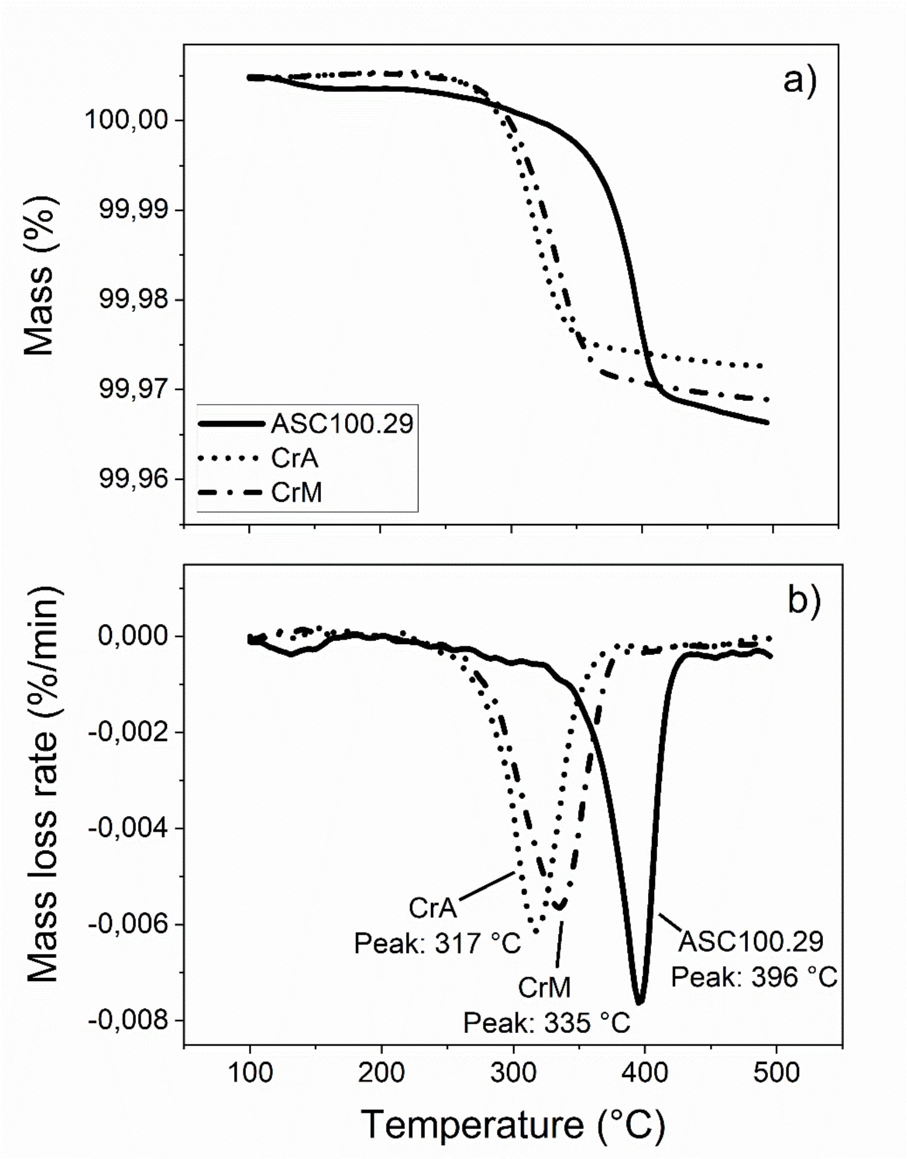

Figure 6.4: Thermogravimetric curves showing the differences in surface oxide layer reduction temperature between ASC100.29, CrA and CrM. a) TG curves, b) DTG curves. From paper V.

oxide layer composition [112] as well as the differences in the initial, as-received, powder states which are a function of the powder atomization, annealing, and subsequent handling. In addition to a change in reduction temperature, the kinetics of the reduction process is also altered in the presence of alloying elements or when the powder grades are 'normalized' in two sequential reduction steps as will be shown later. See Paper V [113] for further details regarding the analysis.

The chemical differences between the powder grades, as inferred by the thermogravimetry results in Figure 6.4, were further investigated by XPS. The analyses were conducted to study the surface chemical composition of as-received powder grades, and are described in detail in Papers I, IV, V and VI. Analyses of water-atomized iron powder reveal that predominantly Fe^{3+} ions are present, with only minor contribution from Fe^{2+}. This chemical state is characteristic of hematite, Fe_2O_3, rather than magnetite, Fe_3O_4, or other compounds in which iron would be present as Fe^{2+} to a large extent. The narrow scan XPS spectra of the Fe 2p region for ASC100.29, CrA and CrM can be seen in Figure 6.5a along with a reference Fe_2O_3

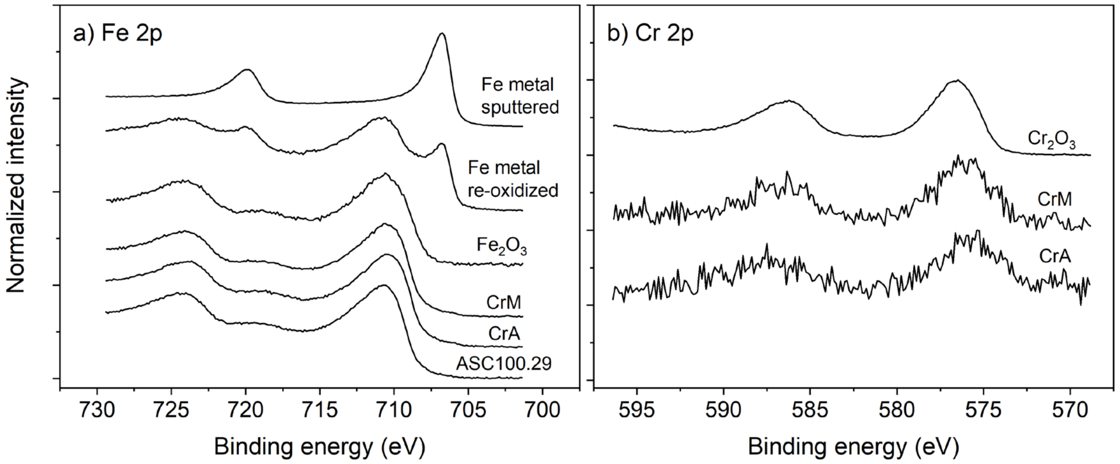

Figure 6.5: XPS narrow scans of the a) Fe 2p and b) Cr 2p regions for ASC100.29, CrA and CrM. Reference samples of Fe_2O_3 *and* Cr_2O_3 *powder are included. For iron, a metal plate was also sputtered and re-oxidized for a reference for metallic iron.*

powder and metallic iron that was first ion etched to clean metal, analysed, and subsequently left to re-oxidize before it was analysed again. The oxide and metal references give the peak positions of Fe^{3+} and Fe^0, respectively. Some ambiguity regarding the presence of Fe^{2+} ions of FeO or Fe_3O_4 in the oxide layer exists. Previous investigations have reported minor contributions from Fe^{2+} although the major fraction has been Fe^{3+} [14,25,38]. However, the satellite peak at approximately 719 eV is indicative of Fe_2O_3 [114].

As shown in Figure 6.5a, no significant differences in the Fe 2p spectra between the powder grades can be seen, and their Fe 2p spectra are similar to that of Fe_2O_3. However, the chromium pre-alloyed grades also contain 1.8-3.0 wt. % Cr. Analysis of the Cr 2p region in Figure 6.5b yields that surface chromium oxide is present on all powder grades. However, one complicating factor with the analysis is that the powder grades initially contain small oxide particulates on the particle surfaces, cf. Figure 6.1. These particulates typically contain strong oxide-forming elements such as Cr, Mn and Si [14], and will inevitably contribute to the recorded XPS signals. Because of this, it is difficult to assess to what extent the Cr signal comes from the oxide particulates or from the surface oxide layer. Additionally, since Fe_2O_3 and Cr_2O_3 are soluble in one another and a single phase oxide can exist over the whole Fe-Cr range according to the formula $(Cr_{1-x}Fe_x)_2O_3$ [107], it cannot be disregarded that the Fe_2O_3 surface layer may contain Cr^{3+} for the Cr-containing powder grades and thereby reflect the alloy composition as indicated earlier.

Nevertheless, an attempt to investigate the presence of non-Fe cations in the oxide layer was presented in Paper V, see Figures 6.6a-c, with an extension of the analysis for ASC100.29 provided here, see Figures 6.7a-e. Figure 6.6a shows the reduction of the surface oxide layer for CrA along with points at intermediate temperatures in the range 250-400 °C that represent samples taken for XPS analyses. Figures 6.6b-c show the corresponding narrow spectra of the Fe 2p and Cr 2p regions, respectively. It should be noted that the samples were exposed to air during the transfer between the thermogravimetric and XPS analysers, thus re-oxidizing the powder so that a native oxide layer about 3 nm thin is formed. Since the small thickness of the oxide layer allows for detection of photoelectrons from the metal matrix, the reduction progress can be identified by the emergence of a small Fe^0 peak (cf. Figures 6.5a and 6.6a) at the low

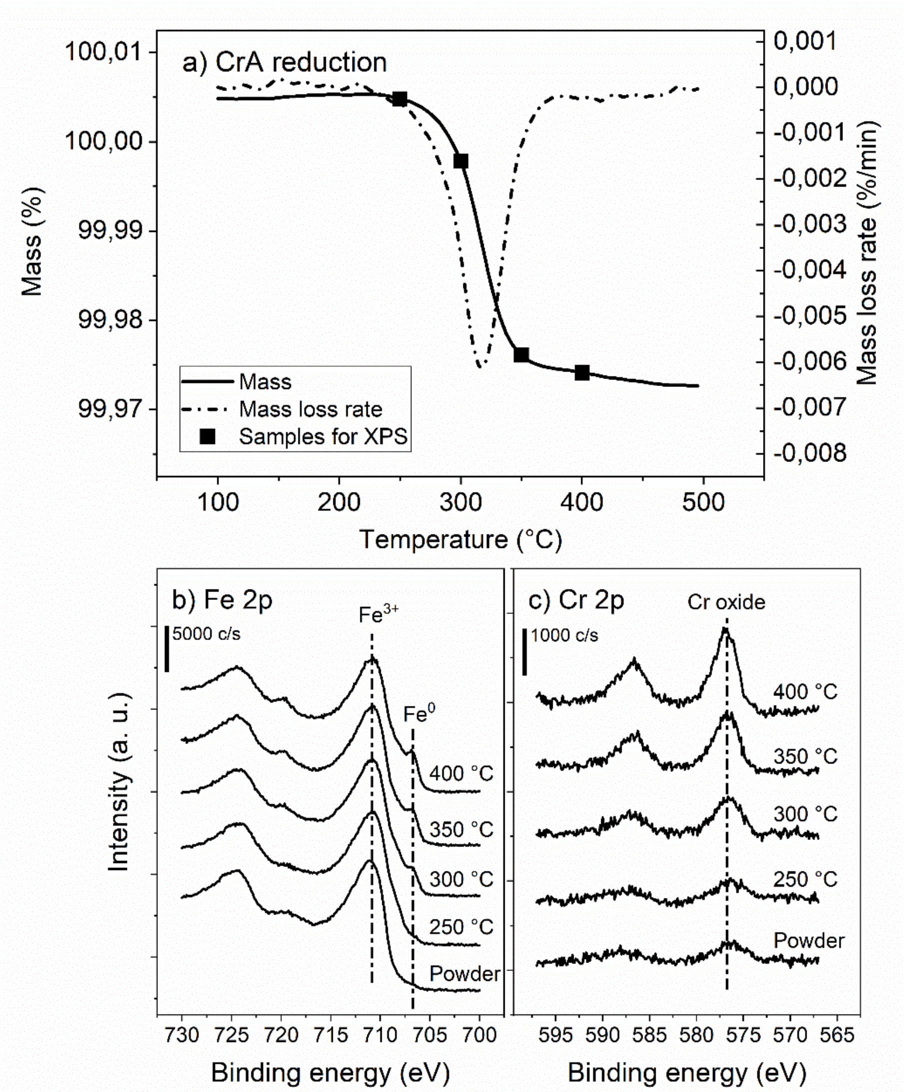

Figure 6.6: a) Thermogravimetric reduction curves of CrA along with sampling points at intermediate temperatures for XPS analyses, b) XPS Fe 2p region, c) Cr 2p region. From Paper V.

binding energy side of the Fe^{3+} peak for samples heated to between 250 and 400 °C. The spectra show good correlation with the reduction curve in Figure 6.6a and signifies that the oxide layer is progressively removed during heating, with full removal at 350-400 °C. For the Cr 2p region, a progressive increase in Cr oxide intensity is clearly obtained with increasing temperature and oxide layer removal. The results suggest that the Cr oxide is present either in the oxide layer itself or close to the metallic matrix of the particles. Due to the low temperatures in the investigation, diffusion is believed to be less significant, but a certain supply of Cr by grain boundary diffusion cannot be disregarded.

The case is slightly different in the case of water-atomized plain iron powder, see Figure 6.7a-e. Whereas the metallic shoulder progressively grows in Figure 6.7b (cf. Figure 6.6b), the small Cr oxide content in the powder remains constant throughout the reduction at these low temperatures (6.7d), see Paper IV [115] for some further details. Instead, some changes occur in the Mn content which is initially to some extent bound to sulphur as a sulphate/sulphite, cf. Figure 6.7c and 6.7e [38]. This compound is then removed at elevated temperatures (<325 °C) in a reducing atmosphere, with an emerging peak of sulphide indicating the presence of MnS, see Figure 6.7e [38]. After removal from the furnace and transfer to the XPS analyser, the

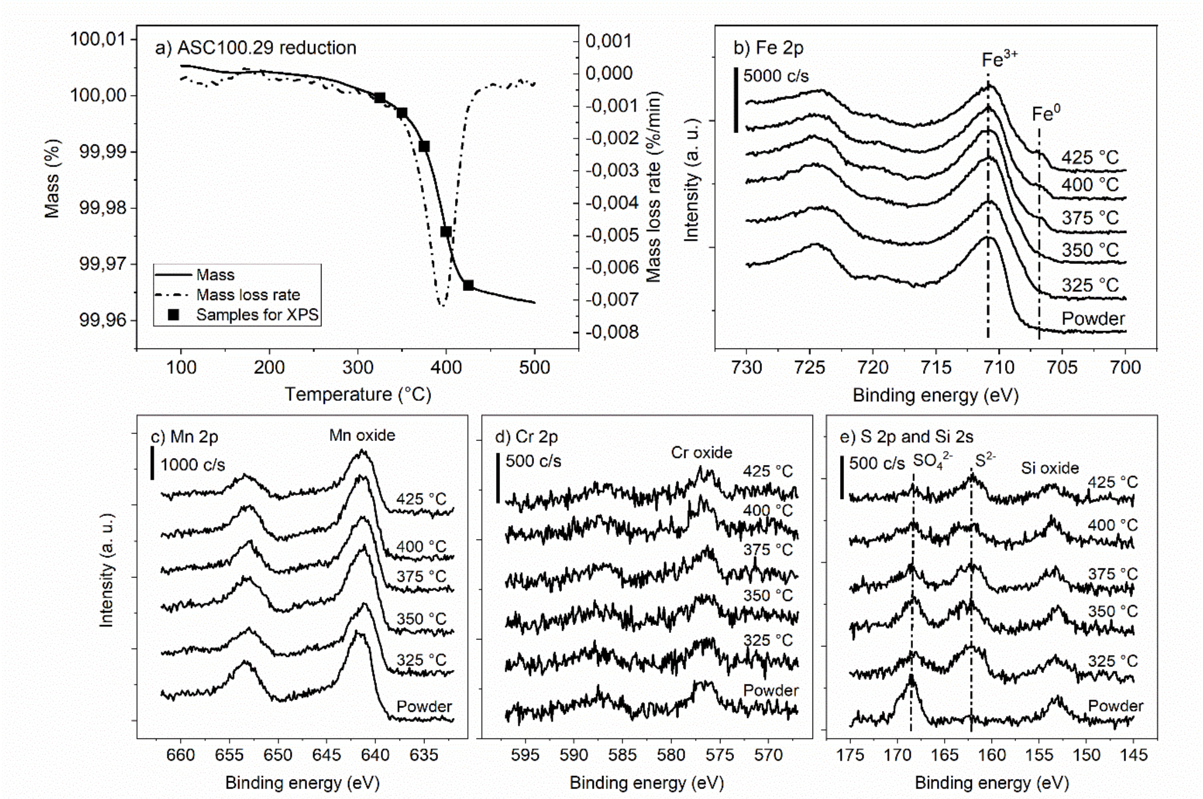

Figure 6.7: a) Thermogravimetric reduction curves of ASC100.29 along with sampling points at intermediate temperatures for XPS analyses, b) XPS Fe 2p region, c) Mn 2p, d) Cr 2p, e) S 2p and Si 2s.

sulphide partly re-oxidizes back to sulphite/sulphate again. While the removal of the initial sulphate cannot be detected by TGA, c.f. Figure 6.7a, some interaction between sulphate reduction, sulphide formation, and the reduction of the surface oxide layer cannot be disregarded. However, if an influence exists, it is believed to be present to a much lesser extent than the effect of chromium in CrA and CrM.

6.3.4 Influence of processing gas

The processing gas can have a profound influence on the reduction curves observed in Figure 6.4, with hydrogen being a necessary component that enables surface oxide reduction at low temperatures[17,26,41]. Diluted hydrogen, as in the typical N_2/H_2 (90/10 ratio) standard industrial processing atmosphere [34], causes a shift in the reduction rate maxima by about 100 °C upwards in temperature along with a reduction peak broadening for both CrA and ASC100.29, see Figure 6.8. The reason for this change may be connected to several parameters, including limitations in mass transport of the gas mixture to the powder bed, and also reflect the deteriorated H_2/H_2O ratio from dilution and slightly lower gas purity (cf. Figure 4.1b). In extension, the dilution may also cause a lowering and underestimation of the calculated apparent activation energy of reduction caused by the shift of the reduction peaks as indicated in Chapter 5. The shift in reduction to higher temperatures also risk interference with sintering by inhibiting neck development and leading to oxide entrapment. Completely removing hydrogen from the processing gas prohibits reduction altogether since no reducing agent is available. The oxides then need to be removed by dissociation which requires very low partial pressures of oxygen at these low temperatures (cf. Figure 4.1a). In real industrial PM settings, carbon is added which enables reduction by carbothermal mechanisms. However, since these only become active at elevated temperatures [26], not having hydrogen present would inevitably leave the surface oxide layers intact well after the onset of sinter neck development, thus potentially causing further entrapment of oxide residues.

6.3.5 Native oxide layers on metal powder

The oxide layers that exist on as-received, commercially available powder grades do not necessarily correspond to the oxides that form naturally on a metal surface, as indicated earlier.

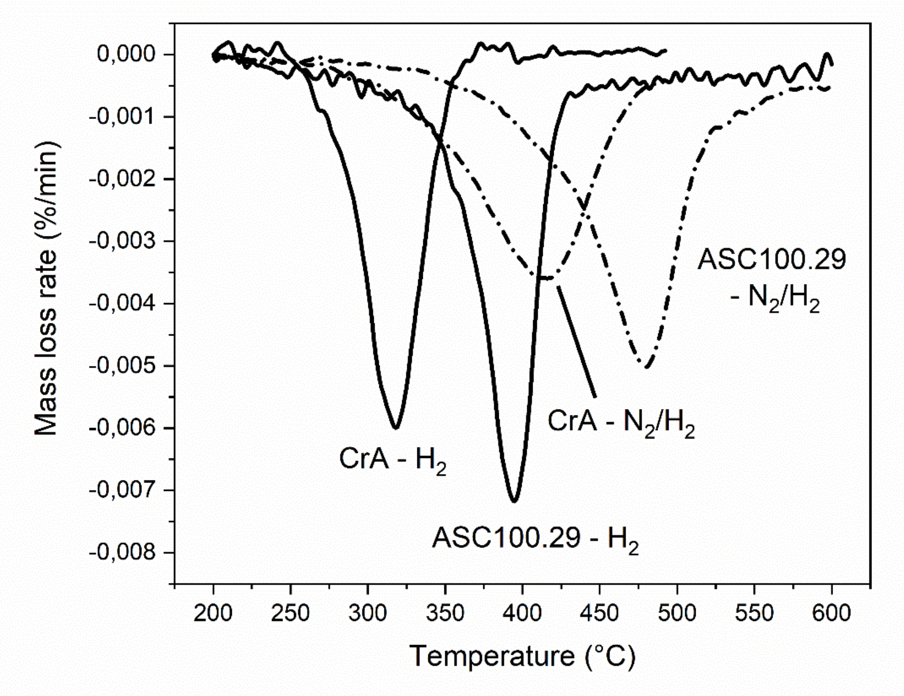

Figure 6.8: Thermogravimetric curves of CrA in H_2 and N_2/H_2 (90/10).

The discrepancy in oxide layer thicknesses detailed above, with a native oxide layer of 3 nm compared to typical as-received powder grades with 5-7 nm oxide thicknesses, can be explained by the origin of the oxide layer. Whereas the native oxides are simply formed at room temperature, the oxide layers on commercial powder are a result of the atomization, annealing and subsequent handling of the powder.

To investigate the native oxide layers formed on water-atomized iron and steel powder, and the reduction behaviour of those layers, a series of low-temperature thermogravimetric reduction experiments were conducted, see Figure 6.9. Powder samples were heated in hydrogen to 500 °C, at which point the oxide layers on the as-received powder are completely removed, followed by subsequent cooling in the hydrogen to prevent re-oxidation. This effectively “normalizes” the powder so that when the furnace chamber is opened, a thin native oxide layer will immediately form on the metal surfaces at room temperature. The samples were then re-heated using the same heating program to complete the oxide reduction sequence again. The differences that were observed show two things; (i) the magnitude of the second cycle oxide layer reduction is significantly smaller compared to that of the first cycle of reduction, indicating that the oxide layer thickness is also reduced, likely to the expected 3 nm. (ii) the reduction events take place at significantly lower temperatures for re-oxidized powder; about 100 °C for water-atomized iron and about 50-60 °C for the two chromium-alloyed steel

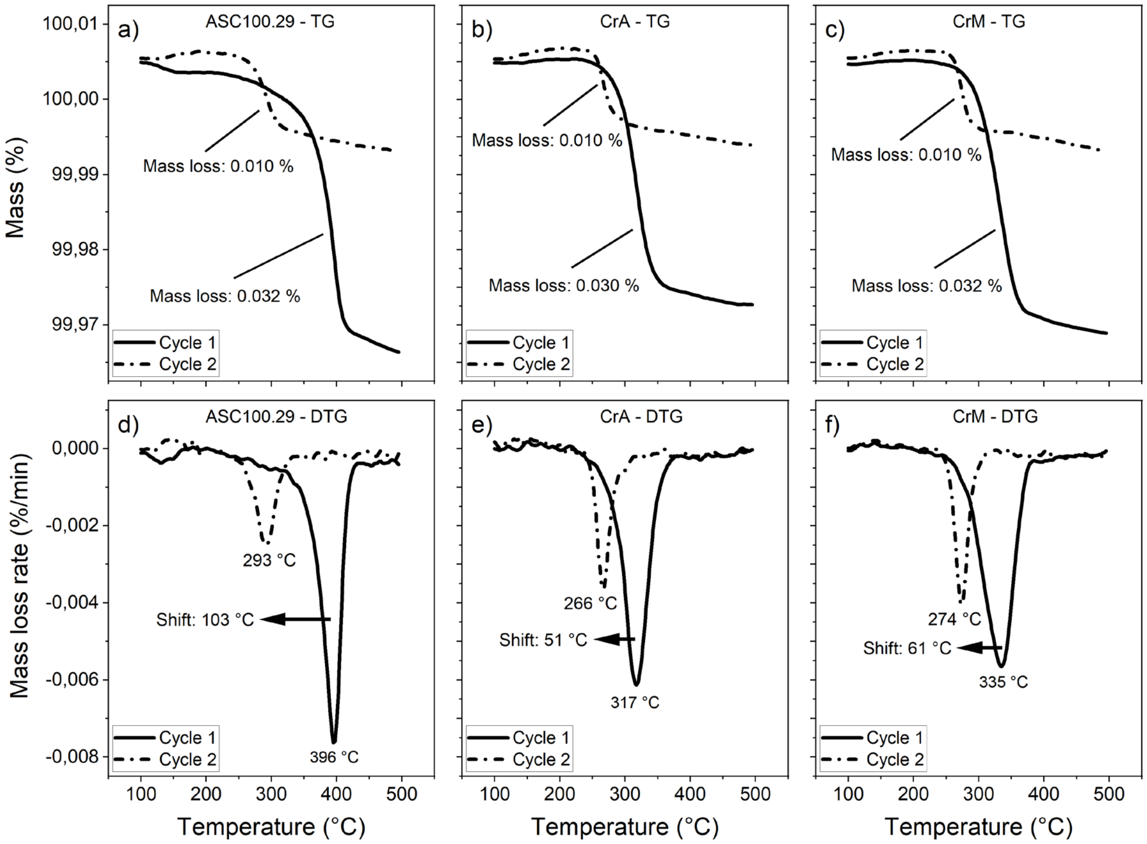

Figure 6.9: Iron and steel powder grades heated to 500 °C in thermogravimetric reduction cycles. a) and d) TG/DTG of ASC100.29, b) and e) CrA, c) and f) CrM. Cycle 1: As-received powder. Cycle 2: Re-oxidized powder with native oxides. There is both a decrease in magnitude and a lowering of the reduction temperature for the native oxides. The commercial powder grades thus deviate from the idealized case of oxides formed on metal powder surfaces at room temperature. From Paper V.

powder grades. These results indicate that the as-received powder grades are covered by oxide layers that exist in a configuration in which they are more stable than their corresponding native oxide layers on the powder surfaces. The origin of this effect may be a combination of structural and compositional differences.

6.3.6 Effect of compaction and mechanical deformation

In an applied industrial setting, the powder grades are mixed with lubricants and go through the conventional PM process as outlined in Chapter 2. This involves a compaction step in which the metal powder particles are rearranged and subsequently deformed as the powder assumes the shape of the die cavity. The deformation of the metal particles readily introduces dislocations and strains in their metallic matrix, as can be inferred by EBSD or XRD measurements [23,116,117]. However, the oxide layer can itself be affected by the mechanical action which in turn can influence its reactivity [56,57] and change its structure [118]. To investigate possible changes in powder reactivity induced by deformation, the different powder grades were subjected to ball milling in a preliminary study of the effect of deformation. The results can be seen in Figure 6.10 for ASC100.29, CrA and CrM milled for 4 and 16 h. From the top row it is seen that the magnitude of mass loss increases with milling time. This is expected to occur both because of the creation of new particle surfaces that re-oxidize as well as due to a growth of the oxide layer thickness. The bottom row of Figure 6.10 reveals a

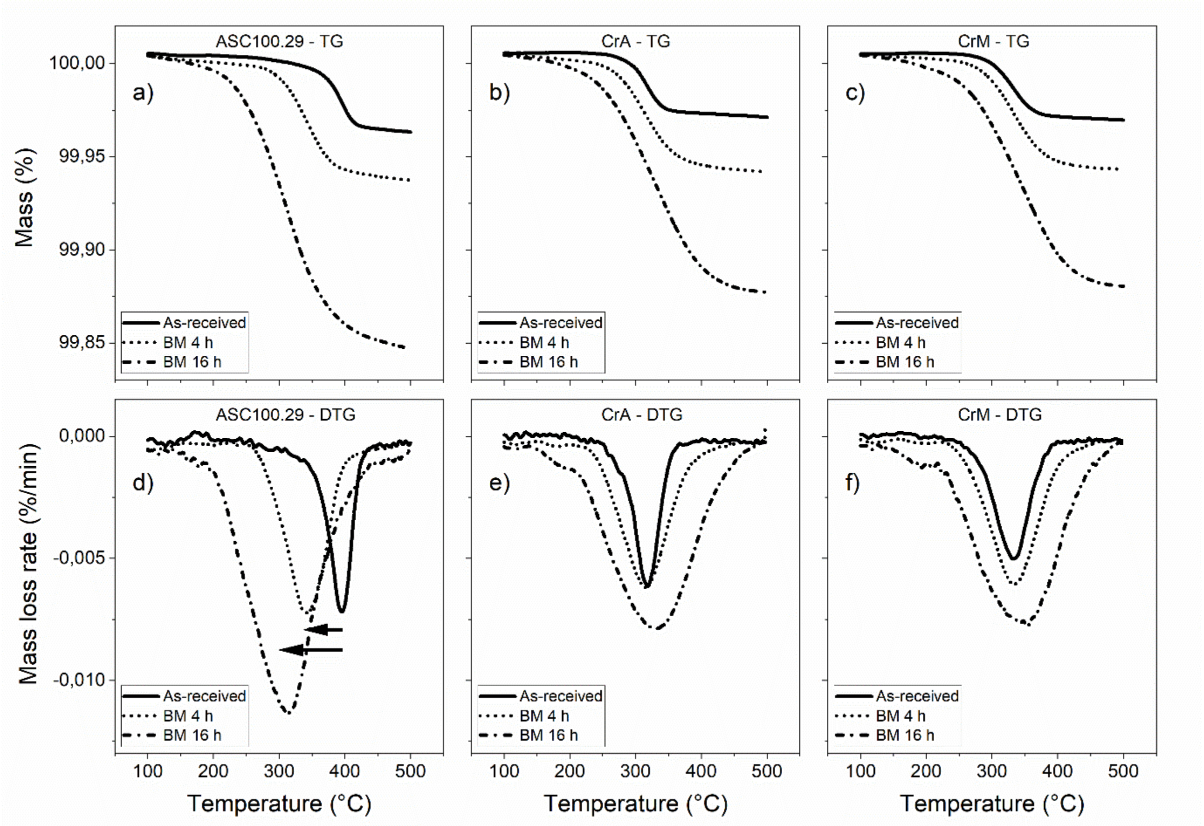

Figure 6.10: Ball milling of ASC100.29, CrA and CrM powder for 4 and 16 h compared with as-received powder. a) and d) TG/DTG of ASC100.29, b) and e) CrA, c) and f) CrM. A reduction rate peak broadening is present along with a distinct shift to lower reduction temperatures in the case of ASC100.29.

broadening of the peaks showing the rate of reduction. For ASC100.29, a distinct shift of the reduction rate maxima to lower temperatures can also be identified which is not present for the pre-alloyed grades, see Figure 6.10d-f. This suggests that the structure and characteristics of the oxide layers are different for water-atomized iron and steel powder, but that the milling may act to normalize the grades, at least in terms of reduction temperatures.

One issue with the ball milled experiments is that the powder is expected to change in several ways: (i) no assessment of the particle size distribution was done, and it is acknowledged that any change to that may affect the magnitude and position of the reduction peaks to some extent as indicated in Figure 6.3 for the fine powder fractions, (ii) new surfaces are created and oxidized so there will a build-up of more surface oxides on the powder, (iii) strains are introduced in the metal matrix simultaneously as changes to the oxide. Due to limitations in separating the contributions from each event, a comparison with the as-received powder will thus be difficult. However, this processing indicates that the initial surface oxide reduction of powder grades is affected by mechanical deformation to some extent, at least in the case of ASC100.29, whereby the milling could be viewed as a type of high-intensity analogy of deformation by compaction. Further details regarding compacted and milled powder can be found in Papers II and VI.

6.4 MASS LOSSES IN THE FERRITE REGION AND AT HIGH TEMPERATURES

Beyond the initial mass loss of the typical thermogravimetric curve seen in Figure 6.2, there is a temperature region of relatively stable mass for the powder samples. When entering this range during heating, the surface iron oxide layer has been completely removed, leaving the powder surface as a clean metal separating the stable particulate oxides that are randomly distributed on the surface. As the solubility of oxygen is low in either of the iron phases [42], any internal oxygen is likely bound as internal oxides in the bulk or at grain boundaries, see for example [63,64] and 6.11b. The removal of internal oxygen can be inferred from the thermogravimetric curves in Figure 6.11a obtained from water-atomized iron powder heated to 900 and 920 °C and held for 1 hour. Here, the strong reducing conditions on the surface and the absence of an oxide layer causes a drive for outwards diffusion of oxygen from internal oxides through the matrix.

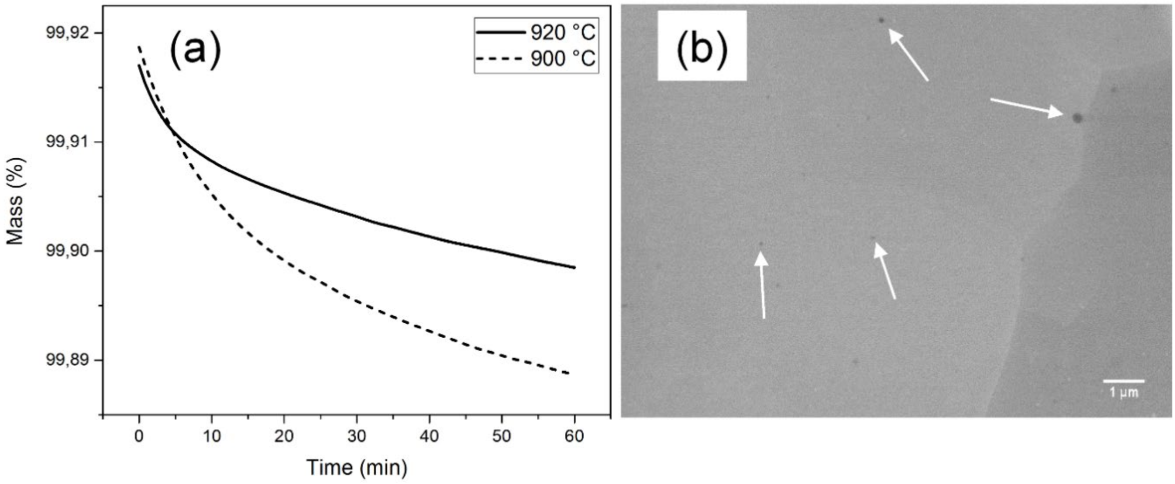

Figure 6.11: a) Mass loss in water-atomized iron powder at 900 and 920 °C in hydrogen indicating the phase-dependence of interstitial diffusion, b) internal oxides in iron powder Fe75. From Paper II.

A clear phase-dependence can be observed, with greater mass loss obtained in the low-temperature ferrite phase with BCC structure. Above the α→γ transformation, iron exhibits the FCC structure with lower substitutional and interstitial diffusivity [95–97,119], thus limiting the removal of internal oxygen. The results indicate that some amounts of internal oxides are present in the powder and can be reduced, as reduction of surface-bound oxides are expected to follow an exponentially increasing reaction rate with increasing temperature, without any limitations from diffusion in iron. However, the surface reactions may significantly affect the reduction curves in Figure 6.11a, but their contribution is expected to diminish rapidly within the first few minutes. A similar reduction behaviour was not observed for the steel powder grades, which are expected to have more stable particulate oxides on the powder surfaces as well as similar internal oxides that are not easily reducible until higher sintering temperatures are reached, see Figure 6.12.

Further mass loss and surface chemical changes during sintering were studied in Paper IV to detail the extent of oxide reduction with increasing temperature. Some results of the analyses can be seen in Figures 6.12-6.13. Immediately after the surface oxide layer reduction at low temperatures, the analysed powder grades show clear metallic iron shoulders in the Fe 2p region (6.13a and 6.13d). As mentioned previously, the reason for the presence of Fe-oxide besides the Fe-metal in the Fe 2p spectrum is the inevitable exposure of the samples to air

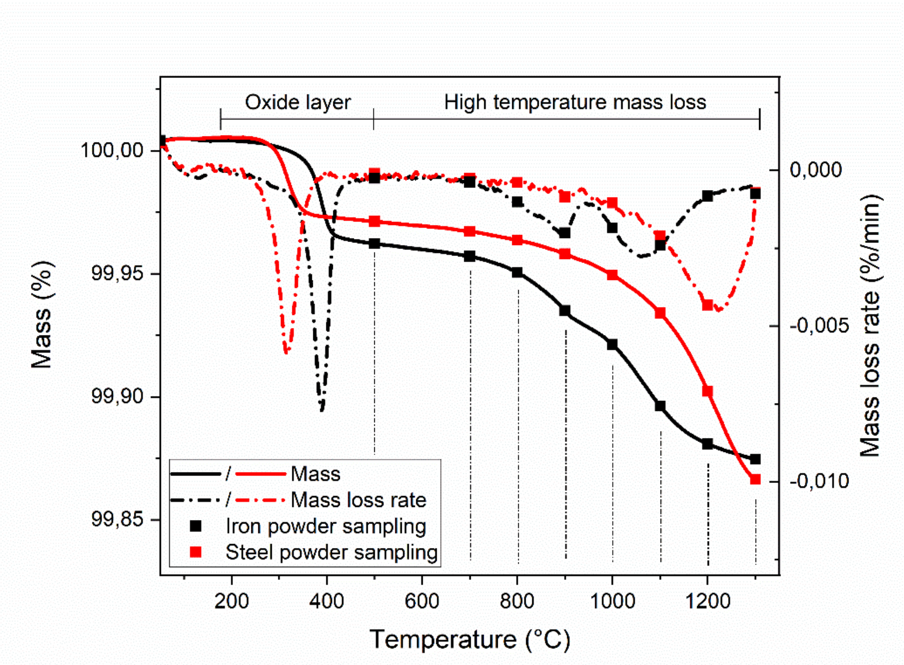

Figure 6.12: Thermogravimetric curves of iron (ASC100.29) and steel (CrA) powder heated to 1300 °C in pure hydrogen. The points represent sampling points for XPS analyses. From Paper IV.

during transfer between the thermogravimetric and XPS analysers. Nevertheless, the presence of other compounds is indicative of the changes that occur during the reduction experiments. For the iron powder, the content of Mn-oxide is shown to be relatively constant over the

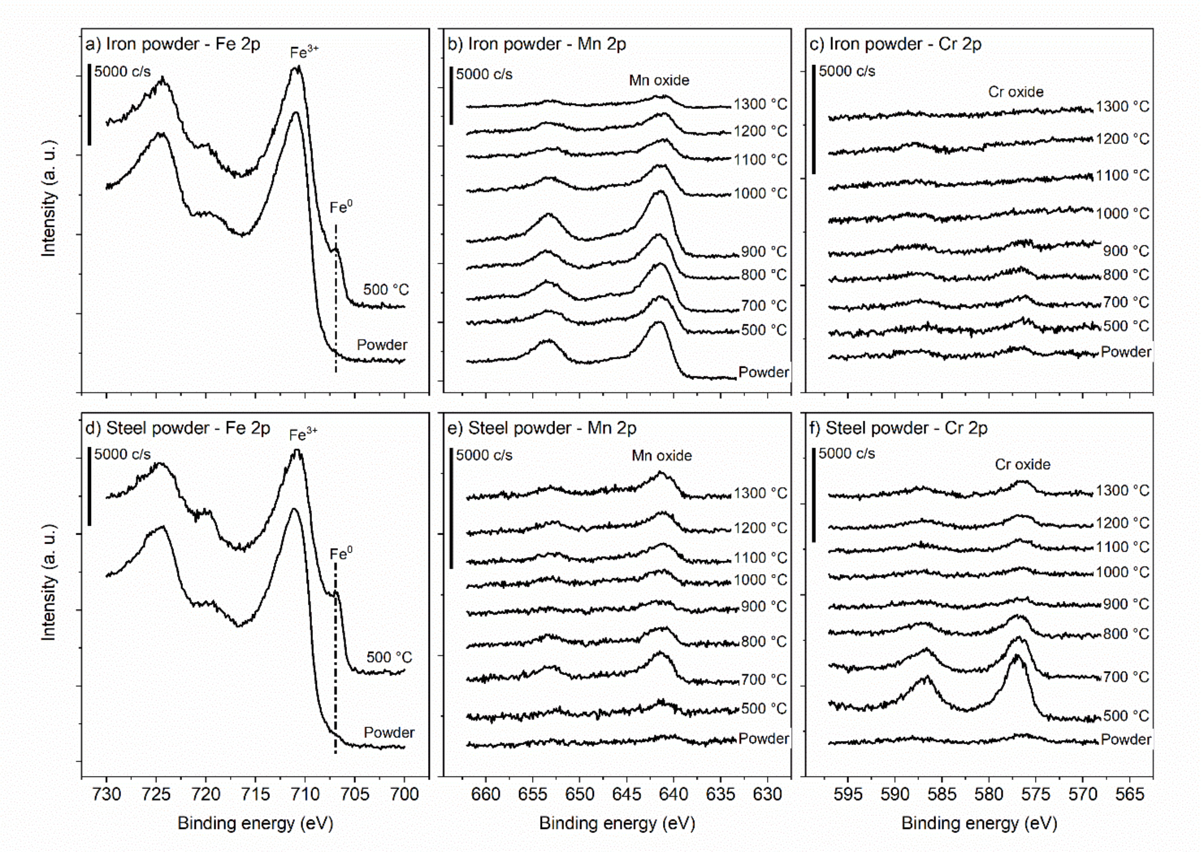

Figure 6.13: XPS analyses of water-atomized iron and steel powder. a) Fe 2p, b) Mn 2p and c) Cr 2p regions of iron powder. d) Fe 2p, e) Mn 2p and f) Cr 2p regions of steel powder. From Paper IV.

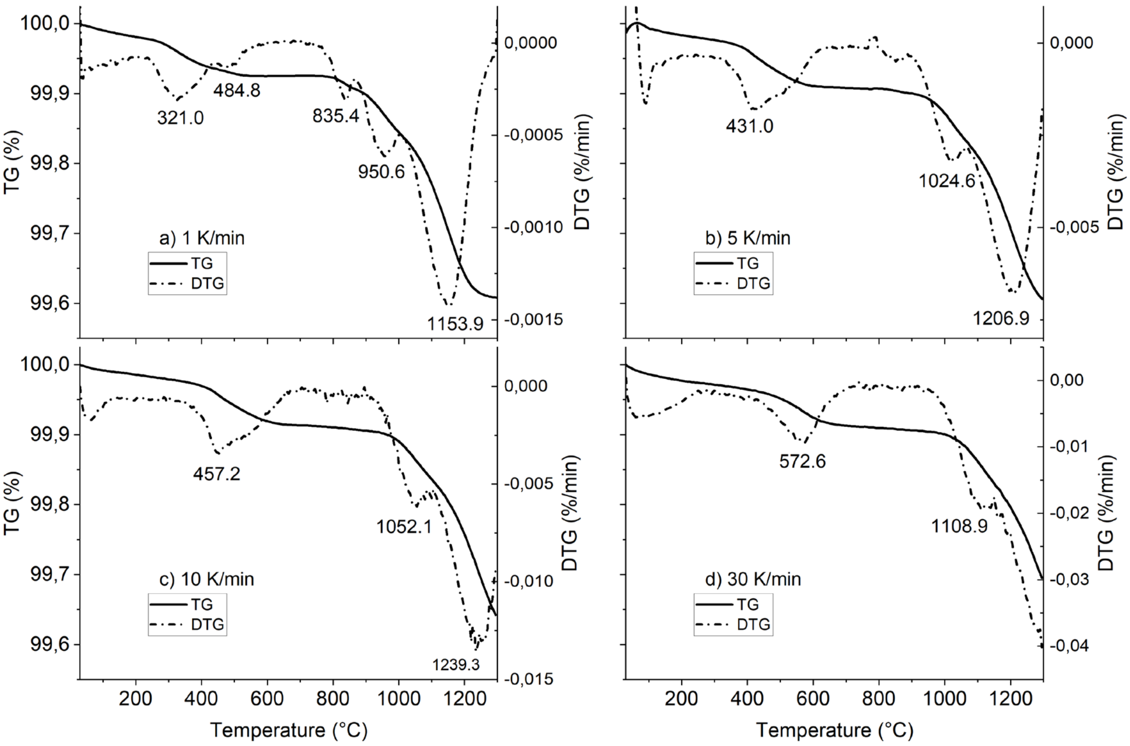

Figure 6.14: CrM + 0.4 wt. % C compacts sintered in Ar-10H_2 at a) 1, b) 5, c) 10 and d) 30 K/min. The graphs show the combined effects of carbon addition, gas dilution and compaction on the reduction curves. At low heating rates, several peaks can be resolved whereas they blur together at higher heating rates. At the standard 10 K/min in c), three main peaks are visible with a significant shift of the oxide layer reduction peak. From paper VII.

reduction event at temperatures below 500 °C, but with a progressive increase up to about 900 °C followed by a decrease at increasing temperatures up to 1300 °C. Consequently, Mn appears to not be involved in the surface oxide layer reduction below 500 °C. For Cr, the Cr-oxide intensity increases after heating to 500 °C, thereby indicating the involvement of Cr in the events connected to the reduction of the Fe-oxide layer on the steel powder, cf. Figures 6.6 and 6.7.

At elevated temperatures, the mass losses recorded by thermogravimetry correspond to both reduction and removal of internal oxides as well as particulate oxides on the powder particle surfaces for all powder grades. Oxides that are thermodynamically more stable than iron oxides, such as those based on Cr, Mn and Si, require elevated temperatures in order to be reduced. Consequently, the composition of the powder grades is reflected in the thermogravimetric curves as indicated in Figure 6.12 where the main reduction peak in austenite for ASC100.29 is located at about 1050 °C as compared to about 1200 °C for CrA.

A more applied setting with industrial conditions was analysed in Paper VII [120] for CrM, see Figure 6.14. Both compaction of the powder, added carbon and a dilution of the processing gas affects the overall reduction curves compared to Figure 6.2. The dilution delays reduction which is then further accentuated by the restriction due to compaction. At higher temperatures, carbothermal reduction mechanisms become active and aid hydrogen in reducing the remaining oxide species.

6.5 KINETIC ANALYSES OF OXIDE REDUCTION

Kinetic analyses based on thermogravimetric measurements were done to further investigate the reduction behaviour of oxides present on water-atomized iron and steel powder. Both the low-temperature process of surface oxide layer reduction as well as the mass losses above the α/γ transformation were analysed, see results in Papers II and V. Special emphasis was put on the reduction of the surface oxide layer and how this process is influence by e.g. powder composition and initial condition (Papers II and V) as well as compaction (Paper II).

The kinetic analyses were done utilizing both the Kissinger [77] and the isoconversional Kissinger-Akahira-Sunose [77,90,94] methods. The methodology and analysis steps are detailed in Papers II, V and in chapter 5 covering the experimental details. Both methods have been successfully applied for reduction of various metal oxides [86,87], including iron oxides and milled iron ores [56,57,88,121] as well as binder systems in metal injection moulding [83,84]. It is shown in this thesis that the methods can also be applied for studying reduction of the thin oxide layers that exist on ferrous powder particles, and in extension be utilized as an important tool for studies of chemical reactions that are of interest to the PM industry. The analysis of the reduction processes based on TGA is shown to be sensitive to a variety of material and processing conditions such as alloying elements and initial powder state, powder particle size/size distribution and compaction pressure/deformation. The subsequent kinetic analysis can therefore be used as a tool to further assess the impact that these factors have on oxide reduction, and the implications for sintering.

It should be emphasized that the kinetic results are highly dependent on the characteristics of the starting material as well as the experimental setup and the conditions that are used for the experiments. Because of this, a large spread of reported activation energies can be found in literature despite describing the same reduction steps [48–50]. Nevertheless, the experimental setup and conditions are kept constant for the results presented in this thesis, thus allowing for isolation and comparison of the inherent characteristics of the investigated materials.

6.5.1 Kissinger analysis

Kissinger plots can be seen in Figure 6.15 for surface oxide reduction of ASC100.29, CrA and CrM along with their reduced and re-oxidized surface conditions, as well as the reduction step $Fe_2O_3 \rightarrow Fe_3O_4$ of pure hematite for reference. The results show the activation energies of reduction as the slope of the curves, with the position of the data points indicating at which temperature the peak rate of reduction is located. The activation energies of the $Fe_2O_3 \rightarrow Fe_3O_4$ step and reduction of the oxide layer of ASC100.29 are similar, while the values are significantly lower for the reduction of the oxide layer for all other powder grades and conditions. This indicates a strong effect on reduction from what is believed to be the alloying elements and the initial, as-received, condition of the powder grades. Multiple reduction steps are expected for the overall reaction $Fe_2O_3 \rightarrow Fe$ but cannot be distinguished in the case of reduction of oxide layers on powder grades. After reduction and re-oxidation, the activation energies of the surface oxide reduction in the case of ASC100.29, CrA and CrM essentially converge to around 70 kJ/mol, meaning that the reactions are expected to proceed in a similar fashion under these dynamic conditions. As mentioned previously, an underestimation of the activation energy can be expected in the case of a N_2/H_2 mixture due to the worsened heat transfer and lower reducing activity of the atmosphere. Some results of the low-temperature reduction experiments are summarized in Table 6.1. Further information can be found in Paper

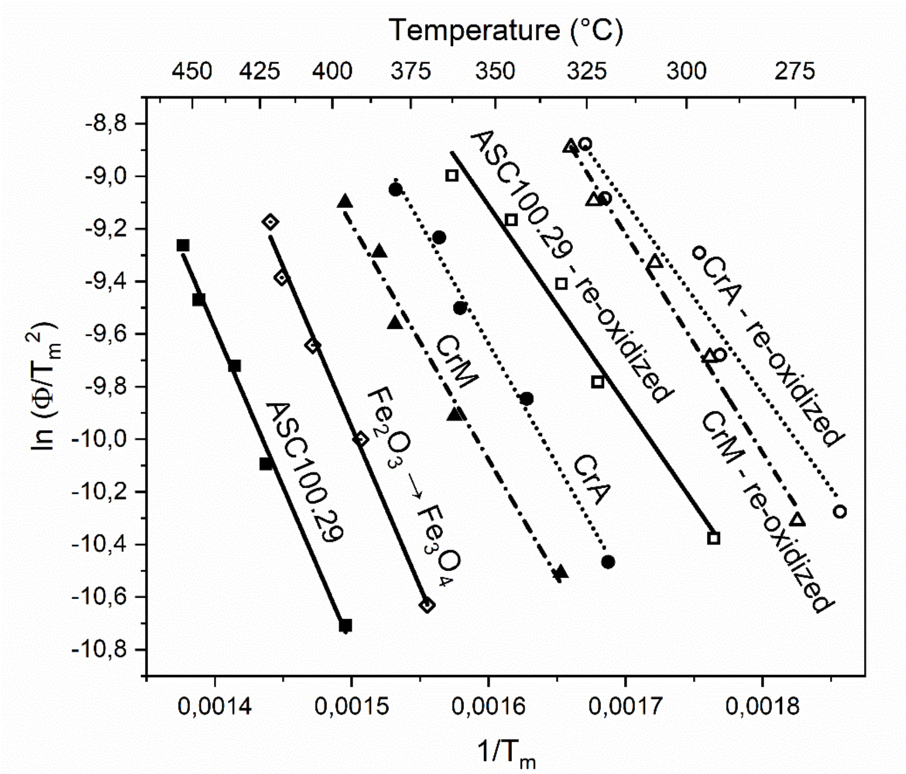

Figure 6.15: Kissinger plots for reduction of the surface oxide layer of ASC100.29, CrA and CrM and their re-oxidized counterparts. The reduction step $Fe_2O_3 \rightarrow Fe_3O_4$ of a pure hematite oxide powder is included for reference. From Paper V.

II for fine powder fractions, Paper V, and Paper VII for an applied setting with compaction, added graphite and gas dilution.

Table 6.1: Calculated apparent E_a from Kissinger plots

Powder grade and conditions	**Activation energy (kJ/mol)**	**R^2**	**Temperature range**
$Fe_2O_3 \rightarrow Fe_3O_4$	101 ± 5	0.99	370-421 °C
ASC100.29	100 ± 4	0.99	396-453 °C
Re-oxidized	63 ± 6	0.98	294-363 °C
CrA	75 ± 4	0.99	317-380 °C
Re-oxidized	60 ± 8	0.95	266-326 °C
CrM	74 ± 6	0.98	335-396 °C
Re-oxidized	69 ± 4	0.99	275-329 °C

The values presented in Table 6.1 are in reasonable agreement with previous literature on reduction of iron oxide, see for example [48,49,88,122,123]. However, as indicated earlier, the results also reflect the experimental setup and initial state of the samples [48–50].

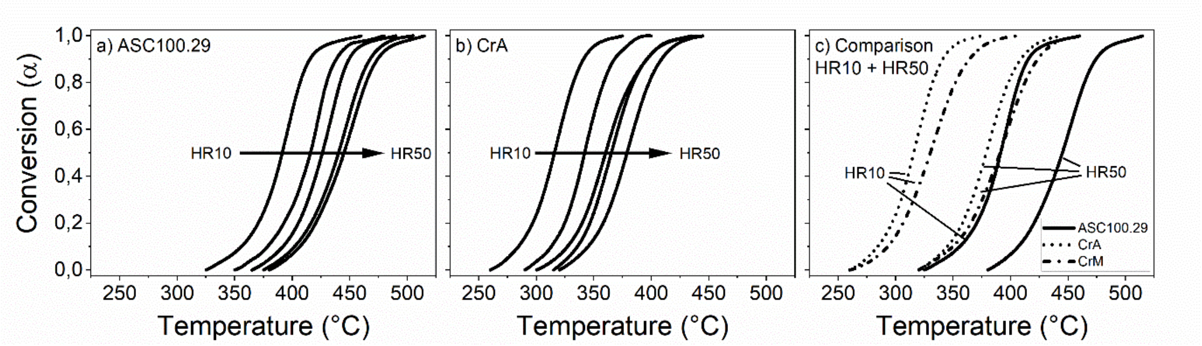

Figure 6.16: Conversion versus temperature for a) ASC100.29 and b) CrA. c) Comparison between three powder grades at HR10 and HR50. From Paper V.

6.5.2 Isoconversional methods

The isoconversional kinetic method was used to minimize the assumptions made regarding how the reduction proceeds and see if there is a potential E_α vs. α dependence. This behaviour cannot be captured by the Kissinger formulation as it only gives a single activation energy, regardless of the real complexity of the reduction process [90]. Isoconversional analyses were performed for both the surface oxide layer reduction (Papers II and V) as well as for the high temperature mass loss events (Paper II).

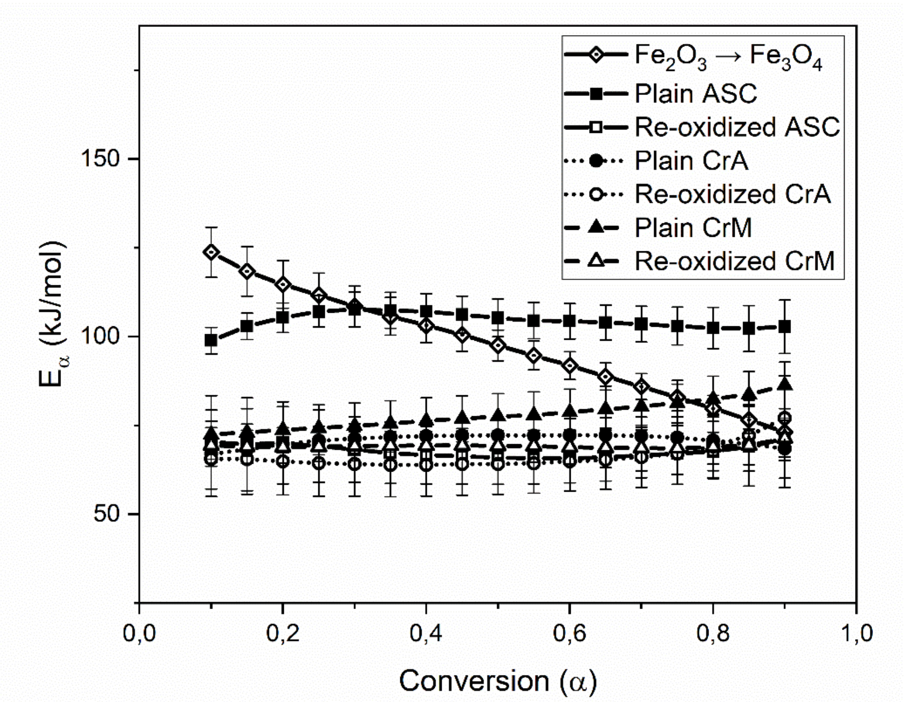

Figure 6.17: Isoconversional analysis of surface oxide layer reduction for ASC100.29, CrA, CrM and their re-oxidized counterparts. The reduction step $Fe_2O_3 \rightarrow Fe_3O_4$ of a pure hematite oxide powder is included for reference. From Paper V.

Figure 6.16 shows an example of dynamic thermogravimetric measurements of ASC100.29, CrA and CrM over the range of the surface oxide layer reduction. The plots are computed to show the extent of conversion according to Equation 5.1, with the curves shifted to higher temperatures at higher heating rates.

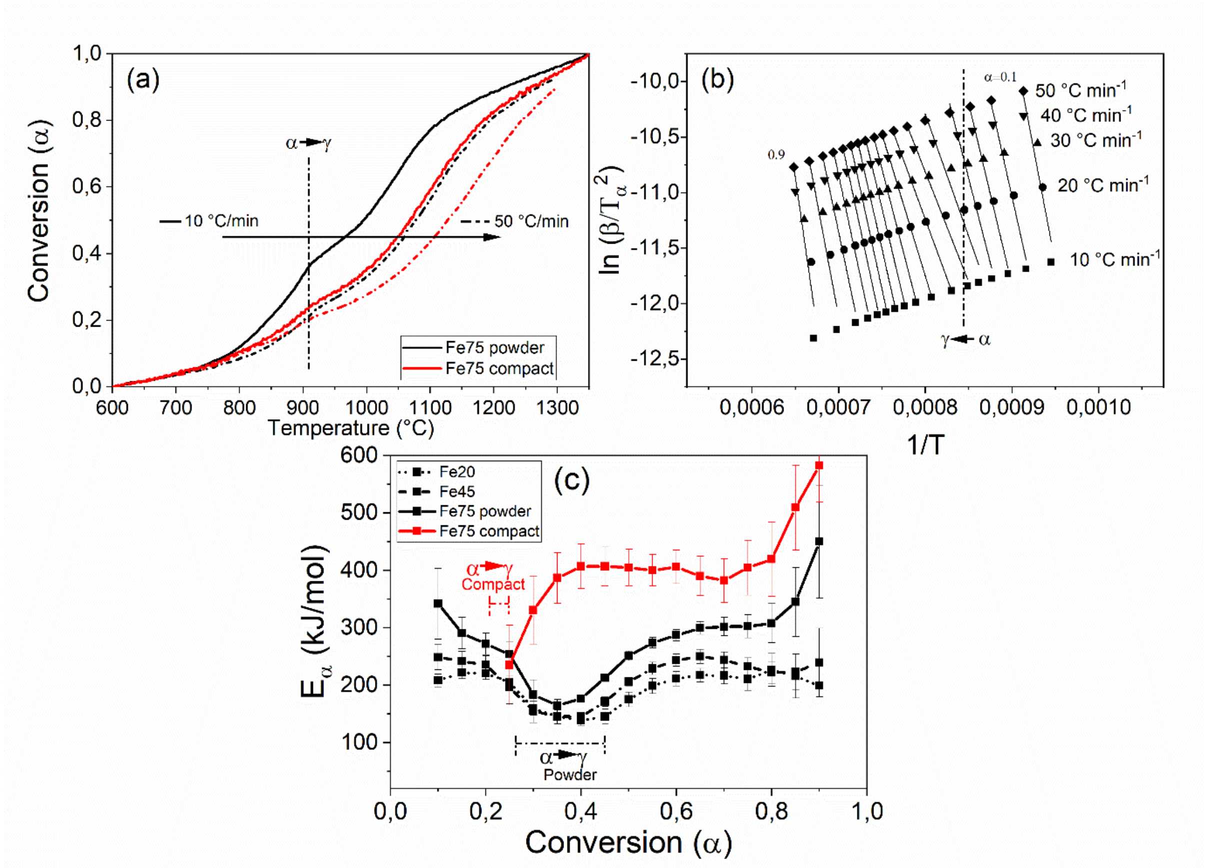

Figure 6.18: Isoconversional kinetic analysis of high temperature reduction in water-atomized iron powder and compacts. a) Conversion vs. temperature for HR10 and HR50, b) linear fitting at different conversions of Fe75 powder, c) E_α vs. conversion for powder and compacts. From Paper II.

Like the Kissinger analysis, the isoconversional analyses yields the activation energies of the studied reduction reactions, see Figure 6.17. The difference is that the analyses reveal a complex reduction behaviour with a conversion dependence of the $Fe_2O_3 \rightarrow Fe_3O_4$ reduction step of the pure hematite powder, which is otherwise not captured by the Kissinger method which gives only a single activation energy. The explanation for this is that the reduction likely proceeds via an autocatalytic nucleation and growth mechanism, in which the second part has a lower activation energy [57,90]. The powder grades, i.e. ASC100.29, CrA and CrM, show a relatively stable activation energy with no clear E_α vs. α dependence. The reduction of the surface oxide layers thus appears to proceed as an apparent single step reduction and can be associated with a single apparent activation energy although the reduction is likely more complex. The as-received ASC100.29 powder is shown to have a significantly higher activation energy for the reduction of its oxide layer than the CrA and CrM steel powder grades. After initial reduction and re-oxidation at which point the powder can be thought of as normalized, no differences can be observed in terms of activation energy values although the reduction temperatures still differ between the powder grades. Based on these analyses, it is believed that the initial state of the powder and the alloying elements are jointly responsible for the differences observed between the powder grades. In the case of Cr pre-alloyed grades, Cr is expected to contribute to the changes in powder surface chemistry while for ASC100.29, Cr is less important, and Mn as a trace element may some role. As explained previously, due to the detection limits of XPS and AES, it is unclear whether the surface oxide layer contains cations of elements other than iron. However, while the presence of foreign oxides and their

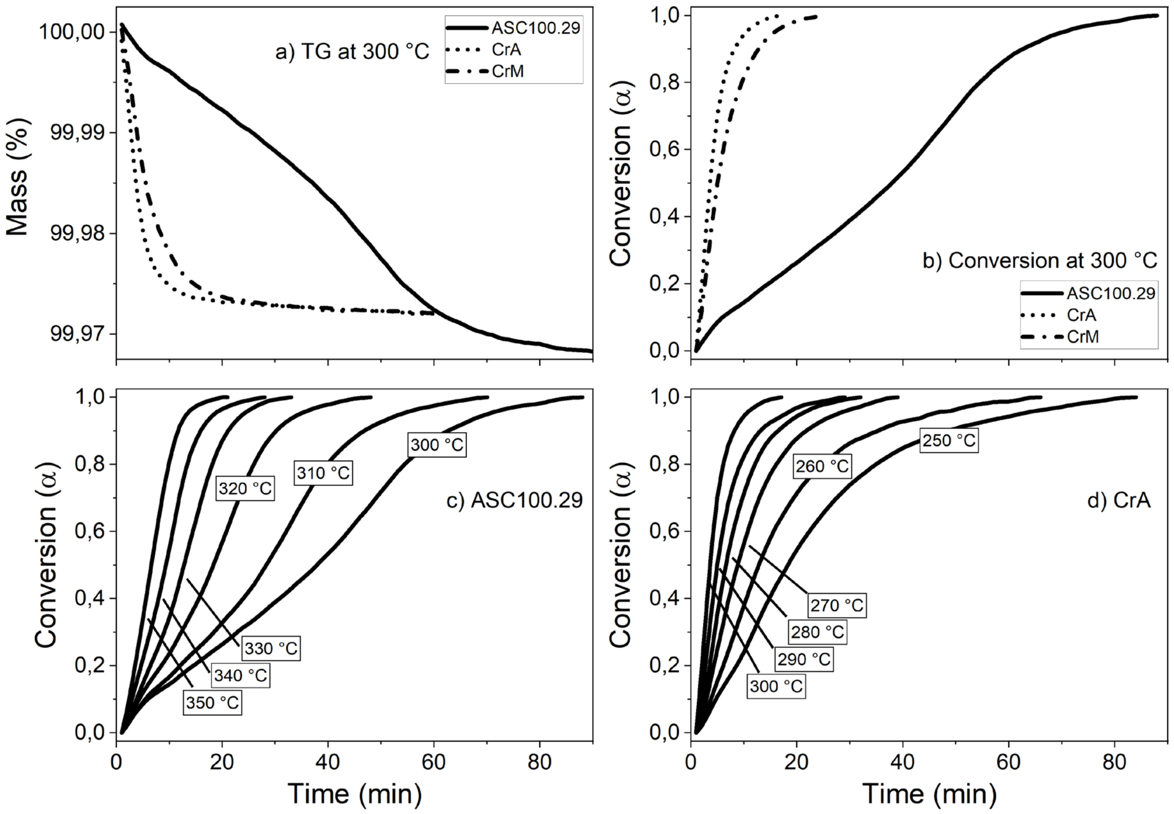

Figure 6.19: Isothermal reduction curves. a) TG at 300 °C, b) conversion at 300 °C. Detailed isothermal reduction curves of c) ASC100.29 and d) CrA at different temperatures. From Paper V.

possible involvement in the reduction of the surface oxide layer cannot be explicitly proven, the thermogravimetric and kinetic analyses, c.f. Figures 6.4, 6.6, 6.7, 6.16 and 6.17 infer that at least chromium is likely influencing the results to some extent.

The high temperature reduction processes are more complicated, as they reflect the compounded effects several factors. First, the removal of internal oxides through diffusion of atomic oxygen in the metal matrix and the phase dependence of that process (cf. Figure 6.11). Second, the effect of reduction of surface oxides with varying chemical composition. Finally, how these processes are in turn affected by temperature and the mass transport restrictions that occur during sintering. The isoconversional plots in Figure 6.18 captures both the shift of main reduction peaks in the range 1000-1200 °C in addition to the progressive removal of oxygen during the heating stage where the metal powder initially exists as ferrite prior to the transformation to austenite.

6.5.3 Kinetic predictions

Predictions based on kinetic analyses are probably the most concrete use of the calculated apparent activation energies [90], apart from using them to distinguish between the nature of chemical reactions. Reaction time predictions have for example been used to estimate the progress of reduction of hematite [57] or other iron oxides in general [48,50]. In this thesis, some predictions based on the derived apparent activation energies from Papers II and V are used for estimating the time to reach complete conversion of reduction of the surface oxide layer on water-atomized iron and steel powder grades. The kinetic analyses presented above, based on the dynamic measurements presented in Papers II and V, with an example in Figure 6.16, clearly show a difference between the water-atomized iron and steel powder grades. The difference is further highlighted by isothermal measurements showing the time to reach full conversion of the oxide layer reduction at a fixed temperature, see Figure 6.19. At an isothermal temperature of 300 °C (6.19b), the time required to complete the reduction is about 15-25 minutes for the steel powder grades, whereas the iron powder requires up to 90 minutes. In Figure 6.19c-d it can also be seen that the conversion curves have a different appearance with ASC100.29 exhibiting a sigmoidal reduction behaviour if the temperature is sufficiently low whereas CrA instead shows a decelerating curve. Further details can be found in Paper V.

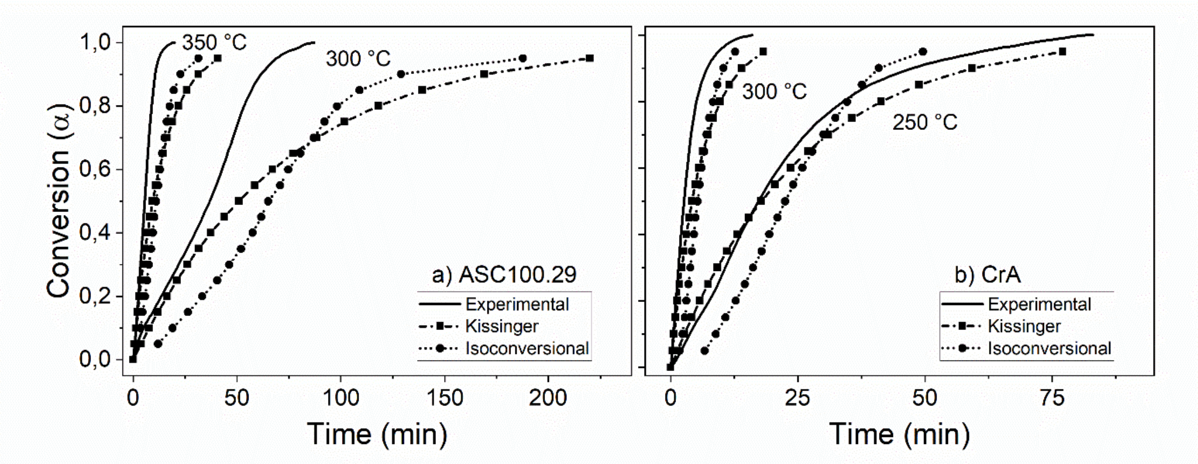

Figure 6.20: Kinetic predictions of a) ASC100.29 and b) CrA at two different temperatures using results from the Kissinger and isoconversional analyses.

For the kinetic predictions to be meaningful, they need to capture the differences between the powder grades that are observed in Figures 6.19. The results from the predictions are shown in Figure 6.20a-b for ASC100.29 and CrA, respectively, using the activation energies derived earlier as input into Equations 4.10 and 4.11 and compared to isothermal conversion curves presented in Figure 6.19. A reasonable agreement between the calculated predictions and the experimental results is found for CrA at both 250 and 300 °C, and at 350 °C for ASC100.29. However, the predictions for low temperature (300 °C) reduction of the oxide layer on ASC100.29 is relatively poor, with a large overestimation of the time by which the reduction reaches full conversion. The single step prediction can only estimate the time for conversion up to about $\alpha = 0.4$, above which the prediction deviates from the experimental curve. On the other hand, the isoconversional prediction captures the reduction curve shape with higher accuracy, but with a large shift in position of the curve. One limitation with the analysis, and likely a reason why the reduction behaviour of ASC100.29 is more difficult to model, is that the reduction of the surface oxide layer on the powder appears to transition from a decelerating curve at high temperatures to a sigmoidal conversion curve at lower temperatures. This transition is believed to reflect a reduction behaviour that is more complex than anticipated if the surface oxide layer would have been completely homogeneous. Consequently, the conversion rate reaches a maximum at some conversion other than zero, see Figure 6.21. For ASC100.29, this occurs about halfway which could be indicative of an autocatalytic reduction behaviour which is not seen for CrA. Additionally, the predictions become less accurate in temperature regions far away from where the activation energies were obtained [90].

Based on the thermal and surface analyses presented above, the reduction behaviour of the iron and steel powder grades are consequently believed to be fundamentally different from each other, with surface oxide layer chemistries reflecting the differences in overall powder chemistry between ASC100.29 and Cr pre-alloyed grades.

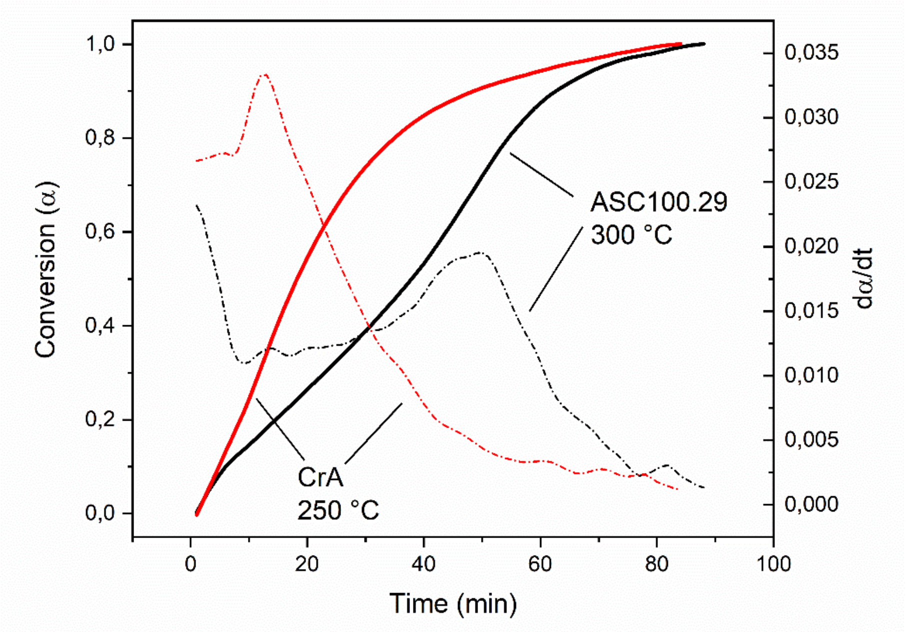

Figure 6.21: Isothermal conversion of oxide layers on CrA and ASC100.29 at 250 and 300 °C, respectively. The first derivative curves are added which indicate the decelerating and sigmoidal behavior of the oxide reduction.

6.6 SINTERING BEHAVIOUR OF WATER-ATOMIZED IRON AND STEEL POWDER

Uniaxially compacted water-atomized iron and steel powder grades are typically pressed to high green densities prior to sintering to ensure high final sinter densities as well as to mitigate excessive shrinkage. The pressing operation introduces particle rearrangement as well as plastic deformation of the particles on a microstructural level. The resulting green compact also has a complex anisotropic character that originates from the pressing, in which regions perpendicular to the compaction direction are more heavily deformed than regions parallel to the compaction direction [40,60]. Besides the general effects of grain boundary and volume diffusion, contribution to sintering shrinkage is believed to come from geometrical and structural activity, originating from the increased particle proximity and coordination number, and dislocation-enabled pipe diffusion, respectively.

6.6.1 Green state characterization

As outlined in Paper III, the deformation from compaction is likely to be localized to mainly interparticle contact regions or smaller sections or protrusions of the highly irregular metal powder particles while the bulk of larger particles remaining relatively undeformed. An example EBSD micrograph is seen in Figure 6.22a-b showing undeformed and compacted powder. The presence of low-angle grain boundaries can be considered as arrays of dislocations and is indicative of a deformed microstructure [71,72].

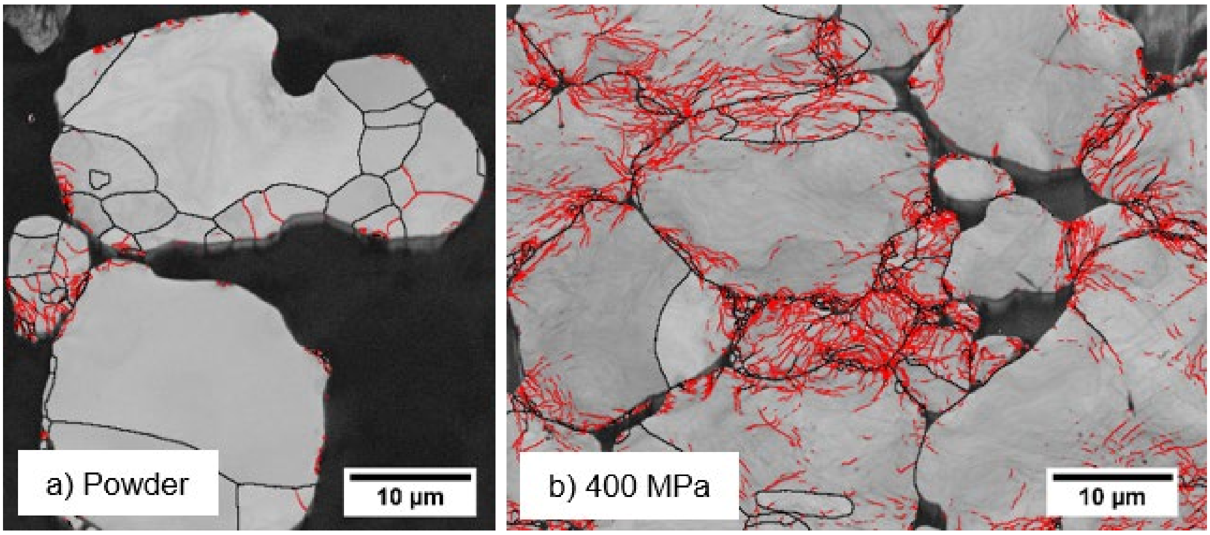

Figure 6.22: EBSD maps of a) as-received and b) compacted powder with low- and high-angle grain boundaries depicted in red and black, respectively. From Paper III.

Sintering of the green compacts was done using a variety of model sintering cycles but can be classified as being confined to low and high sintering temperatures. Low temperatures are here defined as being below the typical 1120 °C industrial sintering temperature.

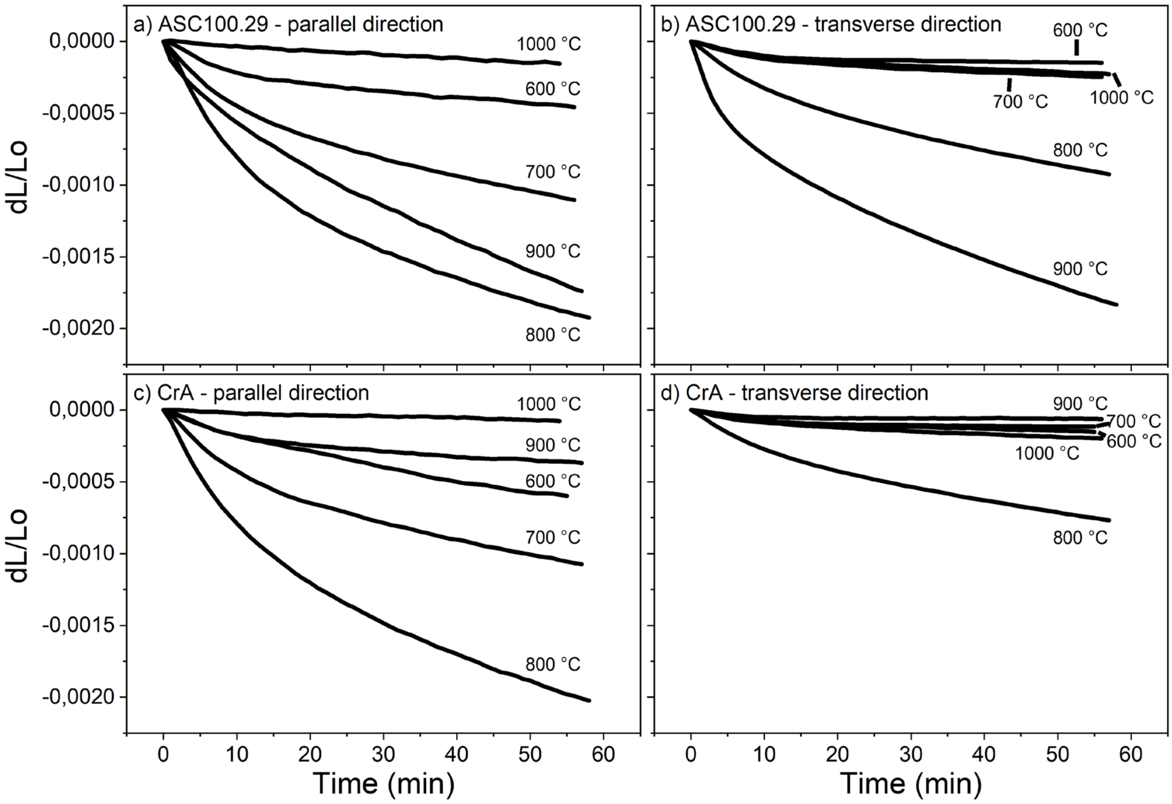

Figure 6.23: Isothermal shrinkage at low temperatures for ASC100.29 and CrA in different directions. a) and b) ASC100.29 in parallel and transverse directions, c) and d) CrA in parallel and transverse directions. From Paper VI.

6.6.2 Low temperature sintering

Low temperature sintering trials were conducted to capture the sintering behaviour taking place during the heating stage of a typical industrial sintering cycle, and especially the sintering shrinkages that take place in the high-diffusivity ferrite phase of the iron/steel matrix.

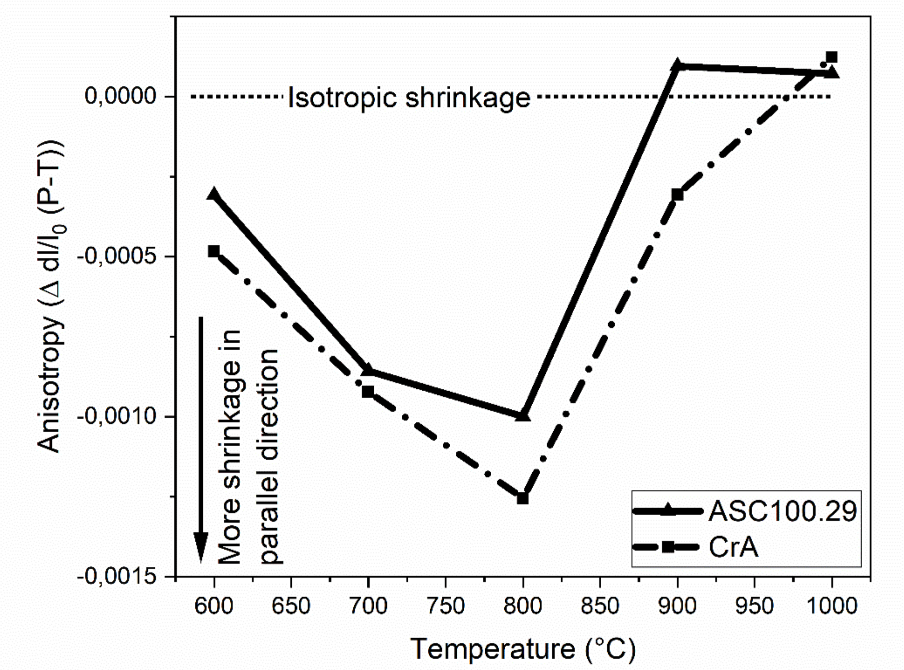

Figure 6.24: Shrinkage anisotropy in the range 600-1000 °C for ASC100.29 and CrA. From Paper VI.

In Papers III and VI it is shown that significant shrinkage can occur even at these low temperatures, see Figure 6.23. The differences between shrinkages in the parallel and transverse directions also highlight the significant anisotropy that exists in the green compacts after uniaxial pressing, see Figure 6.24. The anisotropy in sintering is initiated already at 600 °C and then increases until it reaches a maximum somewhere before the α/γ transformation temperature. The magnitude of the shrinkages is also strongly affected by the compaction pressure as shown in Paper III and is believed to additionally be further influenced by structural activation as explored in Paper VI.

While hydrogen facilitates low temperature reduction as indicated earlier, a diluted hydrogen atmosphere delays reduction, cf. Figure 6.8. In extension, the deteriorated atmosphere influences sintering as shown in Figure 6.25 for ASC100.29 and CrA sintered in H_2 and N_2/H_2 at 800 °C for 1 hour. The combination of a delayed reduction caused by dilution and restriction of mass transport caused by compaction means that significant obstruction to sintering remains. This shows the link between the chemical changes that takes place as the powder interacts with the sintering atmosphere and the sintering shrinkages that are in turn affected by that interaction.

Low-temperature sintering cycles can provide information about the role of early stage processes during sintering such as the initial reduction of the surface oxide layer as well as the high mass transport in ferrite before the α/γ transformation that influence early sinter neck formation and anisotropy. These cycles thus form a basis for further understanding the processes that occur at higher temperatures that are used in industrial sintering practice.

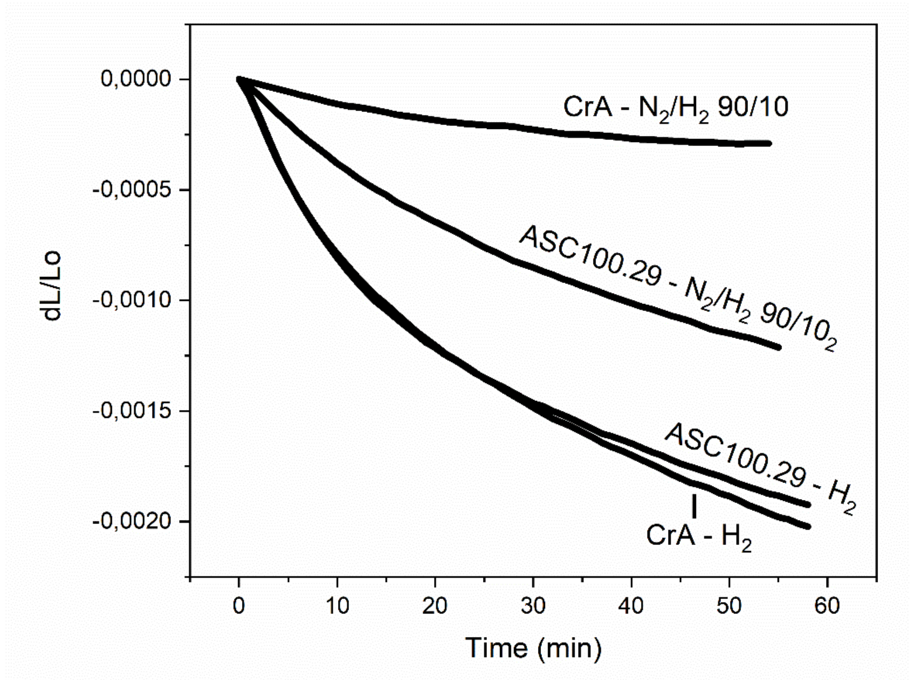

Figure 6.25: Influence of processing atmosphere on sintering shrinkage in ASC100.29 and CrA at 800 °C. From Paper VI.

6.6.3 High temperature sintering

Sintering using cycles that more closely resemble industrial practise was conducted at temperatures in the range 1120-1250 °C which are common, and at 1350 °C which can be considered very high for industrial sintering. Pure hydrogen atmospheres were used for samples

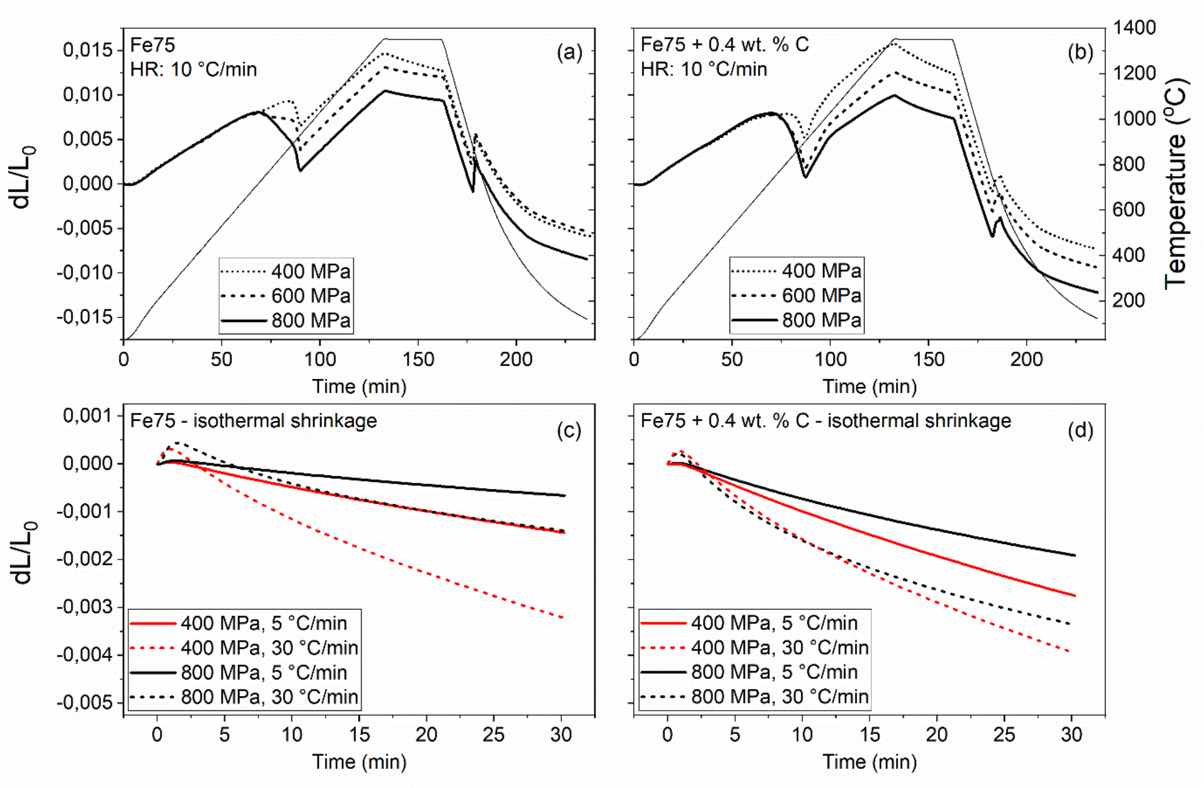

Figure 6.26: Sintering cycles of Fe75 and Fe75+C samples under different conditions. a-b) complete sintering cycles, c-d) isothermal shrinkages. From Paper III.

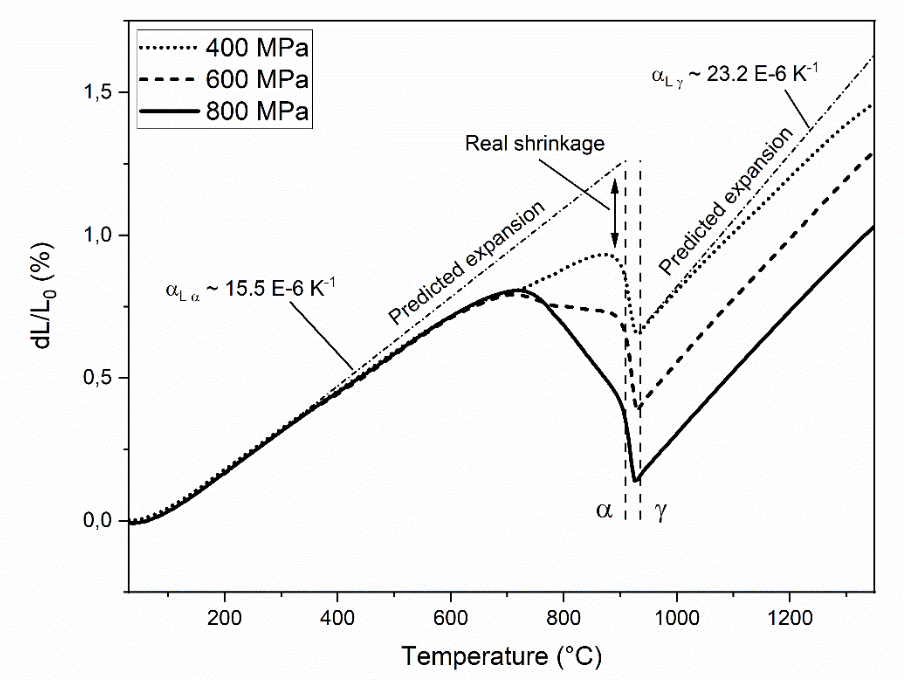

Figure 6.27: Methodology for determining the sintering shrinkage in each region – ferrite, austenite and isothermal. From Paper III.

with and without added graphite. It should be noted that this choice of atmosphere is not according to industrial practice but is deemed to be of importance in line with the oxide reduction studies presented above. Results from sintering at 1350 °C can be seen in Figure 6.26. Because of the significant influence of compaction pressure as well as increased diffusivity in the ferrite region, as explained previously, the high temperature sintering behaviour must be considered based on this. To quantify the extent of shrinkage during the heating stage and at the isothermal holding temperature, cylindrical samples were sintered repeatedly to provide a baseline for thermal expansion. The real shrinkage could then be extracted from the difference between the values of the calibration cylinder and the sintering,

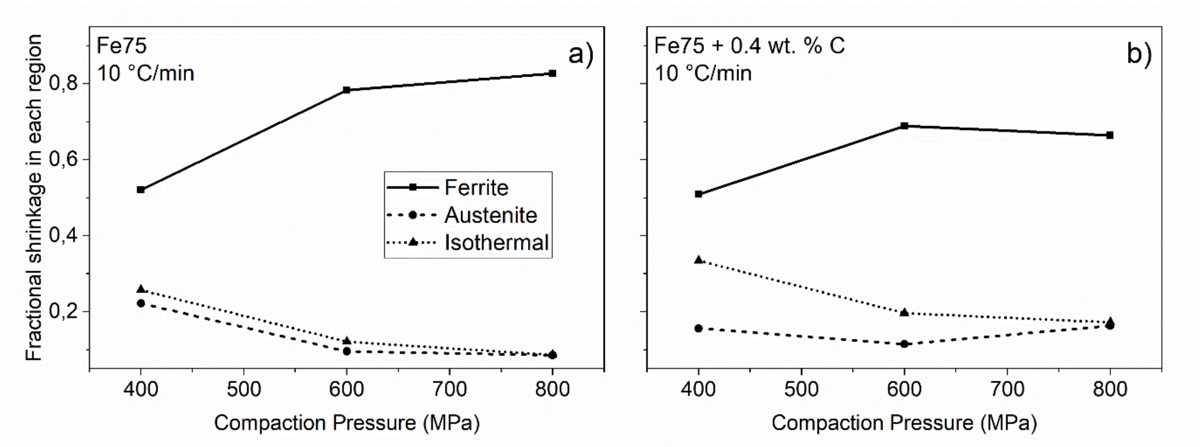

Figure 6.28: Fractional shrinkage in each region – ferrite, austenite and isothermal – versus compaction pressure for a) Fe75 and b) Fe75+C samples. From paper III.

see Figure 6.27. The results show that the shrinkage that occurs in ferrite can account for up to 80 % of the total shrinkage of the material, see Figure 6.28, even if a high sintering temperature of 1350 °C is used. With a lower sintering temperature, less shrinkage will take place in austenite during heating as well as during the isothermal hold, thus making the ferrite shrinkage even more dominant. See Papers III and VI for more details regarding the sintering behaviour.

6.7 MODEL FOR OXIDE REDUCTION AND OXYGEN REMOVAL IN FERROUS POWDER

Previous work has crystallized into models describing the trajectory of oxide reduction, oxygen transfer and finally the oxygen removal in water-atomized iron and low-alloyed steel powder, see for example [8,12,13]. The models provide both a generalized description as well as an applied setting involving hot isostatic pressing. With a basis in the literature, and with support from the current investigation presented in this thesis and the appended papers, an updated model is proposed. The model is schematically shown in Figure 6.29, with special emphasis on the reduction of the surface oxide layer.

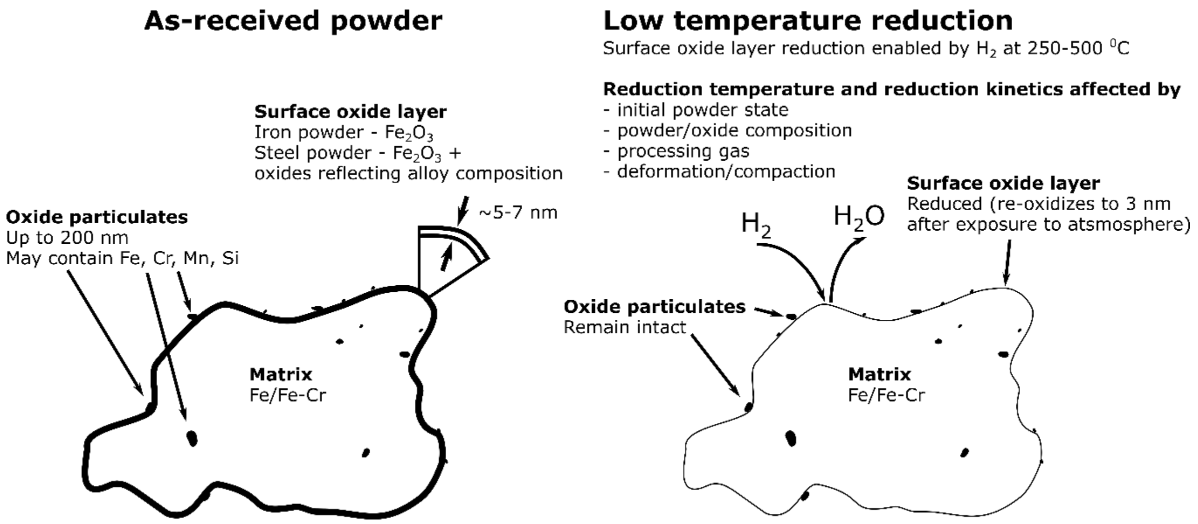

Figure 6.29: Schematic of surface oxide layer reduction in PM steels, and how it is affected by various material and processing parameters.

The oxide layers on water-atomized iron and chromium pre-alloyed grades are different and reflect the powder composition as well as the prior atomization, annealing and handling. The added chromium lowers the reduction temperature and affects the kinetics of reduction compared to iron powder which indicates that the oxide layers are fundamentally different. After the initial surface oxide layer is reduced for pre-alloyed grades, chromium oxide nuclei are likely distributed on the powder particle surfaces where they can subsequently grow and possibly interfere with sinter neck development. Additionally, the surface oxide layer reduction is also significantly influenced by the processing gas where diluted hydrogen shifts the reduction rate maxima to much higher temperatures compared to pure hydrogen, thus risking possible interference with the subsequent sintering. The reduction is further influenced by powder deformation and compaction making the overall oxide reduction event dependent on several material and processing parameters.

Chapter 7

CONCLUSIONS

The sintering of iron and low-alloyed steel powder grades is a complex process. In summary, the outcome can be said to be influenced by parameters connected to the powder grade itself, such as the initial surface chemistry. In addition, sintering is also affected by the experimental parameters which dictate how the powder behaves at elevated temperatures. The combination of surface- and thermoanalytical methods has proven to be an invaluable tool for investigating the changes that occur during the sintering process.

The main conclusions of this doctoral thesis are summarized in the following two sections reflecting the main areas of study: thermogravimetric and kinetic analyses, and sintering by dilatometry.

Thermogravimetric and kinetic analyses

Thermogravimetric analyses simulating the heating stage of sintering revealed three distinct temperature regions of mass loss in water-atomized iron and low-alloyed steel powder; (i) reduction of the surface oxide layer in the range 250-500 °C, (ii) mass loss in ferrite, and (iii) mass loss at high temperatures.

The surface oxide layer

- Thermogravimetric analysis of an Fe_2O_3 (hematite) powder showed the reduction properties of an ideal oxide in hydrogen atmospheres. A three-step reduction sequence, $Fe_2O_3 \rightarrow Fe_3O_4 \rightarrow FeO \rightarrow Fe$, was identified using high heating rates.
- The surface oxide layers covering metal powder particles are approximately 5-7 nm thick and covers the major fraction of the powder surface.
- Fine particle sizes showed a lower surface oxide layer reduction temperature than coarser sizes which is believed to be linked to the increase in surface area.
- The oxide layer is predominantly an iron-based oxide for the analysed water-atomized iron and steel powder grades but is believed to reflect the alloying composition meaning that the Cr pre-alloyed grades are expected to have an oxide layer with small amounts of Cr. These powder grades then show a lower reduction temperature compared to iron powder and Fe_2O_3.
- Diluted hydrogen in a N_2/H_2 processing gas alters the H_2/H_2O ratio and deteriorates the reducing conditions, thereby causing a delay in the reduction of oxides. Hydrogen is thereby shown to be crucial for low-temperature reduction of the iron-rich surface oxide layer.
- Reduction followed by re-oxidation effectively normalizes the powder grades, revealing the native oxide layers forming on the powder without interference from prior

atomization, annealing and handling. The reduction behaviour of these layers therefore reflects the inherent differences between oxides formed on iron and steel powder.

- A change in reactivity by deformation is indicated by compacted and ball milled iron powder where the reduction rate maxima are lowered and broadened.

Internal oxides and high temperature reduction

- Internal oxides are reduced by the driving force for outwards oxygen diffusion created by reducing conditions at the powder surface. This reduction is coupled with oxygen mobility, with increased magnitude in the ferrite region.
- Reduction at high temperatures is influenced by the powder composition as well as the increasingly restricted transport due to sinter neck development.

Kinetic analyses

- An apparent single reduction step was identified for reduction of oxide layers on iron and steel powder using dynamic conditions. Low temperature isothermal measurements reveal more complex reduction mechanisms with autocatalytic and decelerating reduction behaviours for iron and steel powder grades, respectively.
- Reduction of the oxide layer on iron powder is similar to the initial steps of hematite reduction, whereas the apparent activation energies are lower for reduction of oxide layers on steel powder. The difference is believed to reflect the influence of Cr on the oxide layer as well as the initial surface state of the powder grades. The chromium is believed to alter the chemistry and structure of the oxide layers, thereby changing the reduction properties of the powder grades.

Sintering

- Water-atomized iron and low-alloyed steel powder grades are heavily deformed in uniaxial die-compaction. On a local level, protrusions and small sections of particles are more heavily deformed and show a higher density of low-angle grain boundaries, which may aid diffusion.
- The initial heating stage of sintering can account for a relatively large fraction of the total sintering shrinkage. The fraction was observed to increase with increasing green density of the compacts. The changes are believed to originate mainly from an increase in the interparticle contact areas, but the influence of defective zone caused by compaction cannot be ruled out although it is expected to contribute to a lesser extent.
- Sintering anisotropy was investigated for water-atomized iron and low-alloyed steel powder in the low-temperature range. The anisotropy starts with initial sintering at low temperatures and reaches a maximum as the samples approaches the ferrite-austenite transformation.
- Sintering shrinkages at low temperatures are shown to be affected by the processing atmosphere, indicating the strong link between oxide reduction and sinter neck development.

Chapter 8

SUGGESTIONS FOR FUTURE WORK

While a large pool of knowledge already exists regarding processes related to sintering of iron and steel powder, there are several gaps which can be investigated further.

Oxide reduction and oxygen removal

- The involvement of alloying elements and structural changes in the reduction of the surface oxide layer at lower temperatures can be inferred from a combination of thermogravimetric and XPS analyses. However, an explicit proof of the presence of Cr cations inside the oxide layer or the mechanism which explains the destabilization is missing.
- The kinetic analyses in the thesis can be used to predict the reduction of the surface oxide layer under arbitrary temperature programs. This can prove beneficial during annealing of powder to reduce oxygen levels.

Sintering

- Development of sinter necks and densification of powder compacts is known to be affected both by the increase in interparticle contact area during compaction and by the creation of a defective zone that could enhance diffusion. However, the relative contributions from these factors is still unknown.
- At some elevated temperature, recrystallization of deformed regions will occur which thereby mitigates further diffusion via dislocation pipes. This temperature range is not found but will provide the upper limit to where the contribution from structural activation can be expected.
- Sintering anisotropy as a function of alloy composition, sintering temperature, and processing atmosphere can be interesting to investigate.

Surface analysis

- The involvement of Cr, Mn and other cationic species in the reduction of the surface oxide layer can be analysed by surface sensitive techniques to provide further insights into how they affect the reduction.

Chapter 9

ACKNOWLEDGEMENTS

First and foremost, I would like to express my gratitude towards my supervisors Professor Lars Nyborg and Professor Eduard Hryha for providing me with support and guidance throughout the work, as well as the freedom to pursue my own research interests.

Funding from the Swedish Foundation for Strategic Research (SSF) as well as Production Area of Advance at Chalmers University of Technology is greatly appreciated.

Höganäs AB and its employees, in particular Dr. Dimitris Chasoglou and Dmitri Riabov, are gratefully acknowledged for helping me by providing powder, chemical analyses, pressing, and for their scientific cooperation.

Thanks are extended to Yu Cao and Ruslan Shvab for sharing knowledge and introducing me to surface science, and for being part of my research as co-authors.

Special thanks are given to Roger Sagdahl, Håkan Millqvist and Dr. Eric Tam for their never-ending willingness to help with practical support if, and when, something breaks down.

I would like to thank all colleagues and members of the department for creating a pleasant and encouraging working environment.

I would especially like to express my thanks to all fellow PhD students, past and present, with whom I have shared this journey for the last few years. A special thanks to the people of the powder group, for mostly fruitful discussions about everything related to particles, and especially the problems they impose on our daily lives. I am particularly grateful to Mahesh and Swathi for all our discussions about the purest and most noble form of powder metallurgy.

I would like to thank my friends not at Chalmers, for reminding me of the outside world.

Warm embraces to my family, without whom I would not have been able to complete this.

My sincere and loving thanks to Kristina, for supporting me throughout all aspects of life, and encouraging me to strive to become the best version of myself. Finally, to Vide, my son, for completely changing my life, and for teaching me things about myself that I never knew existed.

Chapter 10

REFERENCES

[1] J.M.C. Azevedo, A. Cabrera Serrenho, J.M. Allwood, Energy and material efficiency of steel powder metallurgy, Powder Technol. 328 (2018) 329–336. https://doi.org/10.1016/j.powtec.2018.01.009.

[2] W. Schatt, K.-P. Wieters, Powder Metallurgy - Processing and Materials, European Powder Metallurgy Association, 1997.

[3] V. Kruzhanov, V. Arnhold, Energy consumption in powder metallurgical manufacturing, Powder Metall. 55 (2012) 14–21. https://doi.org/10.1179/174329012X13318077875722.

[4] G.F. Bocchini, Energy requirements of structural components: Powder metallurgy v. other production processes, Powder Metall. 26 (1983) 101–113. https://doi.org/10.1179/pom.1983.26.2.101.

[5] Höganäs AB, Design and Mechanical Properties, Höganäs Handb. Sintered Components. (2013) 1–130.

[6] R. de Oro Calderon, C. Gierl-Mayer, H. Danninger, Application of thermal analysis techniques to study the oxidation/reduction phenomena during sintering of steels containing oxygen-sensitive alloying elements, J. Therm. Anal. Calorim. (2016). https://doi.org/10.1007/s10973-016-5508-5.

[7] R. De Oro Calderón, E. Bernardo, M. Campos, C. Gierl-Mayer, H. Danninger, J.M. Torralba, Tailoring master alloys for liquid phase sintering: Effect of introducing oxidation-sensitive elements, Powder Metall. 59 (2016) 31–40. https://doi.org/10.1080/00325899.2016.1148897.

[8] M. Vattur Sundaram, Novel approaches for acheiving full density powder metallurgy steels - PhD thesis, Chalmers University of Technology, 2019.

[9] I. Cristofolini, M. Pilla, A. Rao, S. Libardi, A. Molinari, Dimensional and geometrical precision of powder metallurgy parts sintered and sinterhardened at high temperature, Int. J. Precis. Eng. Manuf. 14 (2013) 1735–1742. https://doi.org/10.1007/s12541-013-0233-5.

[10] I. Cristofolini, C. Menapace, M. Cazzolli, A. Rao, W. Pahl, A. Molinari, The effect of anisotropic dimensional change on the precision of steel parts produced by powder metallurgy, J. Mater. Process. Technol. 212 (2012) 1513–1519. https://doi.org/10.1016/j.jmatprotec.2012.02.009.

[11] H. Danninger, C. Gierl-mayer, Advanced powder metallurgy steel alloys, in: Adv. Powder Metall. Prop. Process. Appl., 2013: pp. 149–201. https://doi.org/10.1016/0026-0657(92)91807-V.

[12] E. Hryha, L. Nyborg, Oxide transformation in Cr-Mn-prealloyed sintered steels: Thermodynamic and kinetic aspects, Metall. Mater. Trans. A Phys. Metall. Mater. Sci. 45 (2014) 1736–1747. https://doi.org/10.1007/s11661-013-1969-3.

[13] D. Chasoglou, E. Hryha, L. Nyborg, Effect of process parameters on surface oxides on chromium-alloyed steel powder during sintering, Mater. Chem. Phys. 138 (2013) 405–415. https://doi.org/10.1016/j.matchemphys.2012.11.074.

[14] D. Chasoglou, E. Hryha, M. Norell, L. Nyborg, Characterization of surface oxides on water-atomized steel powder by XPS/AES depth profiling and nano-scale lateral surface analysis, Appl. Surf. Sci. 268 (2013) 496–506. https://doi.org/10.1016/j.apsusc.2012.12.155.

[15] Z.A. Munir, Surface oxides and sintering of metals, Powder Metall. 24 (1981) 177–180. https://doi.org/10.1179/pom.1981.24.4.177.

[16] P. Ramakrishnan, G.S. Tendolkar, Influence of thin oxide films on the mechanical properties of sintered metal-powder compacts, Powder Metall. 7 (1964) 34–49. https://doi.org/10.1179/pom.1964.7.13.003.

[17] H. Danninger, C. Gierl, S. Kremel, G. Leitner, Y. Yu, Degassing And Deoxidation Processes During Sintering Of Unalloyed And Alloyed Pm Steels, Powder Metall. Prog. 2 (2002) 125–140.

[18] M. Hull, Astaloy CrM: new generation powder from Höganäs, Powder Metall. 41 (1998) 232–233. https://doi.org/10.1179/pom.1998.41.4.227.

[19] R.M. German, Sintering Theory and Practice, John Wiley & Sons, New York, 1996.

[20] L. Parilak, E. Dudrova, R. Bidulsky, M. Kabatova, Quantification of Metal Powder Compressibility in Uniaxial Compaction, Euro PM2004. 1 (2004) 593–598.

[21] L. Parilak, E. Dudrova, R. Bidulsky, M. Kabatova, Derivation, testing and application of a practical compaction equation for cold die-compacted metal powders, Powder Technol. 322 (2017) 447–460. https://doi.org/10.1016/j.powtec.2017.09.027.

[22] A. Molinari, C. Menapace, E. Torresani, I. Cristofolini, M. Larsson, Working hypothesis for origin of anisotropic sintering shrinkage caused by prior uniaxial cold compaction, Powder Metall. 000 (2012) 1–8. https://doi.org/10.1179/1743290112Y.0000000043.

[23] E. Torresani, Mechanism of anisotropic shrinkage during sintering of metallic powders - PhD thesis, University of Trento, 2016.

[24] A. Zavaliangos, J.M. Missiaen, D. Bouvard, Anisotropy in shrinkage during sintering, Sci. Sinter. 38 (2006) 13–25. https://doi.org/10.2298/SOS0601013Z.

[25] S. Karamchedu, E. Hryha, L. Nyborg, Changes in the surface chemistry of chromium-alloyed powder metallurgical steel during delubrication and their impact on sintering, J. Mater. Process. Technol. 223 (2015) 171–185. https://doi.org/10.1016/j.jmatprotec.2015.03.054.

[26] E. Hryha, E. Dudrova, L. Nyborg, On-line control of processing atmospheres for proper sintering of oxidation-sensitive PM steels, J. Mater. Process. Technol. 212 (2012) 977–987. https://doi.org/10.1016/j.jmatprotec.2011.12.008.

[27] R.M. German, Chapter Two - History of Sintering, Sinter. from Empir. Obs. to Sci. Princ. (2014) 13–40. https://doi.org/http://dx.doi.org/10.1016/B978-0-12-401682-8.00002-1.

[28] A.R. Poster, H.H. Hausner, Alpha and Gamma Phase Sintering of Carbonyl and Other Iron Powders, in: Mod. Dev. Powder Metall., 1966: pp. 26–44. https://doi.org/10.1007/978-1-4684-7882-2_3.

[29] J.M. Cullen, J.M. Allwood, M.D. Bambach, Mapping the global flow of steel: From steelmaking to end-use goods, Environ. Sci. Technol. 46 (2012) 13048–13055. https://doi.org/10.1021/es302433p.

[30] R.M. German, Chapter One - Introduction, Sinter. from Empir. Obs. to Sci. Princ. (2014) 1–12. https://doi.org/10.1016/B978-0-12-401682-8.00001-X.

[31] H. Danninger, What will be the future of powder metallurgy?, Powder Metall. Prog. 18 (2018) 70–79. https://doi.org/10.1515/pmp-2018-0008.

[32] Höganäs AB, Production of Sintered Components, in: Höganäs Handb. Sintered Components, 2013: pp. 1–170.

[33] Höganäs AB, Material and Powder Properties, in: Höganäs Handb. Sintered Components, 2013: pp. 1–114.

[34] H. Danninger, C. Gierl, New alloying systems for ferrous powder metallurgy precision parts, Sci. Sinter. 40 (2008) 33–46. https://doi.org/10.2298/SOS0801033D.

[35] E. Hryha, L. Cajkova, E. Dudrova, L. Nyborg, Study of reduction/oxidation processes in Cr-Mo prealloyed steels during sintering by continuous atmosphere monitoring, Powder Metall. Prog. 7 (2007) 181–197.

[36] H. Danninger, C. Gierl, Processes in PM steel compacts during the initial stages of sintering, Mater. Chem. Phys. 67 (2001) 49–55. https://doi.org/10.1016/S0254-0584(00)00419-3.

[37] D. Chasoglou, E. Hryha, L. Nyborg, Effect of Sintering Atmosphere on the Transformation of Surface Oxides during the Sintering of Chromium Alloyed Steel, Powder Metall. Prog. 9(2009) (2010) 141–155.

[38] E. Hryha, C. Gierl, L. Nyborg, H. Danninger, E. Dudrova, Surface composition of the steel powders pre-alloyed with manganese, Appl. Surf. Sci. 256 (2010) 3946–3961. https://doi.org/10.1016/j.apsusc.2010.01.055.

[39] H. Karlsson, L. Nyborg, S. Berg, Surface chemical analysis of prealloyed water atomised steel powder, Powder Metall. 48 (2005) 51–58. https://doi.org/10.1179/0032589005X37675.

[40] A. Molinari, E. Torresani, C. Menapace, M. Larsson, The Anisotropy of Dimensional Change on Sintering of Iron, J. Am. Ceram. Soc. 98 (2015) 3431–3437. https://doi.org/10.1111/jace.13852.

[41] E. Hryha, L. Nyborg, Thermogravimetry study of the effectiveness of different reducing agents during sintering of Cr-prealloyed PM steels, J. Therm. Anal. Calorim. 118 (2014) 825–834. https://doi.org/10.1007/s10973-014-3915-z.

[42] J.L. Meijering, On the diffusion of oxygen through solid iron, Acta Metall. 3 (1955)

157–162. https://doi.org/10.1016/0001-6160(55)90085-7.

[43] J. Wendel, R. Shvab, Y. Cao, E. Hryha, L. Nyborg, Surface analysis of fine water-atomized iron powder and sintered material, Surf. Interface Anal. 50 (2018) 1065–1071. https://doi.org/10.1002/sia.6455.

[44] C. Gierl-Mayer, H. Danninger, Dilatometry Coupled With Ms As Instrument for Process Control in Sintering of Powder, Powder Metall. Prog. 15 (2015) 3–12. http://www.imr.saske.sk/pmp/issue/1-2015/PMP_Vol15_No1_p_003-012.pdf.

[45] C. Gierl-Mayer, R. de Oro Calderon, H. Danninger, The Role of Oxygen Transfer in Sintering of Low Alloy Steel Powder Compacts: A Review of the “Internal Getter” Effect, JOM. 68 (2016). https://doi.org/10.1007/s11837-016-1819-z.

[46] M. Vattur Sundaram, E. Hryha, L. Nyborg, Xps Analysis of Oxide Transformation During Sintering of Chromium Alloyed Pm Steels, Powder Metall. Prog. 14 (2014) 85–92. http://www.imr.saske.sk/pmp/issue/2-2014/PMP_Vol14_No2_p_085-092.pdf.

[47] I. Olefjord, Esca-studies of the composition profile of low temperature oxide formed on chromium steels-I. Oxydation in dry oxygen, Corros. Sci. 15 (1975) 687–696. https://doi.org/10.1016/0010-938X(75)90033-5.

[48] A. Pineau, N. Kanari, I. Gaballah, Kinetics of reduction of iron oxides by H2. Part I. Low temperature reduction of hematite, Thermochim. Acta. 447 (2006) 89–100. https://doi.org/10.1016/j.tca.2007.01.014.

[49] A. Pineau, N. Kanari, I. Gaballah, Kinetics of reduction of iron oxides by H2. Part II. Low temperature reduction of magnetite, Thermochim. Acta. 456 (2007) 75–88. https://doi.org/10.1016/j.tca.2007.01.014.

[50] D. Spreitzer, J. Schenk, Reduction of Iron Oxides with Hydrogen—A Review, Steel Res. Int. 90 (2019). https://doi.org/10.1002/srin.201900108.

[51] Z. Chen, C. Zeilstra, J. Van Der Stel, J. Sietsma, Z. Chen, Review and data evaluation for high-temperature reduction of iron oxide particles in suspension in suspension, Ironmak. Steelmak. 0 (2019) 1–7. https://doi.org/10.1080/03019233.2019.1589755.

[52] D. Fernández-González, I. Ruiz-Bustinza, J. Mochón, C. González-Gasca, L.F. Verdeja, Iron Ore Sintering: Process, Miner. Process. Extr. Metall. Rev. 38 (2017) 215–227. https://doi.org/10.1080/08827508.2017.1288115.

[53] G. Munteanu, L. Ilieva, D. Andreeva, Kinetic parameters obtained from TPR data for a-Fe2O3 and Au/a-Fe2O3, Thermochim. Acta. 291 (1997) 171–177.

[54] G. Munteanu, L. Ilieva, D. Andreeva, TPR data regarding the effect of sulfur on the reducibility of □a-Fe2O3, Thermochim. Acta. 329 (1999) 157–162.

[55] G. Munteanu, P. Budrugeac, L. Ilieva, T. Tabakova, D. Andreeva, E. Segal, Kinetics of temperature programmed reduction of Fe3O4 promoted with copper: application of iso-conversional methods, J. Mater. Sci. 38 (2003) 1995–2000. https://doi.org/10.1023/A.

[56] P. Pourghahramani, E. Forssberg, Effects of mechanical activation on the reduction behavior of hematite concentrate, Int. J. Miner. Process. 82 (2007) 96–105. https://doi.org/10.1016/j.minpro.2006.11.003.

[57] P. Pourghahramani, E. Forssberg, Reduction kinetics of mechanically activated hematite concentrate with hydrogen gas using nonisothermal methods, Thermochim. Acta. 454 (2007) 69–77. https://doi.org/10.1016/j.tca.2006.12.023.

[58] P.K. Higgins, Z.A. Munir, Influence of surface oxide layer on sintering process of lead, Powder Metall. 21 (1978) 188–194. https://doi.org/10.1179/pom.1978.21.4.188.

[59] A. Molinari, E. Bisoffi, C. Menapace, J.M. Torralba, Shrinkage kinetics during the early stage of sintering: The time depending effective diffusion coefficient, Int. Powder Metall. Congr. Exhib. Euro PM 2013. (2013). http://www.scopus.com/inward/record.url?eid=2-s2.0-84924940557&partnerID=tZOtx3y1.

[60] A. Molinari, E. Bisoffi, C. Menapace, J. Torralba, Shrinkage kinetics during early stage sintering of cold isostatically compacted iron powder, Powder Metall. 57 (2014) 61–69. https://doi.org/10.1179/1743290113Y.0000000068.

[61] D. Chasoglou, Surface Chemical Characteristics of Chromium-alloyed Steel Powder and the Role of Process Parameters during Sintering - PhD thesis, Chalmers University of Technology, 2012. http://publications.lib.chalmers.se/publication/157463?pubid=128185.

[62] H. Karlsson, Role of Surface Oxides in Sintering of Chromium-alloyed Steel Powder - PhD thesis, CHalmers University of Technology, 2005.

[63] C. Oikonomou, E. Hryha, Å. Ahlin, L. Nyborg, Effect of Powder Properties on the Compressibility of Water-Atomized Iron and Low-Alloyed Steel Grades, Euro PM2013. 2 (2013) 205–212. http://publications.lib.chalmers.se/publication/188217-effect-of-powder-properties-on-the-compressibility-of-water-atomized-iron-and-low-alloyed-steel-grad.

[64] J. Wendel, S.K. Manchili, E. Hryha, L. Nyborg, Oxide reduction and oxygen removal in water-atomized iron powder: a kinetic study, J. Therm. Anal. Calorim. (2020). https://doi.org/10.1007/s10973-020-09724-6.

[65] M. Hrubovčáková, E. Dudrová, E. Hryha, M. Kabátová, J. Harvanová, Parameters controlling the oxide reduction during sintering of chromium prealloyed steel, Adv. Mater. Sci. Eng. 2013 (2013). https://doi.org/10.1155/2013/789373.

[66] R.M. German, Chapter Seven - Thermodynamic and Kinetic Treatments, in: Sinter. from Empir. Obs. to Sci. Princ., 2014: pp. 183–226. https://doi.org/http://dx.doi.org/10.1016/B978-0-12-401682-8.00007-0.

[67] H.F. Fischmeister, R. Zahn, The Mechanism of Sintering of a-Iron, Mod. Dev. Powder Metall. (1966) 12–25.

[68] D.A. Porter, K.E. Easterling, M.Y. Sherif, Phase Transformations in Metals and Alloys, Third edit, Taylor & Francis Group, 2009.

[69] H.H. Hausner, Modern Developments in Powder Metallurgy, 1966. https://doi.org/10.1007/978-1-4684-7882-2.

[70] M. Pilla, Effect of process parameters on the dimensional and geometrical precision of PM steel parts - PhD thesis, University of Trento, 2013.

[71] P.G. Shewmon, Transformation in Metals, McGraw-Hill Book Company, 1969.

[72] L.N. Brewer, M.A. Othon, L.M. Young, T.M. Angeliu, Misorientation mapping for visualization of plastic deformation via electron back-scattered diffraction., Microsc. Microanal. 12 (2006) 85–91. https://doi.org/10.1017/S1431927606060120.

[73] P. Lányi, W. Hermel, Structural activity and shrinkage kinetics in early stages of sintering process, Powder Metall. 24 (1981) 93–100. https://doi.org/10.1179/pom.1981.24.2.93.

[74] E. Friedrich, W. Schatt, Sintering of one-component model systems: nucleation and movement of dislocations in necks, Powder Metall. (1980) 193–197.

[75] J.L. Johnson, D.F. Heaney, N.S. Myers, Metal injection molding (MIM) of heavy alloys, refractory metals, and hardmetals, in: Handb. Met. Inject. Molding, 2012: pp. 526–567. https://doi.org/10.1533/9780857096234.4.526.

[76] P. Kofstad, High Temperature Corrosion, 1 edition, Elsevier Applied Science, 1988.

[77] H.E. Kissinger, Reaction Kinetics in Differential Thermal Analysis, Anal. Chem. 29 (1957) 1702–1706. https://doi.org/10.1021/ac60131a045.

[78] H.E. Kissinger, Variation of peak temperature with heating rate in differential thermal analysis, J. Res. Natl. Bur. Stand. (1934). 57 (1956) 217. https://doi.org/10.6028/jres.057.026.

[79] P. Murray, J. White, Kinetics of clay dehydration, Clay Min. 2 (1955) 255–264. https://doi.org/10.1180/claymin.1949.000.03.05.

[80] L.N. Samuelsson, R. Moriana, M.U. Babler, M. Ek, K. Engvall, Model-free rate expression for thermal decomposition processes: The case of microcrystalline cellulose pyrolysis, Fuel. 143 (2015) 438–447. https://doi.org/10.1016/j.fuel.2014.11.079.

[81] L.N. Samuelsson, Isoconversional analysis for the prediction of mass-loss rates during pyrolysis of biomass, KTH Royal Institute of Technology, 2016.

[82] J.E. White, W.J. Catallo, B.L. Legendre, Biomass pyrolysis kinetics: A comparative critical review with relevant agricultural residue case studies, J. Anal. Appl. Pyrolysis. 91 (2011) 1–33. https://doi.org/10.1016/j.jaap.2011.01.004.

[83] I.U. Mohsin, D. Lager, C. Gierl, W. Hohenauer, H. Danninger, Thermo-kinetics study of MIM thermal de-binding using TGA coupled with FTIR and mass spectrometry, Thermochim. Acta. 503–504 (2010) 40–45. https://doi.org/10.1016/j.tca.2010.03.005.

[84] M. Belgacem, B. Thierry, G. Jean-Claude, Investigations on thermal debinding process for fine 316L stainless steel feedstocks and identification of kinetic parameters from coupling experiments and finite element simulations, Powder Technol. 235 (2013) 192–202. https://doi.org/10.1016/j.powtec.2012.10.006.

[85] E. Hryha, H. Borgström, K. Sterky, L. Nyborg, Influence of the steel powder type and processing parameters on the debinding of PM compacts with gelatin binder, J. Therm. Anal. Calorim. 118 (2014) 695–704. https://doi.org/10.1007/s10973-014-3839-7.

[86] B. Jankovic, B. Adnadevic, S. Mentus, The kinetic study of temperature-programmed reduction of nickel oxide in hydrogen atmosphere, Chem. Eng. Sci. 63 (2008) 567–575. https://doi.org/10.1016/j.ces.2007.09.043.

[87] D. Jelić, J. Penavin-Škundrić, D. Majstorović, S. Mentus, The thermogravimetric study

of silver(I) oxide reduction by hydrogen, Thermochim. Acta. 526 (2011) 252–256. https://doi.org/10.1016/j.tca.2011.10.001.

[88] W.K. Jozwiak, E. Kaczmarek, T.P. Maniecki, W. Ignaczak, W. Maniukiewicz, Reduction behavior of iron oxides in hydrogen and carbon monoxide atmospheres, Appl. Catal. A Gen. 326 (2007) 17–27. https://doi.org/10.1016/j.apcata.2007.03.021.

[89] H.L. Friedman, Kinetics of thermal degradation of char-forming plastics from thermogravimetry. Application to a phenolic plastic, J. Polym. Sci. Part C Polym. Symp. 6 (1964) 183–195. https://doi.org/10.1002/polc.5070060121.

[90] S. Vyazovkin, A.K. Burnham, J.M. Criado, L.A. Pérez-Maqueda, C. Popescu, N. Sbirrazzuoli, ICTAC Kinetics Committee recommendations for performing kinetic computations on thermal analysis data, Thermochim. Acta. 520 (2011) 1–19. https://doi.org/10.1016/j.tca.2011.03.034.

[91] I.E. Åkerblom, D.O. Ojwang, J. Grins, G. Svensson, A thermogravimetric study of thermal dehydration of copper hexacyanoferrate by means of model-free kinetic analysis, J. Therm. Anal. Calorim. 129 (2017) 721–731. https://doi.org/10.1007/s10973-017-6280-x.

[92] S. Vyazovkin, C.A. Wight, Model-free and model-fitting approaches to kinetic analysis of isothermal and nonisothermal data, Thermochim. Acta. 340–341 (1999) 53–68. https://doi.org/10.1016/s0040-6031(99)00253-1.

[93] A.W. Coats, J.P. Redfern, Kinetic Parameters from Thermogravimetric Data, Nature. 201 (1964) 68–69.

[94] T. Akahira, T. Sunose, Method of determining activation deterioration constants of eletrical insulation materials, in: Jt. Conv. Four Electr. Institutes, 1971: pp. 22–31.

[95] F.S. Buffington, K. Hirano, M. Cohen, Self diffusion in iron, Acta Metall. 9 (1961) 434–439. https://doi.org/10.1016/0001-6160(61)90137-7.

[96] Y. Iijima, Diffusion in high-purity iron: Influence of magnetic transformation on diffusion, J. Phase Equilibria Diffus. 26 (2005) 466–471. https://doi.org/10.1361/154770305X66547.

[97] A. Inoue, H. Nitta, Y. Iijima, Grain boundary self-diffusion in high purity iron, Acta Mater. 55 (2007) 5910–5916. https://doi.org/10.1016/j.actamat.2007.06.041.

[98] Y. Shima, Y. Ishikawa, H. Nitta, Y. Yamazaki, K. Mimura, M. Isshiki, Y. Iijima, Self-Diffusion along Dislocations in Ultra High Purity Iron, Mater. Trans. 43 (2002) 173–177. https://doi.org/10.2320/matertrans.43.173.

[99] H. Föll, Diffusion in iron, (n.d.). https://www.tf.uni-kiel.de/matwis/amat/iss/kap_5/illustr/s5_2_3d.html (accessed May 2, 2018).

[100] S. Vyazovkin, K. Chrissafis, M.L. Di Lorenzo, N. Koga, M. Pijolat, B. Roduit, N. Sbirrazzuoli, J.J. Suñol, ICTAC Kinetics Committee recommendations for collecting experimental thermal analysis data for kinetic computations, Thermochim. Acta. 590 (2014) 1–23. https://doi.org/10.1016/j.tca.2014.05.036.

[101] F. Scholz, J.. Driver, E. Woldt, The stored energy of cold rolled ultra high purity iron, Scr. Mater. 40 (1999) 949–954. https://doi.org/10.1016/S1359-6462(99)00047-0.

[102] F. Scholz, E. Woldt, The release of stored energy during recovery and recrystallization of cold rolled ultra high purity iron, J. Therm. Anal. Calorim. 64 (2001) 895–903. https://doi.org/10.1023/A:1011558511053.

[103] T. Yamashita, P. Hayes, Analysis of XPS spectra of Fe2+ and Fe3+ ions in oxide materials, Appl. Surf. Sci. 254 (2008) 2441–2449. https://doi.org/10.1016/j.apsusc.2007.09.063.

[104] M. Fondell, M. Gorgoi, M. Boman, A. Lindblad, Surface modification of iron oxides by ion bombardment – Comparing depth profiling by HAXPES and Ar ion sputtering, J. Electron Spectros. Relat. Phenomena. 224 (2018) 23–26. https://doi.org/10.1016/j.elspec.2017.09.008.

[105] L. Nyborg, A. Nylund, I. Olefjord, Thickness Determination of oxide Layers on Spherically-shaped Metal Powders by ESCA, Surf. Interface Anal. 12 (1988) 110–114. https://doi.org/10.1002/sia.740120209.

[106] M. Norell, L. Nyborg, T. Tunberg, I. Olefjord, Thickness determination of surface oxides on metal powder by AES depth profiling, Surf. Interface Anal. 19 (1992) 71–76. https://doi.org/10.1002/sia.740190116.

[107] H. Asteman, R. Norling, J.E. Svensson, A. Nylund, L. Nyborg, Quantitative AES depth profiling of iron and chromium oxides in solid solution, (Cr1-xFex)2O3, Surf. Interface Anal. 34 (2002) 234–238. https://doi.org/10.1002/sia.1290.

[108] S.C. Tjong, J. Eldridge, R.W. Hoffman, AES studies of the oxides formed on iron-chromium alloys at 400°C, Appl. Surf. Sci. 14 (1983) 297–306. https://doi.org/10.1016/0378-5963(83)90044-2.

[109] C. Leygraf, G. Hultquist, S. Ekelund, A LEED/AES study of the oxidation of Fe0.84Cr0.16 (100) and (110), Surf. Sci. 51 (1975) 409–432. https://doi.org/10.1016/0039-6028(75)90391-X.

[110] H. Danninger, C. Gierl-mayer, S. Strobl, Evolution of microstructure in ferrous and non-ferrous materials, 2013. https://doi.org/10.1533/9780857098900.2.308.

[111] S. Suzuki, Y. Ishikawa, M. Isshiki, Y. Waseda, Native oxide layers formed on the surface of ultra high-purity iron and copper investigated by angle resolved XPS, Mater. Trans. JIM. 38 (1997) 1004–1009. https://doi.org/10.2320/matertrans1989.38.1004.

[112] T.S.T. Saharuddin, A. Samsuri, F. Salleh, R. Othaman, M. Bin Kassim, M.W. Mohamed Hisham, M.A. Yarmo, Studies on reduction of chromium doped iron oxide catalyst using hydrogen and various concentration of carbon monoxide, Int. J. Hydrogen Energy. 42 (2017) 9077–9086. https://doi.org/10.1016/j.ijhydene.2016.08.151.

[113] J. Wendel, S.K. Manchili, E. Hryha, L. Nyborg, Thermochimica Acta Reduction of surface oxide layers on water-atomized iron and steel powder in hydrogen : Effect of alloying elements and initial powder state, Thermochim. Acta. 692 (2020) 178731. https://doi.org/10.1016/j.tca.2020.178731.

[114] M.C. Biesinger, B.P. Payne, A.P. Grosvenor, L.W.M. Lau, A.R. Gerson, R.S.C. Smart, Resolving surface chemical states in XPS analysis of first row transition metals, oxides and hydroxides: Cr, Mn, Fe, Co and Ni, Appl. Surf. Sci. 257 (2011) 2717–2730. https://doi.org/10.1016/j.apsusc.2010.10.051.

[115] J. Wendel, S.K. Manchili, Y. Cao, E. Hryha, L. Nyborg, Evolution of surface chemistry during sintering of water-atomized iron and low-alloyed steel powder, Surf. Interface Anal. (2020) 1–5. https://doi.org/10.1002/sia.6852.

[116] E. Torresani, D. Giuntini, C. Zhu, T. Harrington, K.S. Vecchio, A. Molinari, R.K. Bordia, E.A. Olevsky, Anisotropy of Mass Transfer During Sintering of Powder Materials with Pore–Particle Structure Orientation, Metall. Mater. Trans. A. (2018). https://doi.org/10.1007/s11661-018-5037-x.

[117] C. Oikonomou, D.C. Gutiérrez, M. Monclús, J.M. Molina-adareguia, L. Nyborg, Assessment of the Compacting and Annealing Process Steps on the Performance of Finished Soft Magnetic Composite Components, in: Proc. Euro PM 2015 Int. Power Metall. Congr. Exhib., 2015.

[118] V. Šepelák, S. Bégin-Colin, G. Le Caër, Transformations in oxides induced by high-energy ball-milling, Dalt. Trans. 41 (2012) 11927–11948. https://doi.org/10.1039/c2dt30349c.

[119] J.H. Swisher, E.T. Turkdogan, Solubility, Permeability, and Diffusivity of Oxygen in Solid Iron, Trans. Metall. Soc. AIME. 239 (1967) 426–431.

[120] E. Hryha, J. Wendel, Effect of heating rate and process atmosphere on the thermodynamics and kinetics of the sintering of pre-alloyed water-atomized powder metallurgy steels, J. Am. Ceram. Soc. 102 (2018) 748–756. https://doi.org/10.1111/jace.16079.

[121] G.Y. Lee, J. ll Song, J.S. Lee, Reaction kinetics and phase transformation during hydrogen reduction of spherical Fe2O3 nanopowder agglomerates, Powder Technol. 302 (2016) 215–221. https://doi.org/10.1016/j.powtec.2016.07.038.

[122] H.-Y. Lin, Y.-W. Chen, C. Li, The mechanism of reduction of iron oxide by hydrogen, Thermochim. Acta. 400 (2003) 61–67. https://doi.org/10.1016/S0040-6031(02)00478-1.

[123] M.V.C. Sastri, R.P. Viswanath, B. Viswanathan, Studies on the reduction of iron oxide with hydrogen, Int. J. Hydrogen Energy. 7 (1982) 951–955. https://doi.org/10.1016/0360-3199(82)90163-X.